

**LISTA CU CELE MAI SEMNIFICATIVE PUBLICAȚII
(maxim 10)**

1. **Benchea M.**, Iovan-Dragomir A., Crețu S., 2014, „*Misalignment effects in cylindrical roller bearings*”, **Applied Mechanics and Materials**, ISSN 1662-7482, Vol.658, pp.277-282, Trans Tech Publications, Elveția.
2. Crețu S., **Benchea M.**, Iovan-Dragomir A., 2016., “*On basic reference rating life of cylindrical roller bearings. Part II - Elastic-Plastic Analysis*”, **Journal of the Balkan Tribological Association**, **IF = 0.737**, ISSN 1310-4772, Vol.22, No 1, pp.272-280, Ed.SciBulCom.Ltd, Sofia-Bulgaria.
3. Bujoreanu C., Nedeff F., **Benchea M.**, Agop M., 2017, “*Experimental and theoretical considerations on sound absorption performance of waste materials including the effect of backing plates*”, **Appl. Acoustics**, **IF = 3.4**, ISSN 0003-682X, Vol.119, pp.88-93.
4. Oancea I., Bujoreanu C., Budescu M., **Benchea M.**, Grădinaru C.M., 2018, “*Considerations on sound absorption coefficient of sustainable concrete with different waste replacements*”, **J. of Clean. Prod.**, **IF = 11.1**, ISSN 0959-6526, Vol.203, pp.301-312.
5. **Benchea M.**, Crețu S., 2020, “*Surface roughness influence on active surfaces geometry and modified rating life of rolling contacts*”, **IOP Conf. Ser. - Mat. Sci. and Eng.**, vol.724, 012025.
6. Mazurchevici S.N., Marguță A., Istrate B., **Benchea M.**, Boca M., Nedelcu D., 2021, “*Improvements of Arboblend V2 Nature characteristics through depositing thin ceramic layers*”, **Polymers**, **IF = 5**, ISSN 2073-4360, vol.13, nr. 21, 3765, pp.21.
7. **Benchea M.**, Crețu S., 2022, “*An Investigation Regarding the Impact of Running-in on Rolling Contacts Lives*”, *Innovations in Mechanical Engineering. icieng 2021*, **Lecture Notes in Mechanical Engineering**, Springer, Cham.
8. **Benchea M.**, Bujoreanu C., Ianuș G., 2022, “*Acoustic Performance of Some Lined Dissipative Silencers*”, *Innovations in Mechanical Engineering. icieng 2021*, **Lecture Notes in Mechanical Engineering**, Springer, Cham.
9. Achiței D.C., Bălțatu M.S., Vizureanu P., A.V. Sandu, **Benchea M.***, Istrate B., 2022, “*Ni-Cr Alloys Assessment for Dental Implants Suitability*”, **Applied Sciences**, **IF = 2.7**, ISSN 2076-3417, vol.12, nr. 24, 12814, pp.11.
10. Iovan A., **Benchea M.***, Stoleriu S., Tărăboanță I., Cimpoeșu N., Nica I., Andrian S., 2023, “*Effects of Acidic Challenge on Demineralized Root Surface Treated with Silver Diamine Fluoride and Potassium Iodide*”, **Diagnostics**, **IF = 3.6**, ISSN 2075-4418, vol.13, nr. 3, 530, pp.11.

* autor corespondent

Misalignment Effects in Cylindrical Roller Bearings

BENCHEA Marcelin^{1,a}, IOVAN DRAGOMIR Alina^{1,b},
 CRETU Spiridon^{2,c*}

¹Technical University “Gheorghe Asachi” of Iasi, Iasi, 700060, Romania

²RKB Bearings SA, Balerna, 6828, Switzerland

^amarcelin_ben@yahoo.com, ^balina.dragomir@windowslive.com, ^{c*}spcretu@gmail.com

Keywords: edge effect, elastic-plastic contact, shakedown.

Introduction

All cylindrical-rollers profiles exhibit severe discontinuities in the end chamfer zones; the ZB profile includes two more at the common points of the crowned radius and straight line, Fig. 1.

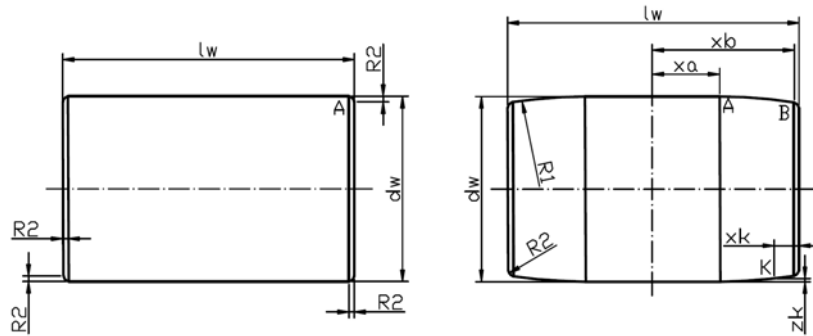


Fig.1 Cylindrical rollers (straight line and ZB profiles).

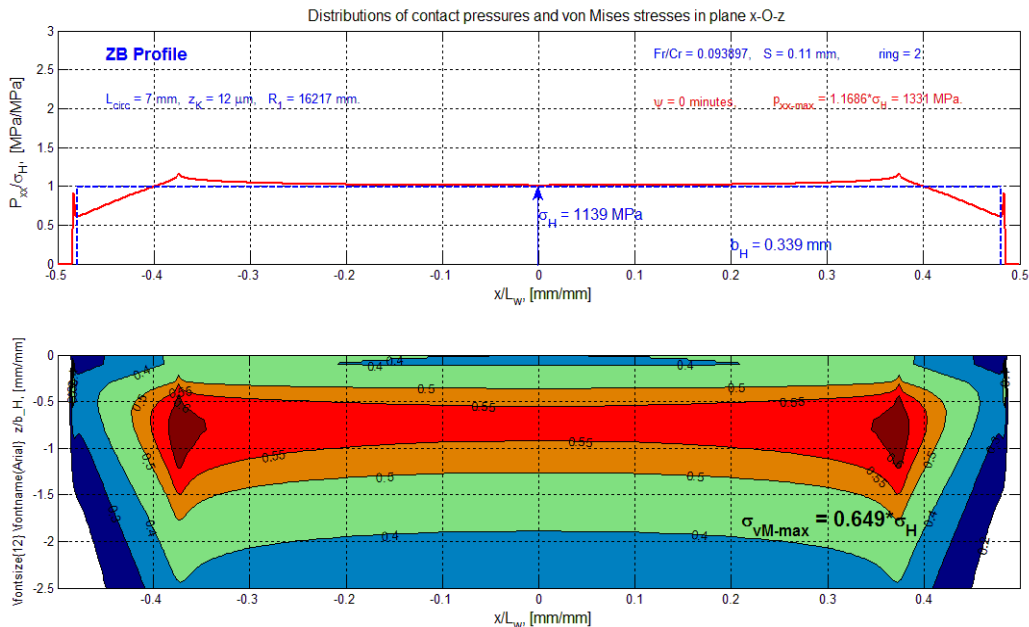


Fig. 2. The contact pressure and von Mises stresses for loading with no misalignment.

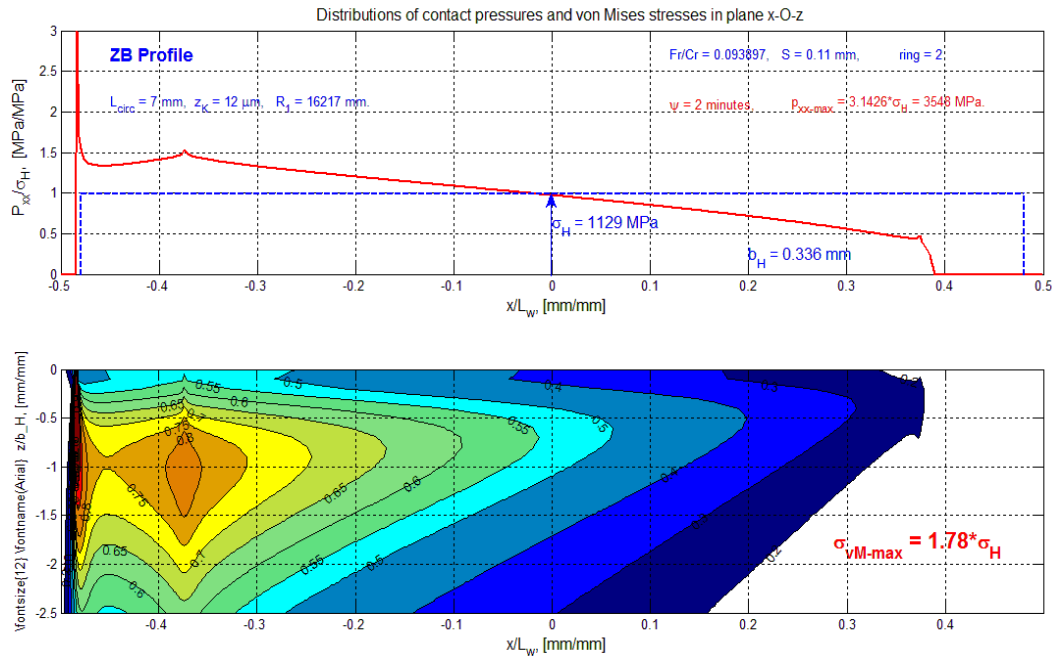


Fig. 3. The contact pressure and von Mises stresses for loading with 2.0 minutes misalignment.

A genuine elastic analysis is able to optimize the roller profile to obtain a stress distribution in the contact zones, Fig. 2, that provides enhanced operational reliability, Ioannides *et al.* [1]. If the misalignment is present the edge loading effects are considerably amplified for one roller’s end and diminished at the other, Fig. 3. The existence of the high pressure peaks determines a significant increase of the von Mises stresses, Fig. 3, and, according to ISO 16281 methodology [2], a very severe reduction of the reference rating life. On the other hand, these von Mises equivalent stresses are able to overcome, locally, the yield limit and to induce both plastic deformations and residual stresses. After a number of cycles the material will shakedown elastically to a slightly modified roller profile, Kapoor and Johnson [3]. If these changes exist they have to be considered in the evaluation of the reference rating life, [2].

Numerical Formulation of the Elastic Non-Hertzian Contact Problem

A hypothetical (virtual) rectangular contact area, denoted A_h , is built, around the initial contact point, on the common tangent plane, Fig. 4.

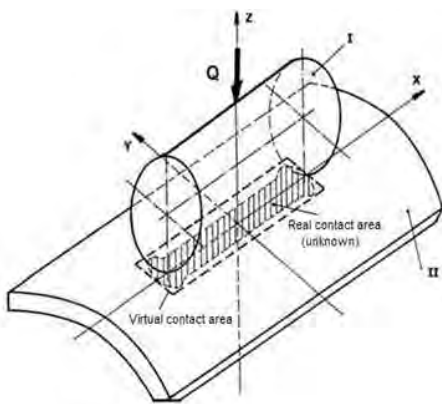


Fig. 4. Real and virtual contact areas.

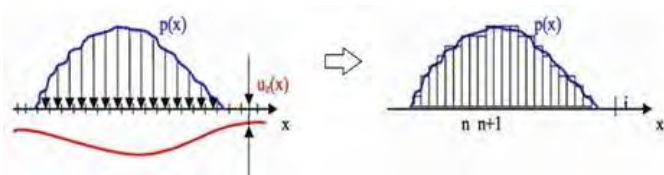


Fig. 5. Real and virtual pressure distributions.

A uniformly spaced rectangular array is built on the hypothetical area with the grid sides parallel to the x and y -axes. The nodes of the grid are denoted by (i, j) , where indices i and j refer to the grid columns and rows, respectively. The real pressure distribution is replaced by a virtual piecewise distribution, Fig. 5. The geometric equation, Boussinesq equation and equilibrium equation,

together with the constraints of non-penetration and non-adhesion, form the system of algebraic equations to provide the real contact area and the pressure distribution. The Conjugate Gradient Method and FFT technique have been involved to solve the mentioned algebraic system of equations. Crețu and Benchea [4], Nelias *et al.*[5]. The components of the stress tensor, induced in the generic point $M(x,y,z)$, are obtained by superposition:

$$\sigma_{ij}(x, y, z) = \sum_{k=0}^{N_x-1} \sum_{l=0}^{N_y-1} C_{ijkl} p_{kl} , \tag{1}$$

where the influence function $C_{ijkl}(x,y,z)$ describes the stress component $\sigma_{ij}(x,y,z)$ due to a unit pressure acting in the patch (k, l) .

Elastic-Plastic Analysis Model

Material Behavior. The material cyclic hardening characteristic is adopted to be described by an isotropic hardening law and the ratchetting effect by a non-linear kinematic hardening law, Crețu [6], Besson *et al.* [7]. The isotropic hardening component of the model defines the yielding stress as a function of the equivalent plastic strain and for materials that cyclically harden is modeled with a simple exponential law as:

$$\sigma_Y^0 = \sigma_{Y0} + Q_\infty \left(1 - e^{-b_\infty \bar{\epsilon}^p} \right). \tag{2}$$

The link between the intensity of the stress tensor and the intensity of the strain tensor is assured by the Ramberg-Osgood’s equation:

$$\bar{\epsilon}_e = \frac{\bar{\sigma}_e}{E} + \left(\frac{\bar{\sigma}_e}{B} \right)^N . \tag{3}$$

Constitutive Equations. The increment of the total strain is assumed to be a sum of the elastic and plastic strain increments:

$$d\epsilon = d\epsilon^e + d\epsilon^p . \tag{4}$$

Hooke’s law assures the differential of elastic strain tensor whereas the differential of plastic strain tensor is:

$$d\epsilon^p = \frac{3}{2} \frac{d\bar{\epsilon}_e^p}{\bar{\sigma}_e} \cdot S . \tag{5}$$

The increments of the total strain are finally obtained as:

$$d\epsilon_{ij} = \frac{1}{E} \left[(1 + \nu) d\sigma_{ij} - \nu \delta_{ij} d\sigma_{kk} \right] + \frac{9}{4} \frac{S_{ij}}{\bar{\sigma}_e^2} \frac{1}{H'} \left[S_{kk} dS_{kk} + (1 - \delta_{kl}) \sigma_{kl} d\sigma_{kl} \right]. \tag{6}$$

In the matrix notation:

$$d\epsilon = [B] \cdot d\sigma , \quad \text{and} \quad d\sigma = [A] \cdot d\epsilon , \quad [A] = [B]^{-1} . \tag{7}$$

Incremental algorithm. The load is increased incrementally till its final value is attained.. For each new load increment the new elastic pressure distribution and corresponding stress state are obtained. The von Mises yield condition is checked and at a certain load increment order, $n + 1$, the yield condition is fulfilled in some points inside the stressed volume and the plastic deformation occurs. For each of these points the stress and strain tensors are obtained in three steps:

In the first step, the increment of the stress tensor is evaluated as the difference between the successive order components; Hooke's law is further used to obtain the increment of the total deformation tensor.

In the second step, the increment of the stress tensor is re-calculated, equation (7), and further the increments of the elastic and plastic strains are obtained:

$$(d\varepsilon_{ij}^e)^{(n+1)} = \frac{1}{E} [(1 + \nu) \cdot d\sigma_{ij}^{(n+1)} - \nu \cdot d\sigma_{kk}^{(n+1)} \cdot \delta_{ij}], \quad (8)$$

$$(d\varepsilon^p)^{(n+1)} = d\varepsilon^{(n+1)} - (d\varepsilon^e)^{(n+1)}. \quad (9)$$

In the third step, the residual stresses increments are added to the stresses increments:

$$d\sigma^{(n+1)} = d\sigma^{(n+1)} + d\sigma_R^{(n+1)}. \quad (10)$$

Finally, the stress and strain tensors components are:

$$\sigma^{(n+1)} = \sigma^{(n)} + d\sigma^{(n+1)}, \quad (11)$$

$$\varepsilon^p{}^{(n+1)} = \varepsilon^p{}^{(n)} + d\varepsilon^p{}^{(n+1)}. \quad (12)$$

The evaluation process of plastic strains and residual stresses is performed in all grid points of the loaded half-space. The depth integration of the plastic strains provides the plastic displacements that modify the contact geometry. The new contact geometry and residual stresses are further considered as initial values for the next loading cycle, the incremental technique being reiterated. The cyclic incremental technique continues till material shakedown. The Melan-Koitter theorems of hardening assures that the related residual stress state is unique, Williams A.[8].

Numerical results

Loading Conditions: Misalignment and Heavy Loads. A NJ2238 roller bearing operating in conditions of heavy radial load $F_R = 450$ kN and 2 minutes misalignment has been selected for this study. The evolutions of the plastic displacements and the corresponding changes induced in the pressure distributions are exemplified in Fig. 6 to Fig. 8.

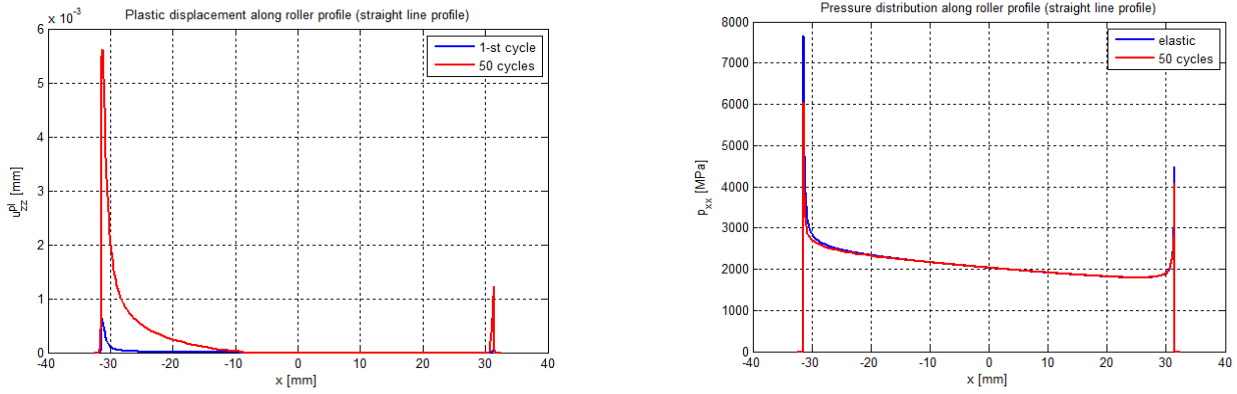


Fig. 6 Plastic displacements and pressure distributions for straight line profile, ($F_R = 450$ kN).

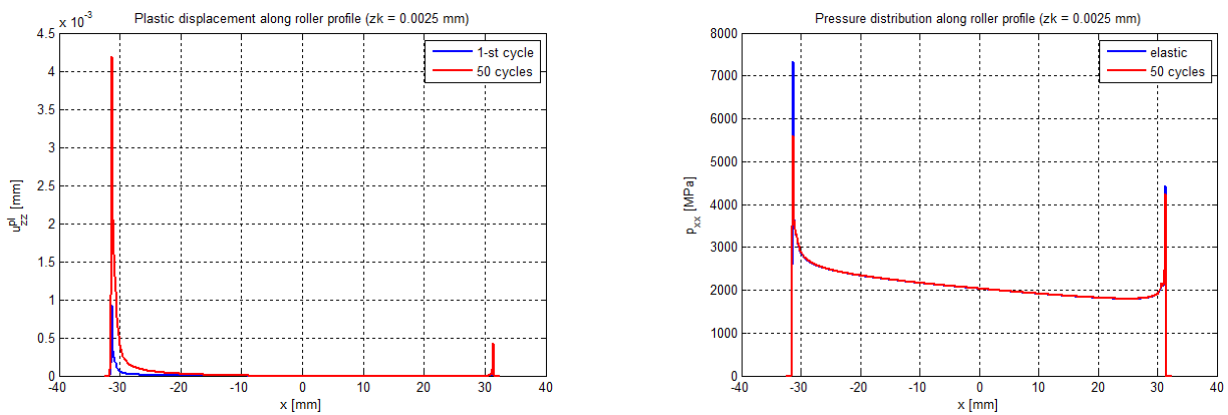


Fig. 7 Plastic displacements and pressure distributions for ZB profile, ($zk = 2.5 \mu\text{m}$, $F_R = 450$ kN).

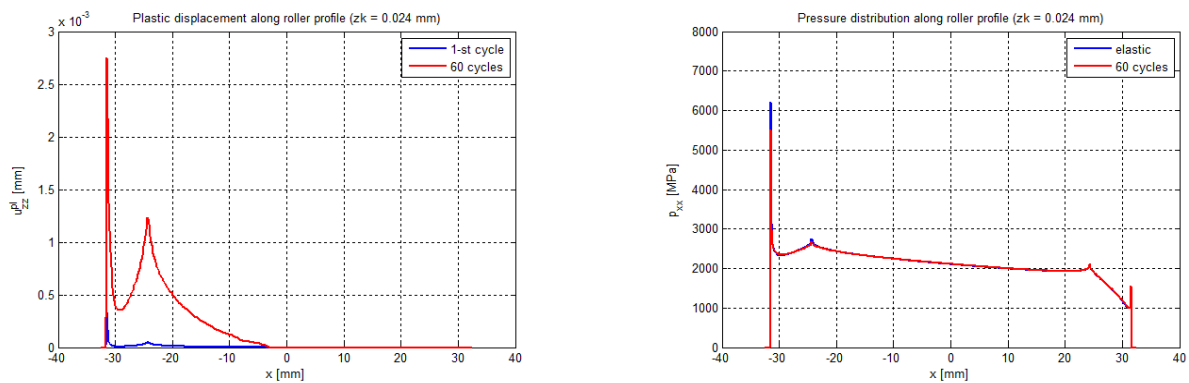


Fig. 8 Plastic displacements and pressure distributions for ZB profile, ($zk = 24 \mu\text{m}$, $F_R = 450$ kN).

Loading Conditions: Misalignment with Transient Overloads. The cylindrical roller bearing that supports a radial force of 100 kN with a very short overloads of 450 kN. The pressure distributions along the profile of the most loaded roller, before and after a transient overload of 450 kN, are exemplified in Fig. 9.

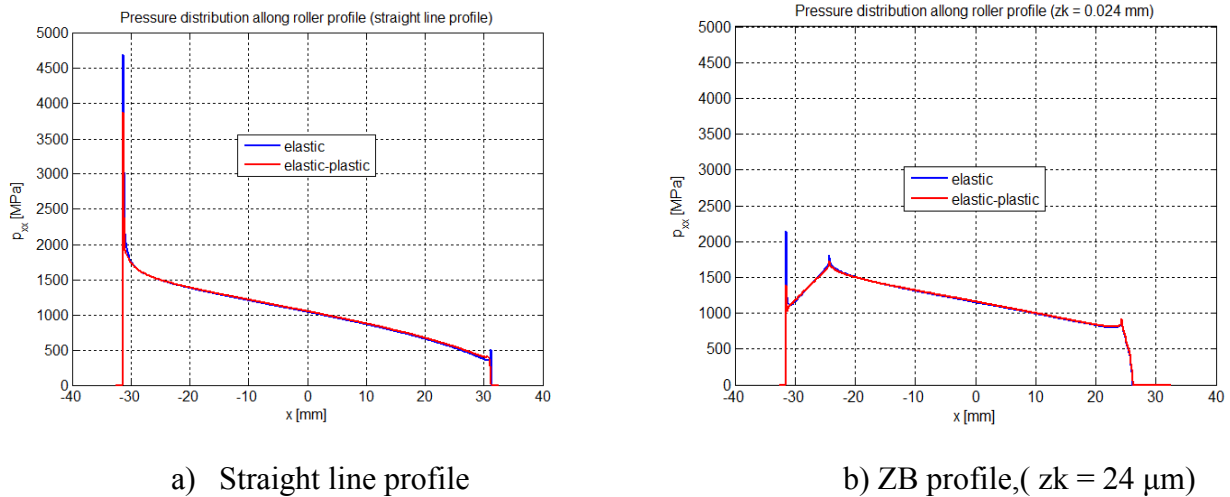


Fig. 9 The pressure distributions for $F_R=100$ kN, before and after a transient overload of 450 kN.

Summary

The running of cylindrical roller bearings in condition of misalignment generates, in the profile's discontinuities points, sharp peaks of the pressure distributions and major increases of von Mises stresses that involve severe reductions of the basic reference rating lives. The local plastic displacements, resulted from the elastic-plastic shakedown process, slightly modify the roller's profile just in its discontinuities points. The new roller profile, stabilized after less than 200 loading cycles, generates significantly lower pressure peaks in the profile discontinuities zones that provides enhanced values for the basic reference rating life.

References

- [1] E. Ioannides, G. Bergling, and A. Gabelli, An Analytical Formulation for the Life of Rolling Bearings, *Acta Polytechnica Scandinavica, Me*, 137, (1999), 1-80.
- [2] ISO /TS 16281: 2008(E), Rolling Bearings - Methods for Calculating the Modified Reference Rating Life for Universally Loaded Bearings, Geneva, Switzerland.
- [3] A. Kapoor and K. L. Johnson, Effect of Changes in Contact Geometry on Shakedown of Surfaces in Rolling/Sliding Contact, *Int. J. Mech. Eng. Sci.*, 34, (1992), 223-239.
- [4] S. Crețu and E. Antalucă, The Study of Non-Hertzian Concentrated Contacts by a GC-DFFT Technique, *Analele U.Galați, VIII, Tribology*, (2003), 39-47
- [5] D. Nélías, E. Antalucă, V. Boucly and S. Crețu, A 3D Semi-Analytical Model for Elastic-Plastic Sliding Contacts, *ASME J. Tribol.*, 129-4, (2007), 761-771.
- [6] S. Cretu, Contactul Concentrat Elastic-Plastic, Polytechnium, Iasi, 2009, 317-333.
- [7] J. Besson, G. Cailletaud, J. L. Chaboche and S. Forest, Non-linear mechanics of materials, Springer, 2010, 76-85.
- [8] J. A. Williams, The influence of repeated loading, residual stresses and shakedown on the behavior of tribological contacts, *Tribol. Int.*, 38, (2005), 786-797.

ON BASIC REFERENCE RATING LIFE OF CYLINDRICAL ROLLER BEARINGS. PART II. ELASTIC-PLASTIC ANALYSIS

S. CREȚU^{a,b*}, M. BENCHEA^a, A. IOVAN-DRAGOMIR^a

^a *Mechanical Engineering Faculty, Technical University ‘Gheorghe Asachi’,
43 D. Mangeron Street, 700050 Iași, Romania*

E-mail: spcretu@mec.tuiasi.com; spiridon.cretu@rkbbearings.com

^b *RKB Bearings, via Primo Agosto, 6828 Balerna, Switzerland*

ABSTRACT

Heavy loads, transient overloads or high misalignments applied to cylindrical roller bearings create uneven pressures distributions with overloading of the yield limit, plastic deformations and shakedown phenomena, able to change the basic rolling contact geometry. To consider these phenomena an elastic-plastic contact model is developed. The model is based on the incremental theory of plasticity comprising the von Mises yield criterion and Prandtl-Reuss equations. Considering isotropic and nonlinear kinematic hardening laws the model accounts for the cyclic hardening phenomena. As result of the elastic-shakedown a new contact geometry is established in less than two hundred of loading cycles. Further, the basic reference rating lives are evaluated using the methodology presented in ISO-16281:2008. The favourable effect of the contact geometry changes due to local plastic deformations is finally revealed.

Keywords: non-Hertzian contact, plastic deformations, kinematic hardening, residual stresses, elastic-shakedown, basic reference rating life.

AIMS AND BACKGROUND

The profile of a cylindrical-crowned roller causes the class I discontinuities at the intersection points of roller profile with the crowning radius as well as at the end chamfers¹. These discontinuities create spikes in the contact pressure distribution²⁻⁵ and diminish the rating life of the bearing¹. On the other hand, these local increases in pressure distribution are able to overcome locally, the yield limit and to induce both plastic deformations and residual stresses⁴. After a certain

* For correspondence.

number of cycles the material will shakedown elastically to a slightly modified roller profile and a stable state of compressive residual stresses⁷. If occurred, these changes have to be considered in the life evaluation. An analysis model has been developed to simulate the nonlinear strain rate dependent deformation of rolling bearing steel stressed in the elastic-plastic domain. The model is developed in the frame of the incremental theory of plasticity by using the von Mises yield criterion and Prandtl-Reuss equations. By considering an isotropic and nonlinear kinematic hardening law the model accounts for the cyclic hardening phenomena.

For the case of cylindrical roller bearings with cylindrical-crowned roller profile, the role played by the crowning geometry on pressure distribution is pointed out for both the elastic analysis and elastic-plastic analysis. Further, the modified rating lives are evaluated using the methodology given in ISO 16281-2008.

THE ELASTIC-PLASTIC MODEL

Material behaviour. For the representation of the yield surface of hardenable alloyed steel it is recommended^{8,9} to use isotropic and kinematic hardening models.

The loading function can be written as:

$$f = \sigma_{eq} - \mathbf{R} - \sigma_Y \quad (1)$$

Isotropic hardening. The isotropic parameter \mathbf{R} is depending on the accumulated plastic strain and defines the change of the yield surface radius.

$$\sigma_s = \sigma_Y + \mathbf{R} \quad (2)$$

where σ_Y and σ_s are the initial and current yield stresses, respectively.

Ramberg-Osgood model for isotropic hardening. This model defines the yielding stress as a function of the equivalent plastic strain ε^p :

$$\sigma_s = \sigma_Y + K_Y (\varepsilon^p)^{1/M_Y} \quad (3)$$

where K_Y is the coefficient of plastic resistance and M_Y is the hardening exponent^{10,11}. The isotropic hardening of the hardened AISI 52100 bearing steel was modelled using the values mentioned by Wang and Kerr (Ref. 10): $K_Y = 5036$ MPa, $M_Y = 8.24$, $E = 210$ GPa.

The number of cycles necessary to induce a steady state of both the plastic deformations and residual stresses (elastic-shakedown) is very small in comparison with the number of loading cycles to induce microstructural changes^{13,14}. Therefore, any cyclic softening was neglected¹¹.

Kinematic hardening. In addition to the stresses caused by the current loading, the equivalent stress takes account of the residual stresses generated by the plastic strains.

CONSTITUTIVE EQUATIONS

Partition hypothesis. In the small perturbation framework the total strain is partitioned into an elastic and plastic strain. This assumption of decoupling the elastic and plastic components allows us to compute total strain increments as a sum of the two components:

$$d\boldsymbol{\varepsilon} = d\boldsymbol{\varepsilon}^e + d\boldsymbol{\varepsilon}^p \quad (4)$$

The Hooke law links the increments of linear elastic strain to stress increments:

$$d\varepsilon_{ij}^e = \frac{1+\nu}{E} d\sigma_{ij} - \frac{\nu}{E} d\sigma_{kk} \delta_{ij} \quad (5)$$

where E is the Young elasticity modulus, ν – the Poisson coefficient of transversal contraction, and δ_{ij} – the Kronecker symbol: $\delta_{ij} = 1$ for $i = j$, and $\delta_{ij} = 0$ for $i \neq j$.

For associated plasticity and inside the framework of Ramberg-Osgood isotropic hardening model, the plastic strain increments are formulated by the Prandtl-Reuss equations^{8,9}:

$$d\varepsilon_{ij}^p = \frac{3}{2} \frac{M_Y}{K_Y} \left(\left\langle \frac{\sigma_{eq} - \sigma_Y}{K_Y} \right\rangle \right)^{M_Y - 1} \frac{d\sigma_{eq}}{\sigma_{eq}} S_{ij} \quad (6)$$

where the angular brackets have the following meaning: $\langle x \rangle = x$ if $x > 0$ and $\langle x \rangle = 0$ if $x \leq 0$.

The loading surface has been considered as described by the von Mises yielding criterion and the increments of total strain become:

$$d\varepsilon_{ij} = \frac{1}{E} \left[(1+\nu) d\sigma_{ij} + \nu d\sigma_{kk} \delta_{ij} \right] + \frac{9}{4} \frac{S_{ij}}{\sigma_{eq}^2} \frac{1}{H'} \left[S_{kk} dS_{kk} + (1 - \delta_{kl}) \sigma_{kl} d\sigma_{kl} \right] \quad (7)$$

where

$$H' = \frac{(K_Y)^{M_Y}}{M_Y (\sigma_{eq})^{M_Y - 1}} \quad (8)$$

In the matrix notation:

$$d\boldsymbol{\varepsilon} = [\mathbf{B}] d\boldsymbol{\sigma} \quad (9)$$

$$d\boldsymbol{\sigma} = [\mathbf{A}] d\boldsymbol{\varepsilon}, \quad [\mathbf{A}] = [\mathbf{B}]^{-1} \quad (10)$$

Incremental algorithm. To attain the final load, the two bodies are incrementally brought into contact^{15,16}. For each new load increment a new elastic pressure distribution is obtained as solution of the system formed by the elastic contact equations. For each load level the internal stresses state is found by using the superposition principle and then the von Mises yield condition is checked. At a certain load increment order, $n + 1$, the yield condition is fulfilled in a number of points inside the stressed volume and the plastic deformations occur. For each of these points the stress and strain tensors are obtained in three steps.

In the first step, the increment of the stress tensor is evaluated as a difference between the successive order components whereas the increment of the total deformation tensor is evaluated by the Hooke law, equation (5) (compatibility technique):

$$d\boldsymbol{\sigma}^{(n+1)} = \boldsymbol{\sigma}^{(n+1)} - \boldsymbol{\sigma}^{(n)} \quad (11)$$

$$d\boldsymbol{\varepsilon}^{(n+1)} = \frac{1}{E} \left[(1 + \nu) d\boldsymbol{\sigma}^{(n+1)} - \nu d\boldsymbol{\sigma}^{(n+1)} \boldsymbol{\delta} \right] \quad (12)$$

In the second step, the increment of the stress tensor is recalculated, equation (10):

$$d\boldsymbol{\sigma}^{(n+1)} = [\mathbf{A}^{(n)}] d\boldsymbol{\varepsilon}^{(n+1)} \quad (13)$$

The increments of the elastic and plastic strains are further found as:

$$d\boldsymbol{\varepsilon}^e{}^{(n+1)} = \frac{1}{E} \left[(1 + \nu) d\boldsymbol{\sigma}^{(n+1)} - \nu d\boldsymbol{\sigma}^{(n+1)} \boldsymbol{\delta} \right] \quad (14)$$

$$d\boldsymbol{\varepsilon}^p{}^{(n+1)} = d\boldsymbol{\varepsilon}^{(n+1)} - d\boldsymbol{\varepsilon}^e{}^{(n+1)} \quad (15)$$

The increments of residual stresses induced by the increments of plastic strain are found as:

$$d\boldsymbol{\sigma}_{ijR}^{*(n+1)} = \frac{E}{1 + \nu} \left[(d\varepsilon_{ij}^p)^{n+1} + \frac{\nu}{1 - 2\nu} (d\varepsilon_{kk}^p)^{n+1} \delta_{ij} \right] \quad (16)$$

Because the boundary conditions require

$$\sigma_{zzR}^{(n+1)}(x, y, 0) = 0 \text{ and } d\sigma_{zzR}^{*(n+1)}(x, y, 0) = 0,$$

a relaxation process^{10,11} has been operated:

$$d\sigma_{xxR}^{(n+1)} = d\sigma_{xxR}^{*(n+1)} - \frac{\nu}{1 - \nu} d\sigma_{zzR}^{*(n+1)} \quad (17)$$

$$d\sigma_{yyR}^{(n+1)} = d\sigma_{yyR}^{*(n+1)} - \frac{\nu}{1 - \nu} d\sigma_{zzR}^{*(n+1)} \quad (18)$$

In the third step, the increments of residual stresses are added to the stresses increments:

$$d\sigma^{(n+1)} = d\sigma^{(n)} + d\sigma_R^{(n+1)} \quad (19)$$

Finally, the stress and plastic strain tensors are:

$$\sigma^{(n+1)} = \sigma^{(n)} + d\sigma^{(n+1)} \quad (20)$$

$$\varepsilon^{p(n+1)} = \varepsilon^{p(n)} + d\varepsilon^{p(n+1)} \quad (21)$$

The evaluation process of plastic strains and residual stresses is performed in the all points where the yielding criterion has been accomplished.

As long as the load attained its final value, the integration of the plastic strains developed along the normal to contact area provides the surface plastic displacements that modify the contact geometry.

Cycling loading and elastic-shakedown. Both, the new contact geometry and residual stresses distribution are further considered as initial values for the next loading cycle, the incremental technique being reiterated with the up-dated values. The cyclic incremental technique continues till the contact geometry and residual stresses no longer change from one cycle to the next, meaning that an elastic shakedown state have been accomplished¹⁷⁻¹⁹.

The evolution of residual stresses depicted in Fig. 1 illustrates the elastic shakedown phenomenon. The way to attain the final state may be different when the load is moving compared to purely vertical loading¹⁰. However, if the shakedown was accomplished, the Melan-Koitter theorems of hardening¹⁷ assure the uniqueness of the related residual stresses state.

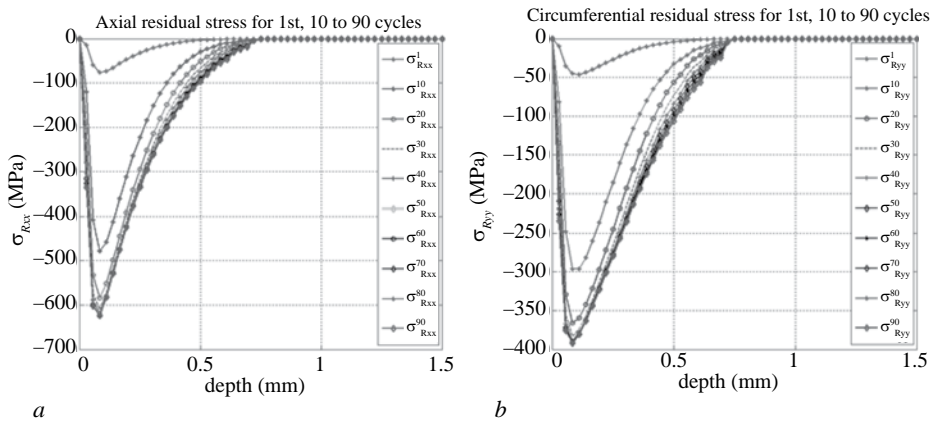


Fig. 1. Residual stresses distributions and elastic shakedown ($F_r = 450$ kN, ZB profile: $z_k = 0.010$ mm)

RESULTS AND DISCUSSION

Profile evolution. Two operating conditions have been considered in the present elastic-plastic analysis; the first one was used in the elastic analysis performed in the paper.

Operating conditions 1: heavy radial load $F_r = 450$ kN and 2 min misalignment.

The plastic displacements after the first loading cycle and after elastic-shakedown are presented in Fig. 2 together with the corresponding modifications in pressure distributions.

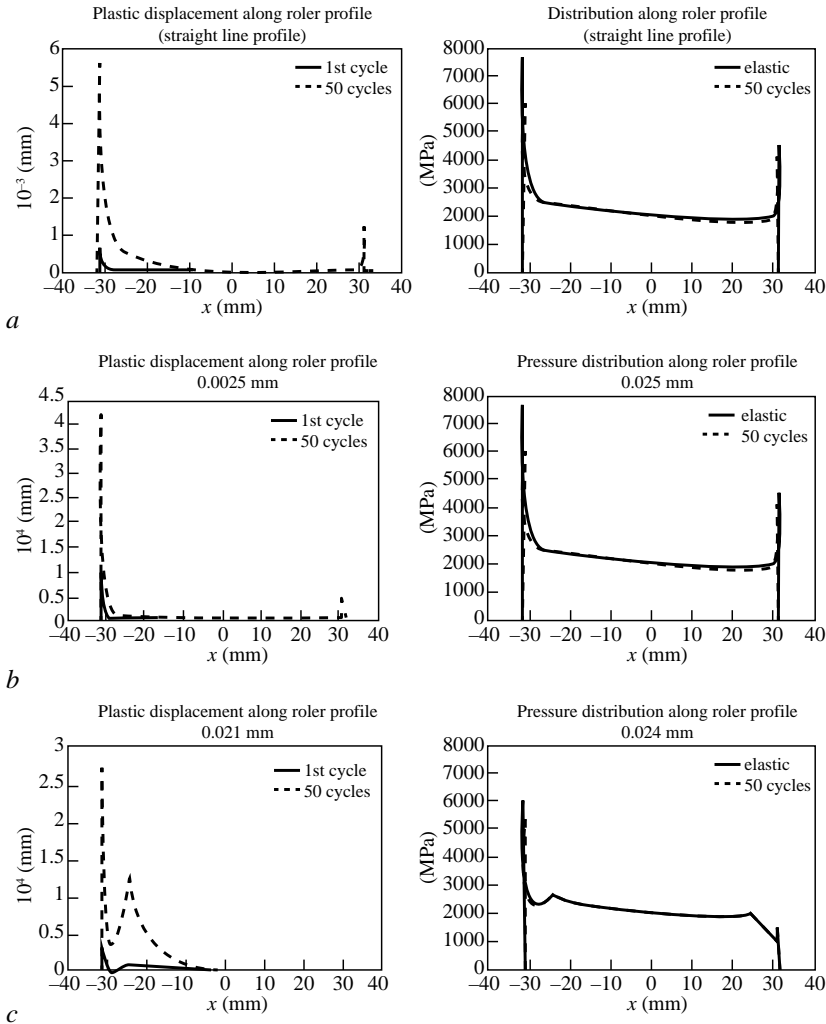


Fig. 2. Profile evolution and the corresponding pressures distributions along roller generatrix (operating load $F_r = 450$ kN, misalignment $\Psi = 2$ min)

a – straight line profile; b – ZB profile, $z_k = 0.0025$ mm; c – ZB profile, $z_k = 0.024$ mm

Basic reference rating lives. The new pressure distributions have been alternatively considered in the evaluation of the basic reference rating life according to ISO-16281 method (Table 1).

Table 1. Fatigue lives for the operating load $F_r = 450$ kN and a misalignment $\Psi = 2$ min. Elastic-plastic analysis

Roller profile	Profile drop z_k (μm)	Basic rating lives L_{10^7} , ISO 281 (Ref. 19) (h)	Basic reference rating lives L_{10^7} , ISO 16281 (Ref. 21) (h)	
			basic profile (elastic analysis)	elastic shakedown profile
Straight	–		3.52	16.7
ZB	2.5	294	4.81	35.5
ZB	10		31.4	42.2
ZB	24		16	37.3

Operating conditions 2: running radial load $F_r = 100$ kN, short transient overload $F_{tr} = 450$ kN and 2 min misalignment. The transient overload F_{tr} is responsible for

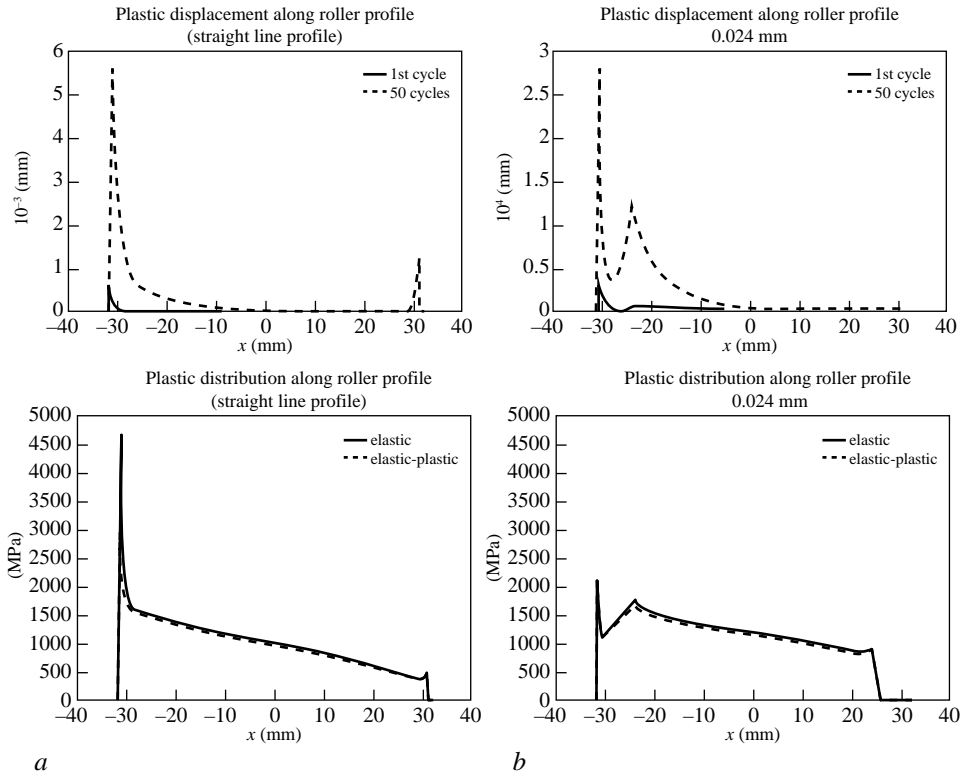


Fig. 3. Profile evolution and the corresponding pressures distributions along roller generatrix (operating load $F_r = 100$ kN, transient overloads $F_{tr} = 450$ kN, misalignment $\Psi = 2$ min) *a* – straight line profile; *b* – ZB profile, $z_k = 0.024$ mm

Table 2. Fatigue lives for the operating load $F_r = 100$ kN with transient overloads $F_{tr} = 450$ kN and a misalignment $\Psi = 2$ min. Elastic-plastic analysis

Roller profile	Profile drop z_k (μm)	Basic rating lives L_{10} , ISO 281 (Ref. 21) (h)	Basic reference rating lives L_{10r} , ISO 16281 (Ref. 22) (h)	
			basic profile (elastic analysis)	elastic shakedown profile
Straight	–		163	757
ZB	2.5	44300	1720	1760
ZB	10		4950	9860
ZB	24		10200	10800

the profile changes, as is depicted in Fig. 3. The pressure distribution due to the operating load $F_r = 100$ kN are represented in Fig. 3 and the corresponding rating lives are given in Table 2. The results reveal that a very short overload, able to induce small alterations of roller profile, may attenuate the pressure peaks with beneficial effect upon basic reference rating life.

CONCLUSIONS

The existing discontinuities along roller generatrix generate sharp increases in pressure distributions that may led to slight changes of roller profile against the basic design.

A fast solver has been developed to obtain the pressure distributions in non-Hertzian contacts loaded in elastic as well as elastic-plastic conditions.

The cyclic evaluation process of the plastic strains and residual stresses is performed until the material shakedowns.

The methodology presented in ISO-16281:2008 has been involved to evaluate the basic reference rating lives. The favourable effect of roller profile changes as result of the local plastic deformations has been revealed.

An elastic-plastic approach can provide a more realistic evaluation of the basic reference rating life of roller bearings that are running in heavy loading conditions, presence of transient overloads or notably misalignments.

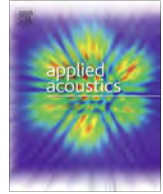
REFERENCES

1. T. A. HARRIS, M. M. KOTZALAS: Rolling Bearings Analysis – Advanced Concepts of Bearing Technology. CRC Press Taylor & Francis Group LLC, Boca Raton, FL, 2007.
2. M. J. DE MUL, J. J. KALKER, B. FREDRIKSSON: The Contact between Arbitrarily Curved Bodies of Finite Dimensions. ASME J Tribol, **108**, 140 (1986).
3. S. CREȚU, E. ANTĂLUCĂ: The Study of Non-Hertzian Concentrated Contacts by a GC-DFFT Technique. Annals of University of Galați, **VIII** (Tribology), 39 (2003).

4. C. I. BARBINTA, S. CREȚU: Modification of Wheel-Rail Contact Parameters by Wear. *J Balk Tribol Assoc*, **19** (3), 412 (2013).
5. S. CREȚU, M. BENCHEA, A. DRAGOMIR-IOVAN: On Basic Reference Rating Life of Cylindrical Roller Bearings. Part 1. Elastic Analysis. *J Balk Tribol Assoc*, **21** (4), 820 (2015).
6. A. KAPOOR, L. K. JOHNSON: Effect of Changes in Contact Geometry on Shakedown of Surfaces in Rolling/Sliding Contact. *Int J Mech Eng Sci*, **34**, 223 (1992).
7. M. BENCHEA, A. DRAGOMIR-IOVAN, S. CREȚU: Misalignment Effects in Cylindrical Roller Bearings. *Applied Mechanics and Materials*, Trans Tech Publication, Switzerland, **658**, 277 (2014).
8. I. LINARES ARREGUI, B. ALFREDSSON: Elastic-Plastic Characterization of a High Bainitic Roller Bearing Steel-Experiments and Modelling. *Int J Mech Sciences*, **52**, 1254 (2010).
9. T. CHAISE, D. NELIAS: Contact Pressure and Residual Strain in 3D Elasto-Plastic Rolling Contact for a Circular or Elliptical Point Contact. *ASME J Tribol*, **133**, 41 (2011).
10. J.-L. CHABOCHE: A Review of Some Plasticity and Viscoplasticity Constitutive Theories. *Int J Plasticity*, **24**, 1642 (2008).
11. J. BESSON, G. CAILLETAUD, J.-L. CHABOCHE, S. FOREST: *Nonlinear Mechanics of Materials*. Springer, 2010.
12. F. WANG, L. KEER: Numerical Simulation for Three Dimensional Elastic-Plastic Contact with Hardening Behavior. *ASME J Tribol*, **127**, 494 (2005).
13. P. A. VOSKAMP: Material Response to Rolling Contact Loading. *ASME J Tribol*, **107** (2), 359 (1985).
14. F. SADEGHI, B. JALALAHMADI, S. T. SLACK, N. RAJE, K. N. ARAKERE: A Review of Rolling Contact Fatigue. *ASME J Tribol*, **131** (4), 681 (2009).
15. A. N. PALAZOTTO, F. N. MORRIS: An Elastic-Plastic Plane Stress Solution Using the Incremental Theory. *Int J of Mech Sci*, **13**, 97 (1971).
16. S. CREȚU, V. HATMANU: A Numerical Analysis of Permanent Deformation in Elastic-Plastic Line Contact. *Bul Inst Polit Iași*, **XXXI** (1-4), 19 (1985).
17. L. K. JOHNSON: The Application of Shakedown Principles in Rolling and Sliding Contact. *Eur J Mech Solids*, **11**, 55 (1992).
18. A. KAPOOR, J. A. WILLIAMS: Shakedown Limits in Sliding Contacts on a Surface Hardened Half-Space. *Wear*, **172**, 206 (1994).
19. J. A. WILLIAMS: The Influence of Repeated Loading, Residual Stresses and Shakedown on the Behavior of Tribological Contacts. *Tribol Int*, **38**, 86 (2005).
20. S. CREȚU: Concentrated Elastic-Plastic Contact. Politehniem, Iași, 2009 (in Romanian).
21. ISO 16281: Rolling Bearings—Methods for Calculating the Modified Reference Rating Life for Universally Loaded Bearings. ISO/TS 16281:2008, ISO, Geneva, Switzerland.
22. ISO 281: Rolling Bearings—Dynamic Load Ratings and Rating Life. ISO 281:2007, ISO, Geneva, Switzerland.

Received 25 May 2015

Revised 29 July 2015



Technical note

Experimental and theoretical considerations on sound absorption performance of waste materials including the effect of backing plates



Carmen Bujoreanu ^{*}, Florin Nedeff, Marcelin Benchea, Maricel Agop

Mechanical Engineering, Mechatronics & Robotics Department, Mechanical Engineering Faculty, "Gheorghe Asachi" Technical University of Iasi, 43 Str. Prof. Dr. Doc. Dimitrie Mangeron, 700050 Iasi, Romania

ARTICLE INFO

Article history:

Received 21 September 2016

Received in revised form 21 December 2016

Accepted 22 December 2016

Keywords:

Sound absorption coefficient

Sound transmission

Waste material

Backing plate

Third octave analysis

ABSTRACT

The acoustic human comfort includes the protection from noise and it is closely related to the sound absorption concept. The paper presents an experimental study on sound absorption coefficients, including transmission, for some combined materials: waste materials (rubber particles, polypropylene, crumbled plastic, wood flour, jute and cord fabrics) with different backing plates (plasterboard, oriented strand board - OSB, polystyrene). The tests were realized following the impedance tube method (ISO 10534-1:1998 standard), except for that the end of the tube was inserted into an anechoic room. The effect of this "backing room" on the samples sound absorption performances is discussed. Also, the experimental results emphasize the influence of the combined materials placed in series on the sound absorption performances and promote the idea of environmentally friendly solutions in their improvement.

© 2016 Elsevier Ltd. All rights reserved.

1. Introduction

The technological development of all the industries (automotive, construction, environmental and equipment manufacturing) that creates powerful and noisy systems requires more efficient and cheap sound absorptive materials in order to achieve the acoustic human comfort. This is connected to the sound absorption concept. Absorption coefficient quantifies how much sound is absorbed by the material and transmission through it. When the sound reaches the material, its energy is absorbed and reflected, depending on the sound absorption performance of the material [1]. For instance, the buildings walls and roofs constitute the backing for different materials that need to have a high absorption coefficient, as wool glass, foam or mineral fibers and their composites.

There are studies that reinforce the idea of the use of some materials combinations, resulting in different structures of thickness and density, influencing the sound absorption properties of the new created material [2,3]. Recently, human health and environmental protection have become another major requirements leading to natural materials use in practical applications. Therefore, another series of experimental studies on sound absorption coefficient focuses on some natural materials and their

combination (bamboo fiberboard, coconut fibers, and tea leaf fibers) [4,5]. As a result, good sound absorption coefficients similar to those for metallic foams or sinterized materials were reported.

This paper experimentally investigates and then compares the sound absorption coefficients including the transmission to behind of several samples consisting of waste materials (rubber particles, polypropylene, crumbled plastic, wood flour, jute and cord fabrics) with different backing plates (plasterboard, oriented strand board - OSB, polystyrene). The samples (considered combined materials placed in series) were tested in an anechoic room using the ISO 10534-1:1998 standard. The testing procedure was modified in that the anechoic room represents the "backing itself" of the tube, replacing the rigid wall from the standard procedure. As the materials sound absorption properties are very dependent on the way the material is mounted, the investigation of the material absorptive performance in a certain position in space is of interest.

The sound absorption study of some materials based on different backing plates, in different combinations, highlights the possibility of cheap and efficient constructive solutions to provide better absorptive materials.

2. Experimental investigation

2.1. Method and material

The absorption coefficient of a material varies with frequency and with the angle at which the sound wave strikes the material.

^{*} Corresponding author.

E-mail addresses: carmen.bujoreanu@gmail.com (C. Bujoreanu), florin_nedeff@yahoo.com (F. Nedeff), marcelin.benchea@tuiasi.com (M. Benchea), m.agop@yahoo.com (M. Agop).

When sound waves hit a surface, as energy conservation, (Fig. 1), it can be expressed [6]:

$$E_i = E_r + E_a + E_t \quad (1)$$

The absorption coefficient is defined as ratio of absorbed energy to incident energy:

$$\alpha = \frac{E_a}{E_i} \quad (2)$$

Also, the absorption coefficient, α , can be defined as the ratio of all energy not reflected to incident energy:

$$\alpha = 1 - \frac{E_r}{E_i} = \frac{E_a + E_t}{E_i} \quad (3)$$

Absorption coefficient measurements usually are made in a reverberant room, according to the ISO 354:2003 standard [7]. Using this standard, it has been reported influences of sample placement in the room and sample edge effects on the accuracy of the measurements [8].

As well, it is used the standing wave tube technique, presented in part 1 of the ISO 10534:1998 standard [9] and the transfer function method described in part 2 of this standard. The first part of the standard settles the measurements of the ratio of peak to minimum amplitude in a standing wave tube in order to determine the magnitude and phase of the pressure reflection coefficient, and then the sound absorption coefficient, α . The second part of the standard describes the use of the transfer function H between two spaced microphones and also spaced from sample in order to get pressure reflection coefficient, r [10,11]. ISO 10534:1998 standard can be applied if there are no reflected waves resulting from other systems than the tested samples, meaning that measurements based on these methods have to be carried out in open spaces or rooms that have sound insulation [12]. The measured upper frequency is limited to the plane waves frequencies which can travel in the tube depending of the sound speed and the tube diameter [6].

None of these procedures allows making measurements in situ, furthermore the experimental methodologies are quite different, and so the obtained values for the sound absorption coefficients have a great dispersion from an author to another [13].

To summarize, we may consider that the sound absorption coefficient obtained from the reverberation room method is the ratio of the absorbed energy by the test sample to the incident sound energy, while the sound absorption coefficient measured in an impedance tube is defined as the ratio of the non-reflected sound energy to the incident sound energy [14].

The standard impedance tube method supposes that the sample is backed by a rigid termination/wall. If the rigid backing is replaced by an anechoic termination, then the measured sound absorption coefficient obtained for this case includes both the energy dissipated inside the material and the energy transmitted through the material and propagated to the anechoic terminal.

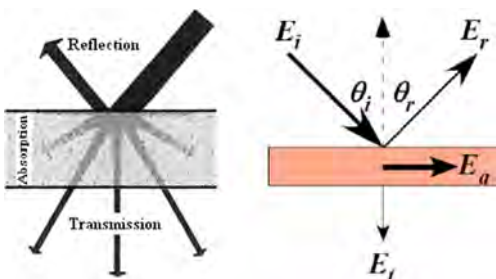


Fig. 1. Sound energy conservation.

When the sample is backed by a rigid plate this latter term disappears and the sound absorption coefficient rating is the same as that for the standard impedance tube method defined by the corresponding ISO standards [14].

Taking into account that we have in the department an anechoic room, we performed our experimental work based on a modified impedance tube method (ISO 10534-1:1998 standard). The anechoic end of the impedance tube is the anechoic room itself.

In practical cases, the energy dissipated inside a material when it is directly mounted on a wall is close to the result from the standard tube configuration [14]. As well, a lot of materials can be freely-hanging in space and the sound transmission loss through the material must be considered. Therefore, it can be of interest for practical situations to explore the effect of the anechoic cavity, as backing, in order to estimate the sound absorption coefficient values.

Fig. 2 presents the experimental setup for the sound absorption coefficients. It consists of: signal random generator, microphone, soundmeter connected with the microphone and NIDAQ board, laptop with LabVIEW soft compatible with National Instruments DAQPad for data processing. The signal generator connected to the loudspeakers emits waves travelling to the other end of the tube, where the tested samples are well fastened.

The samples are realized from different combinations of waste/recycled materials (plastic, wood flour, rubber, polypropylene, jute fabric, cord fabric) bonded on backing plate made of some usual construction materials for room walls and roofs (plasterboard, polystyrene, OSB-oriented strand band). The bonding solution is a water-based agent, ecological and without chemical reactivity.

Therefore, some materials are layered together to make a new structure in practice and it is necessary to get the acoustic properties of the whole structure. The total reflected sound wave at the interface of two or more layers of materials is the summation of the infinite number of reflections at the surfaces [14]. In a standard configuration, the material is backed by a rigid wall. It can be considered as two layers of materials placed in series with the reflection coefficient of the second one equal to unity [14]. We can think about this standard configuration as a particular case of the general situation when the end of the tube has an anechoic termination. The anechoic room is the back cavity replacing the rigid wall from the standard procedure.

In the impedance tube the waves are reflected back from the sample and received by the microphone measuring the incident and reflecting sound pressure. The samples with a diameter of 10 cm were prepared according to the tube size and the third octave analysis with LabVIEW soft is performed in frequencies band ranging from 63 to 2000 Hz.

The tested samples are noted:

The appearance characteristics of the tested samples are depicted in Fig. 3.

2.2. Experimental results and discussions

We have measured the sound pressure level dB(A), A weighted, of incident and reflected wave, using the LabVIEW soft with the *third-octave analysis* tool. Values are usually provided in the literature at the standard frequencies of 125, 250, 500, 1000 and 2000 Hz [15].

Specifications for this tool included in LabVIEW library are defined by ANSI and International Electrotechnical Commission (IEC) standards and the results are fully compliant to the international standards (ANSI S1.11-2004 and the IEC 1260:1995 standards). The absorption coefficient under a certain frequency is determinate according to ISO 10534-1:1998 standard. Each sample was tested 3 times and the averaged values are considered.

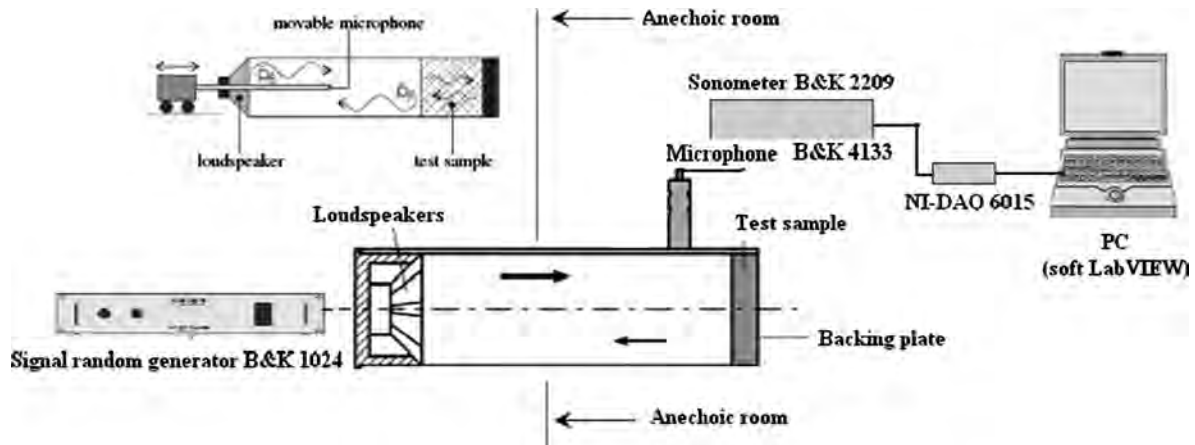


Fig. 2. Experimental setup, using the anechoic room, for the sound absorption coefficients.

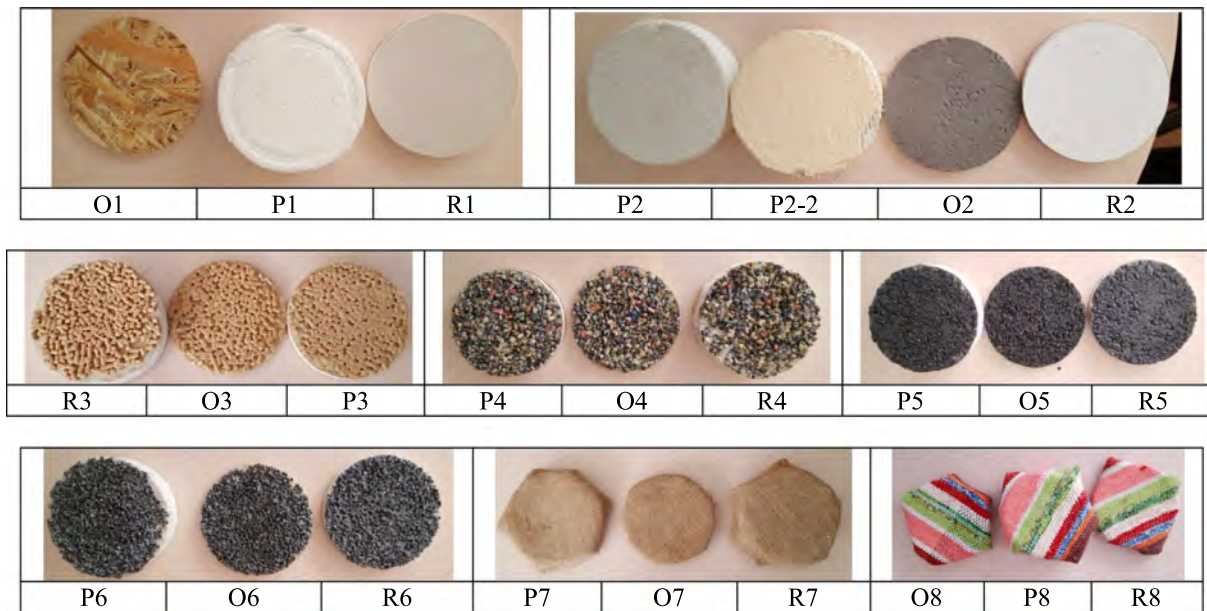


Fig. 3. Tested samples.

Our method of impedance tube without rigid backing is not a usual way to measure absorption performance. The energy dissipated inside a material together with the transmitted energy through this material is propagated to the anechoic room. When the sample is backed by a rigid plate, the sound transmission loss is negligible and we have the same situation as that for the impedance tube method defined by the corresponding ISO standards [14]. Therefore the absorption coefficient values in our work are lower than those obtained through standard measurements (with rigid backing of the tube end).

Figs. 4–6 describe the relation between frequency and sound absorption coefficients, α , of samples with three backing materials covered with different waste materials, as it is denoted in Table 1. Note that these absorption coefficients include sound transmission.

The tested samples with plasterboard backing have sound absorption coefficients greater at low frequencies (125–250 Hz) than at high frequencies (1000–2000 Hz). From the Fig. 4, it is obvious that the deposition of the granular or grinded materials (see Table 1) on the plasterboard plates increases the sound absorptive properties of the new created materials.

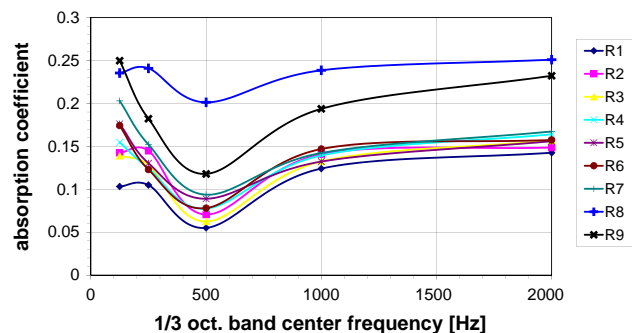


Fig. 4. Sound absorption coefficients of tested samples with plasterboard backing (the absorption coefficients include sound transmission).

However, the sound absorption of the composed materials thus created is dominated by the R8 sample (the plasterboard is covered with cord fabric). The simplicity of the fabric and also its natural origin, environmentally friendly, give to this combination (expressed in R8 sample) a good potential in sound absorption.

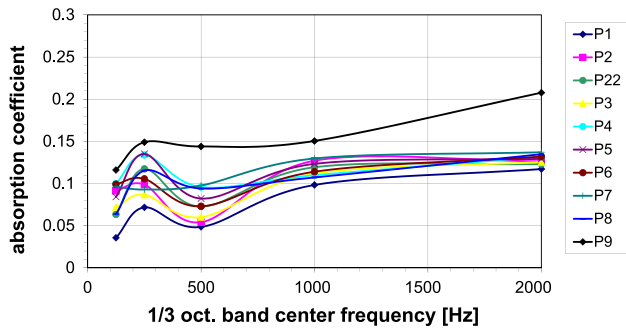


Fig. 5. Sound absorption coefficients of tested samples with polystyrene backing (the absorption coefficients include sound transmission).

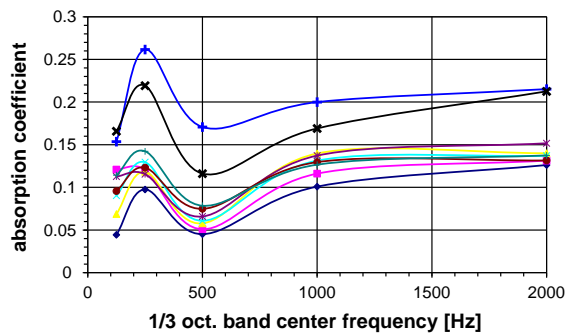


Fig. 6. Sound absorption coefficients of tested samples with OSB backing (the absorption coefficients include sound transmission).

Also, a natural textile material bonded on the plasterboard backing (R9) seems to have an increase sound absorption coefficient compared to the other combinations from Fig. 4. In the figure, it can be observed a drop in sound absorption at approx. 500 Hz.

Fig. 5 reports the sound absorption performances of the materials with polystyrene backing, from Table 1. We can recognize better sound absorption behaviour at 2000 Hz than at frequencies below this one, for almost all these type of samples. The sample P9, which is a natural textile material on polystyrene, has the highest values for the sound absorption coefficient, even at 500 Hz, although it is observed a decrease for almost all the other materials.

Fig. 6 describes the evolution of sound absorption coefficients for the samples with oriented strand band (OSB) backing. The samples O1–O7 have sound absorption coefficients without significant variations in the interest frequency band, excepting the decrease recorded at 500 Hz. There are good sound absorption properties (noting the values recorded at 250 Hz) for samples O8, then O9, which are made of cord and jute fabric, respectively, bounded on the OSB backing.

In the next Figs. 7–15 we have realized a comparative analysis of sound absorption coefficients of the tested samples from the point of view of covering materials.

It can be seen that, from our measurements, the plasterboard sample R1 has greater sound absorption coefficients compared to polystyrene and OSB samples, as resulting from Fig. 7. Although the simple polystyrene sample P1 has the greatest thickness among the backing plates, it recorded poor sound absorption. The OSB plate, O1, denser and the thinnest sample, has also the sound absorption behaviour comparable with the sample R1 at low frequency of 125 Hz. However, the thickness is important on low frequency sound absorption, as low frequency means larger wavelength and larger wavelength sound can be absorbed if the

Table 1
Samples codes and their characteristics.

Tested sample code	Materials combination	Diameter/Mean thickness [mm]
R1	Simple plasterboard	100/15
R2	Whitewashed plasterboard	100/15
R3	Plasterboard covered with wood flour	100/15
R4	Plasterboard covered with crumbled plastic	100/15
R5	Plasterboard covered with polypropylene granules	100/15
R6	Plasterboard covered with rubber granules	100/15
R7	Plasterboard covered with jute fabric	100/15
R8	Plasterboard covered with cord fabric	100/15
R9	Plasterboard covered with jute fabric on the backing both surfaces	100/15
P1	Simple polystyrene	100/40
P2	Plaster polystyrene with meshing	100/40
P2-2	Plaster polystyrene with meshing and whitewashed	100/40
P3	Finished polystyrene covered with wood flour	100/40
P4	Finished polystyrene covered with crumbled plastic	100/40
P5	Finished polystyrene covered with polypropylene granules	100/40
P6	Finished polystyrene covered with rubber granules	100/40
P7	Finished polystyrene covered with jute fabric	100/40
P8	Finished polystyrene covered with cord fabric	100/40
P9	Finished polystyrene covered with jute fabric on the backing both surfaces	100/40
O1	Simple OSB without cover material	100/5
O2	Painted OSB	100/5
O3	OSB covered with wood flour	100/5
O4	OSB covered with crumbled plastic	100/5
O5	OSB covered with polypropylene granules	100/5
O6	OSB covered with rubber granules	100/5
O7	OSB covered with jute fabric	100/5
O8	OSB covered with cord fabric	100/5
O9	OSB covered with jute fabric on the backing both surfaces	100/5

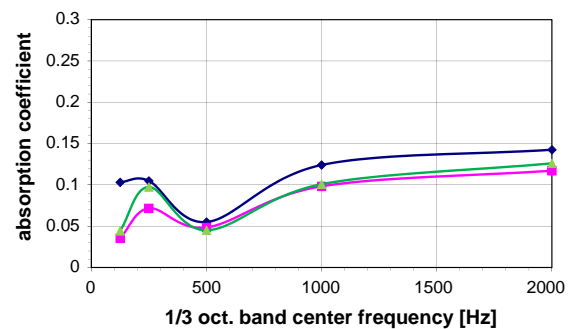


Fig. 7. Sound absorption coefficients including transmission.

material is thicker. Thickness at higher frequencies has insignificant effect on sound absorption [16].

The recycled materials covering the backing plates bring changes in the sound absorption behaviour, as it is presented in Figs. 8–15. Whitewashing and painting the backing plates (R2 and O2 from Fig. 8) lightly raise the sound absorption coefficients of the initial samples, highlighting the surface effects. The wood flour bonded on the backing plates (Fig. 9) don't have significant influence on samples sound absorption, while the crumbled plastic (Fig. 10) and the propylene granules (Fig. 11) on polystyrene back-

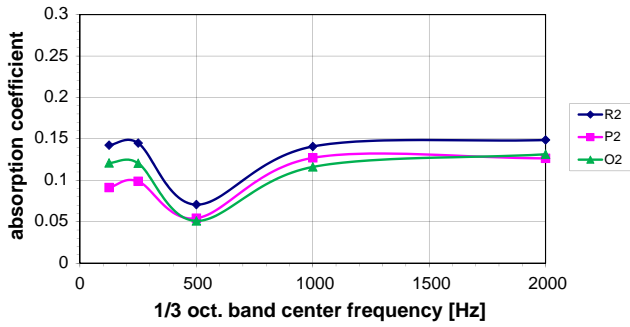


Fig. 8. Sound absorption coefficients including transmission.

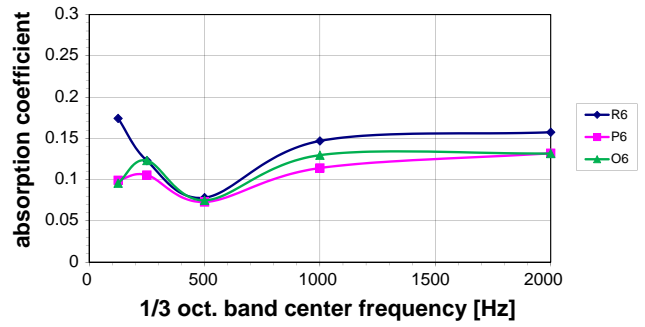


Fig. 12. Sound absorption coefficients including transmission.

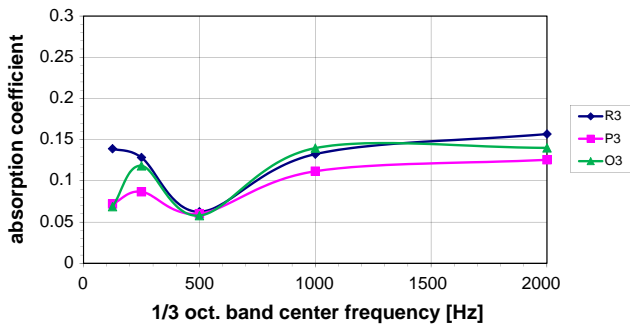


Fig. 9. Sound absorption coefficients including transmission.

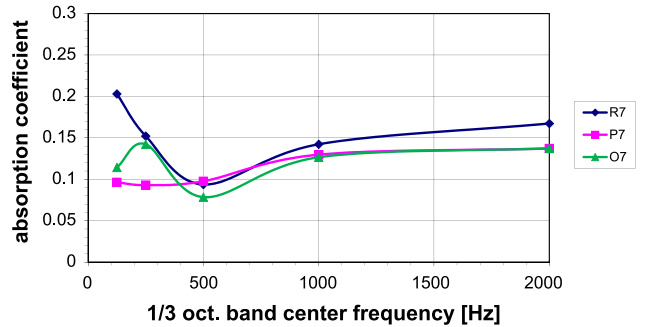


Fig. 13. Sound absorption coefficients including transmission.

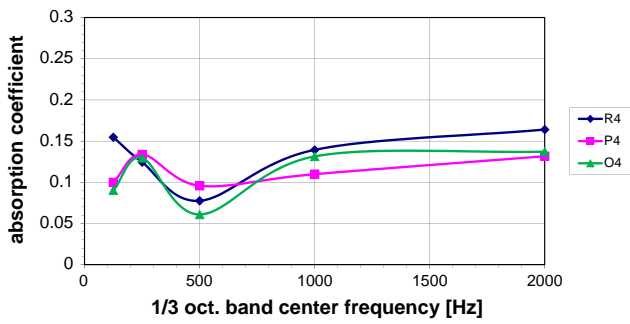


Fig. 10. Sound absorption coefficients including transmission.

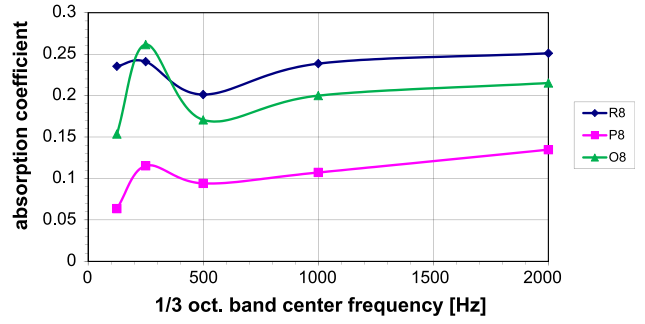


Fig. 14. Sound absorption coefficients including transmission.

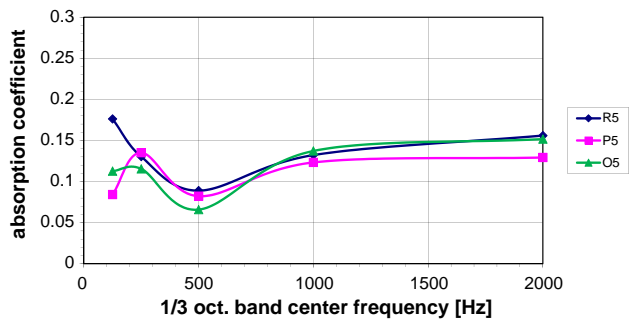


Fig. 11. Sound absorption coefficients including transmission.

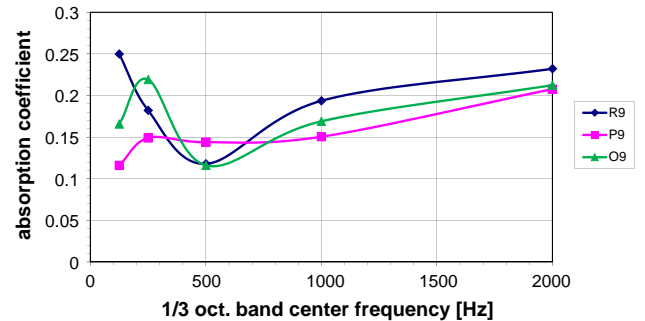


Fig. 15. Sound absorption coefficients including transmission.

ing plate represent materials with higher sound absorption coefficients, especially at lower frequencies. The samples with rubber granules as coating layer (Fig. 12) demonstrate that at low frequency they have lower sound absorption behaviour, mainly on polystyrene backing.

Figs. 13–15 reports the sound absorption performances of the sample consisting in textiles (jute and cord fabrics) bonded on the backing plates. The jute fabric on the backing both surfaces (Fig. 15) increases the sound absorption properties of the samples compared to the situation when the backing is covered by the jute

fabric on a single surface (Fig. 13). As well, the cord fabric with backing (Fig. 14) represents a better absorptive material than those previously described.

The reported results included in the Figs. 7–15 (note that these absorption coefficients include sound transmission) show a drop in sound absorption at 500 Hz. It is possible that at this frequency a non-axisymmetric sound field to be created as result of the excitation of a vibration mode of the acoustic waves [8].

The literature agrees that the behaviours of the materials are totally different in different configurations and are very dependent on the material concerned [14]. The classic theoretical models must be adapted to these situations.

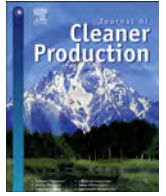
3. Conclusions

The paper first presents an experimental investigation on the sound absorption coefficients behaviour, including the effect of the backing walls, of some combined materials: waste materials (rubber particles, polypropylene, crumbled plastic, wood flour, jute and cord fabrics) bonded on the usual construction materials of plasterboard, polystyrene and OSB. The tests were realized using the tube end inserted into an anechoic room. The effect of this backing cavity on the samples acoustic performances, in terms of sound absorption, is discussed. As consequence, the absorption coefficient values in our work are lower than those obtained through standard measurements (with rigid backing of the tube end). The one layer material covering the backing plate leads to the increase of sound absorption of the sample thus created. The results highlight that the samples including textile materials (jute and cord fabrics) have better sound absorption properties in the exploited frequency band. This fact is also important for the environment and the human health. The backing of plasterboard with a single layer of any used waste material has sound absorption properties better when compared to samples with polystyrene backing, even their thickness is greater. Similar behaviour is recorded for the thinner samples with OSB base. The backing plates density of the samples influences the sound absorption properties more than their thickness.

The study of the particles size and thickness of the waste materials covering the backing plates could extend this current work. The paper draws attention on the possibility of cheap and efficient constructive solutions to provide better sound absorption properties.

References

- [1] Cavanaugh William J, Tocci Gregory C, Wilkes Joseph A, *Acoustics Architectural. Principles and practice*. Wiley; 2009.
- [2] Ersoy Sezgin, Küçük Haluk. Investigation of industrial tea-leaf-fiber waste material for its sound absorption properties. *Appl Acoust* 2009;70:215–20.
- [3] Hong Z, Bo L, Guangsu H, Jia H. A novel composite sound absorber with recycled rubber particles. *J Sound Vib* 2007;304:400–6.
- [4] Nor MJM, Jamaluddin N, Tamiri FM. A preliminary study of sound absorption using multi-layer coconut coir fibres. *Techn Acoust Electron J* 2003;3.
- [5] Shahani Fereshteh, Soltani Parham, Zarrebini Mohammad. The analysis of acoustic characteristics and sound absorption coefficient of needle punched nonwoven fabrics. *J Eng Fibers Fabr* 2014;9(2):84–92.
- [6] Muehleisen Ralph T. *Measurement of the acoustic properties of acoustic absorbers*. Illinois Institute of Technology; 2011.
- [7] ISO 354:2003. *Acoustics - measurement of sound absorption in a reverberation room*.
- [8] Wijnant YH, Kuipers ER, de Boer IrA. Development and application of a new method for the in-situ measurement of sound absorption. *Proc Isma* 2010:109–22.
- [9] ISO 10534:1998. *Acoustics - determination of sound absorption coefficient and impedance in impedance tubes: Part 1: Method using standing wave ratio, Part 2: Transfer-function method*.
- [10] Chung JY, Blaser DA. Transfer function method of measuring in-duct acoustic properties. Part I: Theory. *J Acoust Soc Am* 1980;68(3).
- [11] Chung JY, Blaser DA. Transfer function method of measuring in-duct acoustic properties. Part II: Experiment. *J Acoust Soc Am* 1980;68(3).
- [12] Wijnant YH, Kuipers ER, de Boer A. An alternative coefficient for sound absorption. *Proc Isma* 2012:85–94.
- [13] Farina Angelo, Torelli A. Measurement of the sound absorption coefficient of materials with a new sound intensity technique, AES convention: 102 paper number: 4409; 1997. p. 1–18.
- [14] Feng Leping. Modified impedance tube measurements and energy dissipation inside absorptive materials. *Appl Acoust* 2013;74:1480–5.
- [15] Takahashi YT, Otsuru, Tomiku R. In situ measurements of surface impedance and absorption coefficients of porous materials using two microphones and ambient noise. *Appl Acoust* 2005;66:845–65.
- [16] Seddeq Hoda S. Factors influencing acoustic performance of sound absorptive materials. *Aust J Basic Appl Sci* 2009;3(4):4610–7.



Considerations on sound absorption coefficient of sustainable concrete with different waste replacements

Irina Oancea^{a,*}, Carmen Bujoreanu^{b,**}, Mihai Budescu^a, Marcelin Benchea^b,
Cătălina Mihaela Grădinaru^c

^a Department of Structural Mechanics, Faculty of Civil Engineering and Building Services, “Gheorghe Asachi” Technical University of Iasi, 43 Str. Prof. Dr. Doc. Dimitrie Mangeron, 700050 Iasi, Romania

^b Mechanical Engineering, Mechatronics & Robotics Department, Mechanical Engineering Faculty, “Gheorghe Asachi” Technical University of Iasi, 43 Str. Prof. Dr. Doc. Dimitrie Mangeron, 700050 Iasi, Romania

^c Department of Concrete Structures, Building Materials, Technology and Management, Faculty of Civil Engineering and Building Services, “Gheorghe Asachi” Technical University of Iasi, 43 Str. Prof. Dr. Doc. Dimitrie Mangeron, 700050 Iasi, Romania

ARTICLE INFO

Article history:

Received 27 March 2018
Received in revised form
10 August 2018
Accepted 26 August 2018
Available online 27 August 2018

Keywords:

Sustainable concrete
Waste aggregates
Acoustic coefficient
Noise barriers

ABSTRACT

In the context of an urban environment assaulted by noise from different sources, the possibility of using composite materials made of concrete and various materials considered as waste was investigated, for the purpose of using them in acoustic barriers. Five different types of sustainable concrete have been developed, incorporating polystyrene granules, polyethylene terephthalate granules, corn cob granules, shredded sunflower stalk and balls made of sheep wool. Two different thicknesses were adopted, of 40 mm and 80 mm. The influence of the material's thickness was investigated. For these materials, the acoustic absorption coefficient was determined, using Feng's modified procedure of the ISO 10534:1998 standard. The sound absorption coefficient's meaning suffers changes and its measured value can be considered the real one, smaller than the usual reported standard values. Each of the sustainable concrete has sound absorption coefficients higher than those of the conventional concrete. The results highlighted that these types of materials represent a sustainable solution for both waste and noise problems of our cities.

© 2018 Elsevier Ltd. All rights reserved.

1. Introduction

Urban development in the last century, often chaotic, has led to the emergence of important issues in terms of the comfort we feel in today's cities. We speak of comfort, referring to all its components, including the thermal comfort, influenced by the phenomenon of the city's heat island, the visual comfort, as well as the acoustic. Acoustic comfort is a component of urban comfort, the importance of which is recognized by physicians in particular, and has become an increasingly important concern for both civil engineering and urban design. By joining this problem with the one generated by waste, we can find a link so that civil engineering has a positive contribution to reducing the environmental impact of

pollution, while at the same time bringing benefits to increasing acoustic comfort in urban areas. This link may consist of the use of various materials considered waste in the development of new materials that can be used in construction, with superior quality to classical materials. The incorporation of various wastes has been studied by many researchers, aiming at both mechanical behavior of new materials (Cook, 1983; Ferrandiz-Mas and Garcia-Alcocel, 2012; Felix et al., 2013) and acoustic behavior as well (Kim and Lee, 2010; Ghizdavet et al., 2016).

In this study the authors aimed to determine the sound absorption coefficients of composite materials made of concrete and various embedded wastes. The energy dissipated inside the material plus transmitted energy is the definition of absorption. The new materials can be used in the realization of acoustic barriers and our study results highlighted that these types of materials represent a sustainable solution for both waste and noise problems of our cities. The authors chose to embed in concrete different types of waste, expanded polystyrene granules (EPS), polyethylene terephthalate (PET) granules, but also vegetal and animal waste, as the

* Corresponding author.

** Corresponding author.

E-mail addresses: irina.oancea@tuiasi.ro (I. Oancea), carmen.bujoreanu@gmail.com (C. Bujoreanu).

quantity of these wastes that we generate is unexpectedly high. All of these wastes have been studied, as presented next, but the authors' idea is to see if they can contribute to enhance the sound comfort that we experience outdoors, by using them in creating sound barriers. The use of waste materials for creating panels for noise barriers is an important factor in determining their sustainability, as shown by [Oltean-Dumbrava and Miah \(2016\)](#).

Since conventional aggregates (sand and gravel) represent an exhaustible resource and approximately 60–80% of the volume of concrete, their partial or total replacement with artificial or natural waste contributes to the conservation of natural resources.

For an easier comparison between different materials, it is useful to use a single number to describe the sound absorption coefficients of each material. For this reason, the notion of Noise Reduction Coefficient (NRC) has been introduced, having the value equal to the arithmetic average of the sound absorption coefficients depending on frequency. NRC rating of a material is intended to be a simplified indicator and can be considered as a percentage. The NRC values are ranged from 0.00 (perfectly reflective) to 1.00 (perfectly absorptive).

The artificial wastes imbedded in concrete in this research are EPS and PET, materials used at a very large scale in different applications. Polystyrene granules can be easily incorporated into concrete to produce light-weight concrete with a wide range of densities. EPS granules are classified as an artificial ultralightweight aggregate (density less than 33 kg/m^3) with a non-absorbent, hydrophobic and closed cell nature ([Chen et al., 2010](#)). The NRC for a 50 mm thickness layer of granular foamed polystyrene is 0.32 ([Sikora and Turkiewicz, 2010](#)). The NRC of 0.32 means that 32% of the energy of incident sound waves reaching the material is absorbed and is not reflected back, therefore the absorption properties of the material may be improved. PET is one of the most used plastic material, in packaging and bottle production industry. The amount of used PET has become a major environmental problem, as its molecules have a slow rate of natural decomposition ([Ioakeimidis et al., 2016](#)). The PET long biodegradation period (in a landfill it is close to 700 years) leads to different recycling processes, considered better ways to economically reduce PET waste ([Al-Azzawi, 2015](#)). Different types of industries are using recycled plastics, among them, the industry of building materials, which has a high capacity of embedding PET in different forms. Previous investigations revealed the influence of using PET as aggregate substitute in concrete, over the mechanical characteristics ([Chowdhury et al., 2013](#)), showing that PET concrete has lower compression strength, flexural rigidity and tensile strength than standard concrete. At the same time, using PET leads to lightweight concrete with better freeze thaw resistance, impact resistance and toughness. In this paper the authors investigate the influence over the acoustical properties of EPS and PET granules imbedded in concrete, compared to the properties of conventional concrete.

Vegetal and animal wastes are generally burned or used as land fillings (in conventional techniques) causing environmental pollution and soil contamination. Nevertheless, we must mention the efforts made to recover this biomass waste. There are numerous studies that relate to alternative technologies: microwave pyrolysis evaluating the vegetal waste potential to be converted into biochar with desirable properties for use in multi-applications ([Liew et al., 2018](#)), biomass gasification models ([Tavares et al., 2018](#)), anaerobic digestion mechanism of algae on biomethane production ([Saratale et al., 2018](#)). Sustainable and optimized waste management superstructure incorporating these available technological alternatives, as proposed by [Rizwan et al. \(2018\)](#), constitutes a great challenge for a cleaner and healthier life. The use of these types of wastes in the construction industry is being approached more and more in experimental studies due to their advantages related to

wide availability, increased renewability, reduced costs, sustainability ([Saxena et al., 2011](#)), thermal properties ([Sisman et al., 2011](#)) and acoustic properties. Natural fibers are, in general, good absorbers, so they can be used for noise barriers design. For example, a 40 mm layer of hemp fibers has about 57% absorption capacity (indicated by NRC); a 50 mm layer of kenaf fibers has 75% absorption performance; a 60 mm of sheep wool has about 50% absorption ability, in terms of NRC ([Asdrubali, 2007](#)). Their absorption performances are encouraging and new materials based on natural fibers can be realized, in order to increase the acoustic performances needed in environmental protection against the noise. Vegetal waste is also the corn cob. Corn cob is about 15% of total corn production ([Ashour et al., 2013](#)). Among the applications of corn cobs in the building materials industry are their use as a pore forming agent in light clay bricks, the realization of lightweight concrete blocks an enhanced freeze thaw durability ([Faustino et al., 2015](#)) or of lightweight concrete with a density of about 382 kg/m^3 ([Pinto et al., 2012](#)). Aggregates from sunflower stems have a very low bulk density of $105 \pm 2 \text{ kg/m}^3$ ([Nozahic et al., 2012](#)). Due to their low density and high porosity, the sunflower particles have a very good sound absorption coefficient of over 0.8 at 1000 Hz, similar to fiberglass, a conventional commercialized sound absorber ([Chabriac et al., 2016](#)). Sheep wool is especially used as thermal insulation material, but this material also presents good acoustic properties, and can be used as a sound absorber, noise barrier or vibration isolator ([Ballagh, 1996](#)). [Del Rey et al. \(2017\)](#) reports the acoustical characterization of sheep-wool. The authors manufactured several samples of sheep-wool and PET (used as a binder), demonstrating that sheep-wool is a good sound absorbing material at medium and high frequencies. For example, for a 50 mm layer of material consisting of 80% wool and 20% PET, the sound absorption coefficient at 1000 Hz is over 0.8.

Therefore, this study is focused on rating the acoustic performances, in terms of absorption, for composite materials made of concrete and the embedded wastes presented above. The authors experimentally investigated the absorption behavior of these composite materials using the standard 10534:1998, but modified after [Feng's proposal \(Feng, 2013\)](#). The end of the impedance tube is inserted in an anechoic room, the real absorption coefficient and transmission coefficient can be separated. This real measured coefficient has smaller values than the standard absorption coefficient measured in the tube method, with a rigid backing at the end, generally reported in the literature.

2. Experimental investigation

2.1. Materials

In order to establish the acoustic absorption coefficients in this study, concrete samples with different recycled materials were made: polystyrene granules, polyethylene terephthalate (PET) granules, treated corn cobs and sunflower stems, as well as small balls made of sheep wool.

All samples are based on the same components as those of the control mix (denoted as *mc*), a microconcrete having in its composition cement (430 kg/m^3), aggregate sort 0–4 mm (1070 kg/m^3) and aggregate sort 4–8 mm (655 kg/m^3). A superplasticizer based on polycarboxylate technology was used for reducing the water/cement ratio, and an accelerator based on rhodanid for speeding up the cement hydration process and water for a water/cement ratio of 0.43. In all waste concrete types the authors have replaced 50% of the aggregates volume with the corresponding waste, as described below.

The polystyrene microconcrete (denoted in this study as *mc-pol*) contains 50% of the volume of aggregates replaced with

polystyrene granules of different diameters ranging from 1 to 4 mm (Fig. 1a). For the PET concrete mixture, PET wastes were obtained by cutting bottles into small pieces, which in the tests ranged from 1 mm to 4 mm (Fig. 1b). Microconcrete with PET is denoted in this study as **mc-pet**.

In the case of corn cob concrete (denoted in the study as **mc-corn**) were added corn cob granules with variable diameter from 1 to 6 mm (Fig. 1c). In the case of sunflower concrete (denoted in this study as **mc-sun**) were added sunflower stalk shredded in granules with variable diameter from 1 to 5 mm and fibers with 5–25 mm length (Fig. 1d). Corn cob and sunflower granules were treated with a sodium silicate solution in order to reduce the water absorption capacity as in Helepciuc et al. (2017). After the treatment, the corn cob granules had a water absorption capacity of 127% and the sunflower granules had a 100% water absorption capacity.

In the concrete with wool granules (denoted in this study as **mc-wool**) were added balls with 6–16 mm in diameter made from sheep wool fibers glued with a plasticized vinyl polyacetate adhesive (Fig. 1e).

Table 1 presents the density of the reinforced concretes and their compressive strength. In order to determine the compressive strength of all types of microconcrete, the fresh concrete was poured in cubes with 100 mm sides. The samples were stored at 20 °C for 28 days until testing for determining compressive strength (SR EN 12390-3, 2009). The density of the hardened concrete was also determined according to SR EN 12390-7 (2009).

The tests were performed for three replicates of each mixture type, according to the standards. Therefore, the values shown below represent the mean values obtained from the three measurements for each of the six mixture types.

The authors do not track better results in compressive strength,

as we do not intend to use these materials as structural concrete, but as panels, with small dimensions. The 40 mm materials can be applied on a structural frame and the 80 mm materials can be stand-alone panels of limited heights, in order to assemble a sound absorption barrier.

2.2. Method

The method used for determining the acoustic absorption coefficient of these materials is based on the acoustic interferometer technique (Kundt tube), modified according to Feng (2013). The acoustic properties of the material are thus measured in condition of an anechoic termination of the tube. The idea was taken over and applied to some combined materials (with different backing plates) whose sound absorption coefficients were experimentally investigated (Bujoreanu et al., 2017) in an anechoic room. In this case, the anechoic chamber constitutes the final end of the impedance tube. In a standard configuration, the impedance tube is backed by a rigid plate (ISO standard 10534:1998), while in a modified one, the end of the tube is inserted in the anechoic room.

Hence, the meaning of the sound absorption coefficient suffers some changes.

In a standard impedance tube, the measured absorption coefficient, $\alpha_{standard}$, is the ratio of energy dissipated inside the material to the incident sound energy, taking into account only of the sound pressure reflection coefficient, r (Feng, 2013).

$$\alpha_{standard} = \frac{E_{absorbed}}{E_{incident}}; \quad \alpha_{standard} = 1 - |r|^2 \quad (1)$$

Usually, in the tube method, the absorption coefficient is

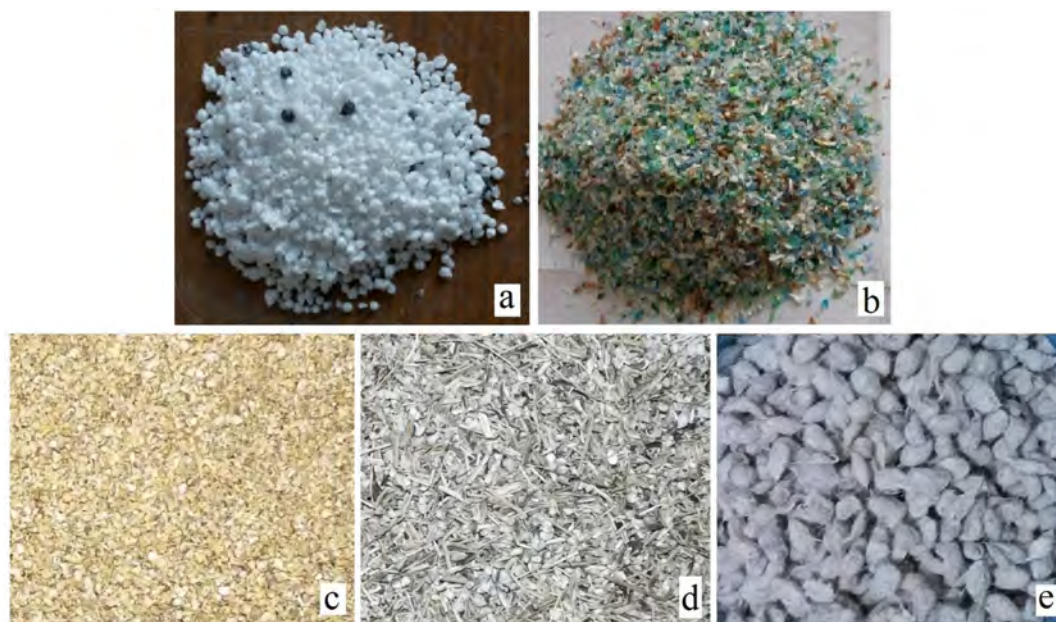


Fig. 1. Granules of recycled materials used in the concrete samples: a - polystyrene used in **mc-pol** concrete; b - PET used in **mc-pet** concrete; c - corn cob used in **mc-corn** concrete; d - shredded sunflower stalks used in **mc-sun** concrete; e - sheep wool balls used in **mc-wool** concrete.

Table 1

Hardened concrete density and compressive strength.

Concrete type	<i>mc</i>	<i>mc-pol</i>	<i>mc-pet</i>	<i>mc-corn</i>	<i>mc-sun</i>	<i>mc-wool</i>
Concrete density [kg/m ³]	2273	1810	2047	1775	1850	1930
Concrete compressive strength [MPa]	36.1	13.91	23.21	10.21	13.50	16.00

understood as one that is measured when a rigid backing at the end of the tube is mounted, therefore the transmission is avoided.

On the other hand, in the modified tube, with the end inserted in the anechoic room, there is a sound energy transmission through the sample, evidenced by the transmission coefficient, t .

In this case, the real sound absorption coefficient, α_{real} is estimated by Feng (2013).

$$\alpha_{real} = 1 - |r|^2 - |t|^2 \quad (2)$$

Using the Feng's procedure, the real absorption coefficient and transmission coefficient can be separated. When the sample is backed by a rigid plate the transmitted energy disappears and the sound absorption coefficient rating is the same as that for the standard impedance tube method defined by the corresponding ISO standards (Feng, 2013). Therefore, the values of the real absorption coefficient measured in the modified tube with anechoic end are lower than those obtained by standard measurements (with rigid support at the end of the tube).

In environmental protection against the noise, acoustic barriers are needed and their structures must have good absorption performances. It's about freely hanging materials, or frames supported and the real absorption coefficient approach is more realistic in these situations (eq. (2)). In other cases, when a material is directly mounted on a wall, the energy dissipated inside a material is close to the result from the standard tube configuration (eq. (1)). In this context, we consider of interest for practical situations to estimate the absorption behavior of some composite materials concrete based, used in urban environment, in terms of real absorption coefficient, as above described.

For each material, the weighted sound pressure level measured in decibels, dB(A), of the incident and reflected waves inside the impedance tube was measured according to ISO standard 10534-1:1998, with the methodology described by Bujoreanu et al. (2017). The 1/3 octave analysis was performed using the LabVIEW software. The method of A-weighted measurement, dB(A) combines octave-band sound data into a single-number descriptor. The letter "A" indicates that the sound has been filtered to reduce the strength of very low and very high frequency sounds, and corresponds to the human ear sensitivity. The human ear works like this and our intention is to assembly in sound absorption barriers these composite materials concrete based, in order to improve the acoustic comfort of urban people. Note that the human ear is most sensitive to sound in the frequency range 1000 Hz–4000 Hz than to sound at very low or high frequencies. This means that the noise at high or low frequencies will not be as annoying as it would be when its energy is concentrated in the middle frequencies (Vér and Beranek, 2006).

The measured upper frequency is limited to the frequencies of standing waves that can travel in the tube depending on the sound velocity and tube diameter (Vér and Beranek, 2006). The frequency of the sound waves is kept lower than the cut-off frequency to assure the generation of plane propagating waves in the tube. Our measurements could only cover frequencies up to 2000 Hz, as our tube diameter is 100 mm.

After data acquisition, octave analysis and processing, the authors have obtained results describing the relationship between the frequency and the real sound absorption coefficient of new materials made with waste.

The circular samples (Fig. 2), with a diameter of 100 mm are perfect fitting into the impedance tube. For the same type of composite material, 40 mm and 80 mm thickness samples were made in order to evaluate the dependence between the sound absorption coefficient and the material thickness. Each sample was tested three times and the mean value was calculated.

3. Experimental results and discussion

The experimental results are presented as graphs made for the comparison of the real sound absorption coefficients of each material with the *mc* control sample (Figs. 3–8).

Table 2 presents the real sound absorption coefficient for each material, for 1/3 octave band center frequency.

As can be seen from the graphs presented above (Figs. 3–8) and also from the results presented in Table 2, all concrete types with recycled materials analyzed have a better behavior regarding the sound energy absorption than conventional concrete sample, *mc*.

Figs. 9 and 10 describe the relationship between the frequency and the real sound absorption coefficient of the samples with thickness of 40 mm and 80 mm respectively. The variation of these curves is similar to some literature examples (Sukontasukkul, 2009). In our tests it is observed a drop in sound absorption around 500 Hz, which is also mentioned in other studies (Sukontasukkul, 2009; Wijnant et al., 2010). This is due to a possible excitation of the acoustic waves vibration mode, or to the fact that the sound level has a pressure minimum at that frequency.

Figs. 9 and 10 show the importance of the thickness of the material in the absorption of the sound waves, with a great difference between the absorption coefficients of the same type of material but with different thicknesses, especially at frequencies between 1000 and 2000 Hz. As one can see, we kept the range for the sound absorption coefficient from 0.00 to 0.55 in both of these graphics, so that it can easily be observed the difference between the real absorption coefficient for the 40 mm and 80 mm samples.

The results (Figs. 9 and 10) show that our composite materials have sound absorption values quite different for frequencies of



Fig. 2. Samples for measuring the sound absorption coefficient.

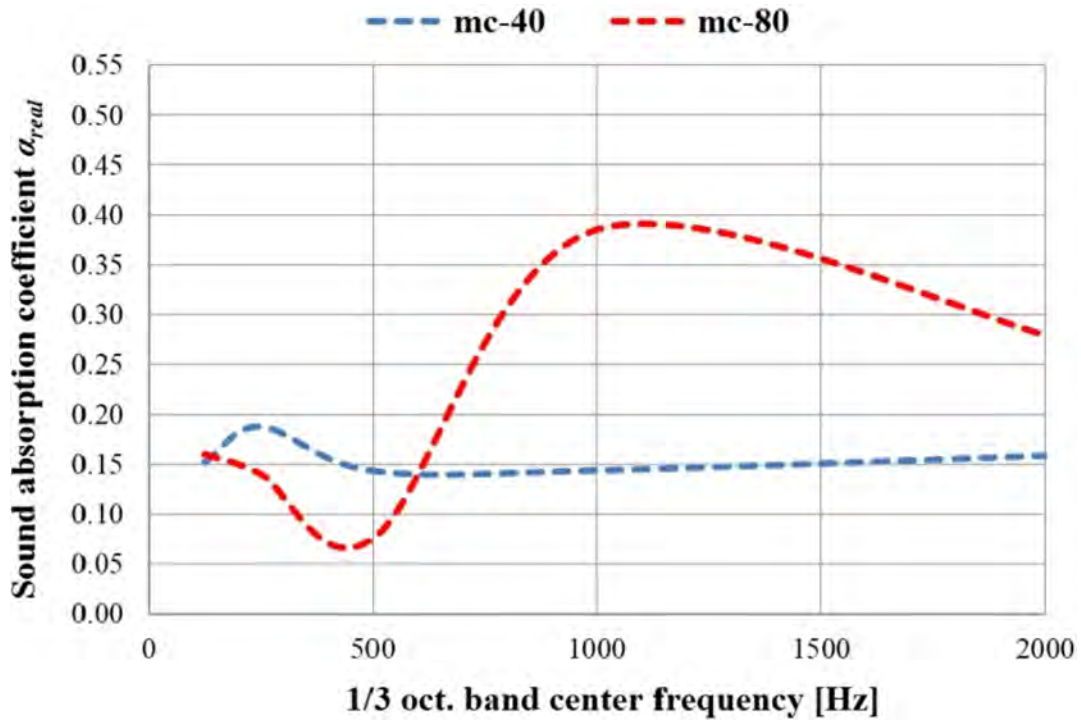


Fig. 3. The variation of the sound absorption coefficient for the control mixture (mc) for the 40 mm and 80 mm samples.

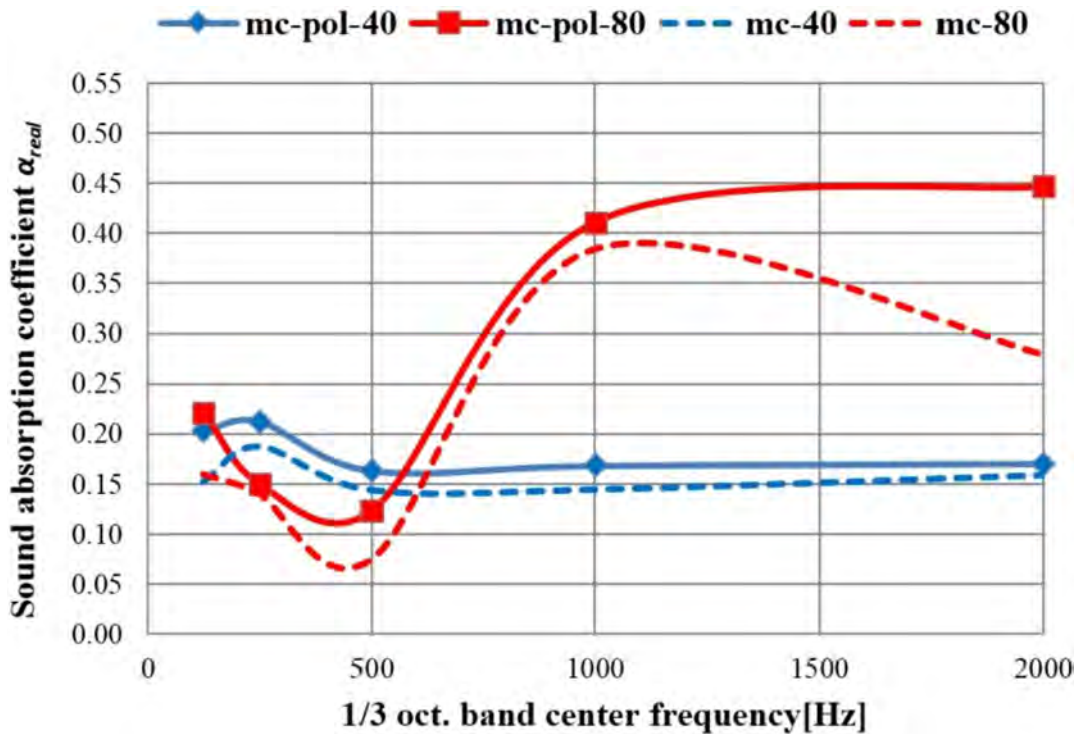


Fig. 4. The variation of the sound absorption coefficient for the microconcrete with polystyrene granules (mc-pol), samples of 40 mm and 80 mm, compared to the control sample mc.

interest. The environmental noise from road traffic, from industrial and civil entities, which influences, as pollutant, our comfort and health is a mixture of different disturbing sounds in the range of audible frequencies. The annoying frequencies cannot be separated

and the corresponding sounds cannot be entirely absorbed by a specific material. The same material can be more or less sound absorber at different frequencies.

Therefore, indicating the sound properties of materials using the

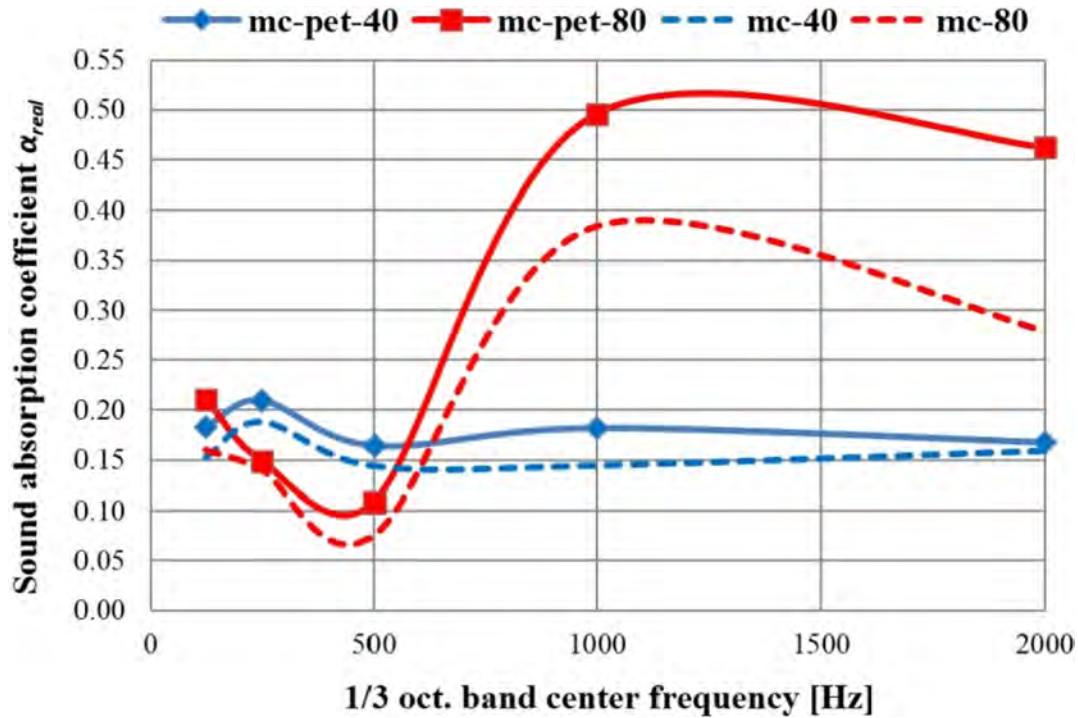


Fig. 5. The variation of the sound absorption coefficient for the microconcrete with PET granules (**mc-pet**), samples of 40 mm and 80 mm, compared to the control sample **mc**.

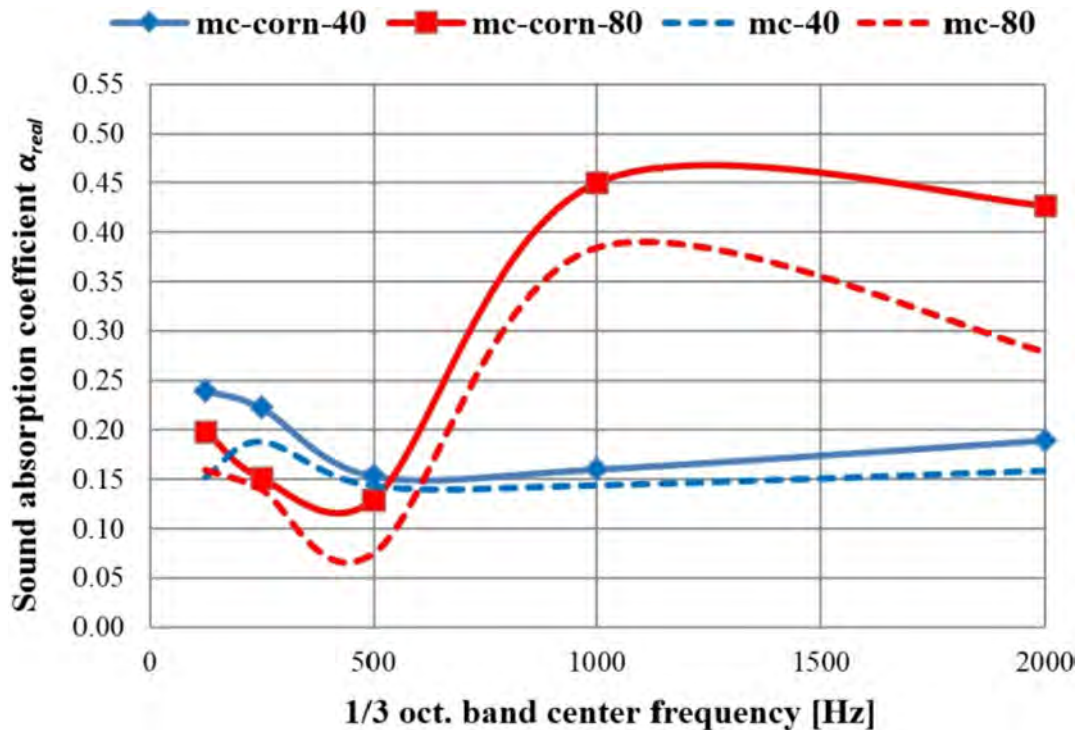


Fig. 6. The variation of the sound absorption coefficient for the microconcrete with corn cob granules (**mc-corn**), samples of 40 mm and 80 mm, compared to the control sample **mc**.

absorption coefficient is complex, involving several frequencies. To solve this problem, the ability of material to absorb sound is described using the noise reduction coefficient NRC, as a single descriptor (Vér and Beranek, 2006).

By calculating the noise reduction coefficient for frequency range 0–2000 Hz, for the tested materials, the following NRC are obtained, as given in Table 3. The noise reduction coefficient does not have high values, yet the tested materials have sound

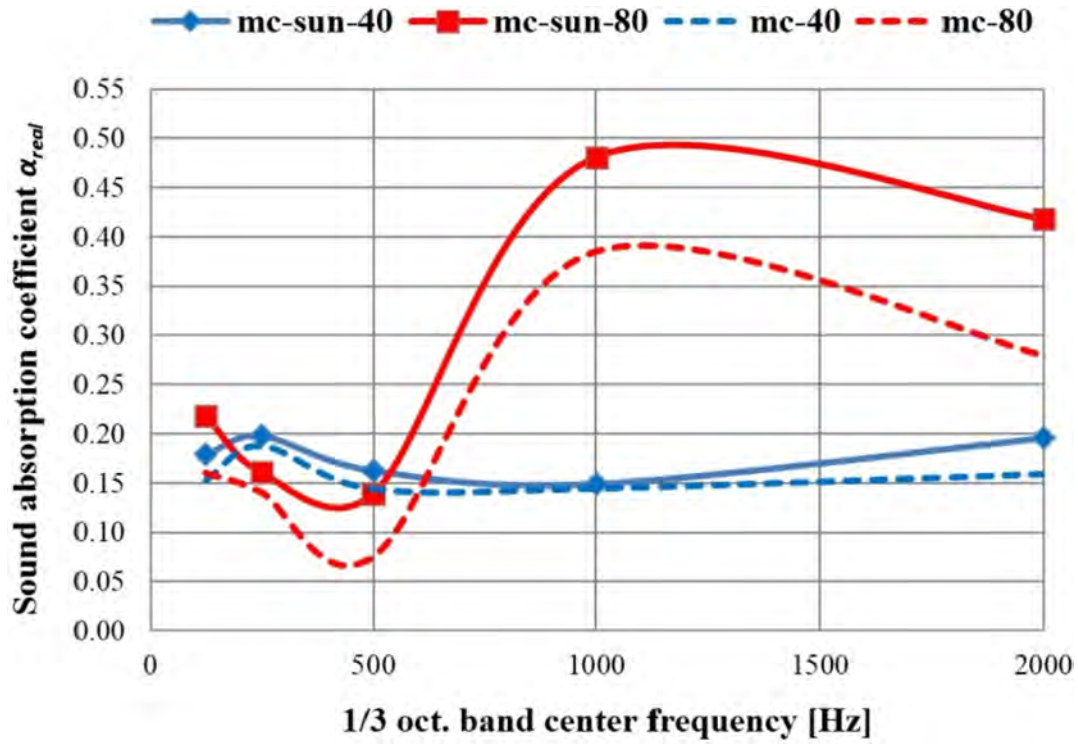


Fig. 7. The variation of the sound absorption coefficient for the microconcrete with sunflower stalk granules (**mc-sun**), samples of 40 mm and 80 mm, compared to the control sample **mc**.

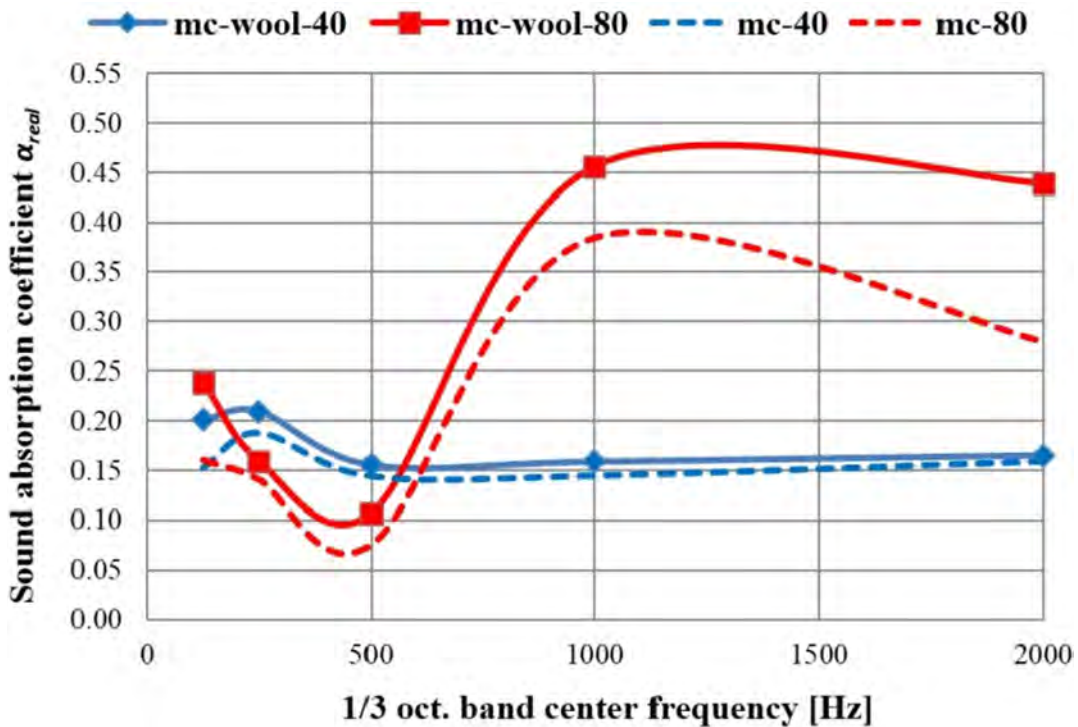


Fig. 8. The variation of the sound absorption coefficient for the microconcrete with sheep wool balls (**mc-wool**), samples of 40 mm and 80 mm, compared to the control sample **mc**.

absorption characteristics much better than common concrete. If we compare the NRC of the 40 mm samples with the NRC of the 80 mm samples, we will observe that doubling the thickness of the

material leads to a substantial increase in sound absorption (Table 3 and Fig. 11).

Among the 40 mm concrete samples with waste substitute, the

Table 2
Sound absorption coefficient for each material.

Freq. [Hz]	Sound absorption coefficient α_{real}											
	<i>mc</i>		<i>mc-pol</i>		<i>mc-pet</i>		<i>mc-corn</i>		<i>mc-sun</i>		<i>mc-wool</i>	
	40 mm	80 mm	40 mm	80 mm	40 mm	80 mm	40 mm	80 mm	40 mm	80 mm	40 mm	80 mm
125	0.152	0.160	0.203	0.221	0.183	0.210	0.240	0.199	0.179	0.218	0.201	0.238
250	0.188	0.140	0.213	0.150	0.210	0.149	0.223	0.151	0.198	0.161	0.210	0.159
500	0.144	0.075	0.163	0.123	0.164	0.108	0.153	0.129	0.162	0.139	0.155	0.107
1000	0.144	0.385	0.168	0.411	0.182	0.496	0.160	0.450	0.149	0.481	0.159	0.456
2000	0.159	0.279	0.170	0.447	0.167	0.462	0.190	0.427	0.196	0.418	0.165	0.439

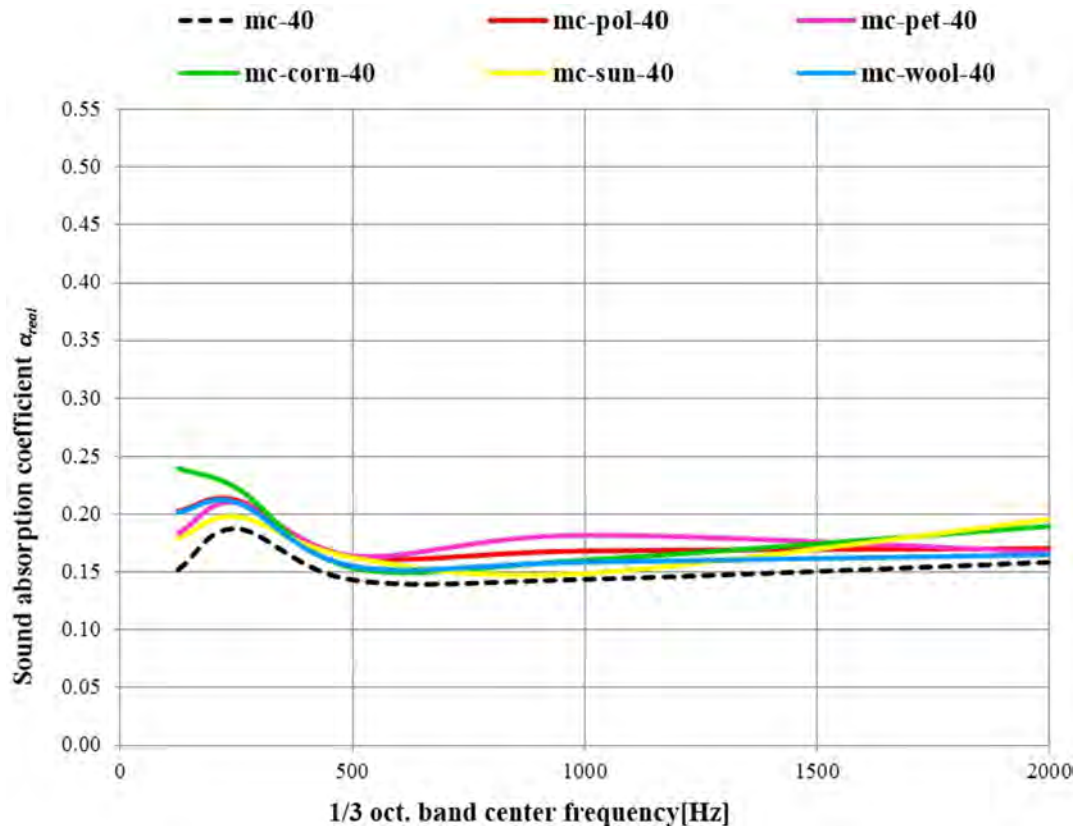


Fig. 9. Variation of sound absorption coefficients for the 40 mm samples.

one with corn cob granules had the highest values, the real sound absorption coefficient exceeding the control sample value by 22% (Fig. 12).

Among the 80 mm concrete samples, the one with PET granules had the highest values, the sound absorption coefficient exceeding by 37% the value of the control sample (Fig. 13).

There is thus a dependence between the density of the material, the thickness of the sample and the measured sound absorption coefficients, as shown in Fig. 14.

Thus, for samples with a thickness of 40 mm, the best absorption behavior, in terms of NRC, was recorded by the materials with the lowest density (concrete with corn cob, denoted *mc-corn*). This composite is less dense due to the corn cob which is a pore forming agent. A more open structure allows more energy loss of the sound incident waves, due to the friction loss inside the porous material and generally has a better sound absorption (Amares et al., 2017; Arenas and Crocker, 2010). At high frequencies, above 2000 Hz,

denser structures have better absorption abilities (Seddeq, 2009).

On the other hand, in the 80 mm thickness samples, the higher the density of the material, the higher the absorption behavior, in terms of NRC (PET concrete, denoted *mc-pet*). The global absorption behavior is thickness dominated. The material thickness is directly related to the frequency range, being relevant up to 2000 Hz and less significant for high frequencies over 2000 Hz (Amares et al., 2017; Seddeq, 2009). Thickness increasing provides better absorption of the higher sound wavelength which characterizes low and medium frequencies (up to 2000 Hz), according to the physics laws. The increase of sound absorption value in the middle and higher frequency range as the density of the sample increased is reported in the literature (Shahani et al., 2014; Amares et al., 2017).

The use of natural fibers in our materials composition has similar results, in terms of NRC, with the other tested materials. In a future study for the wool-containing materials, we intend to obtain a better sound absorption behavior, by decreasing the fibers

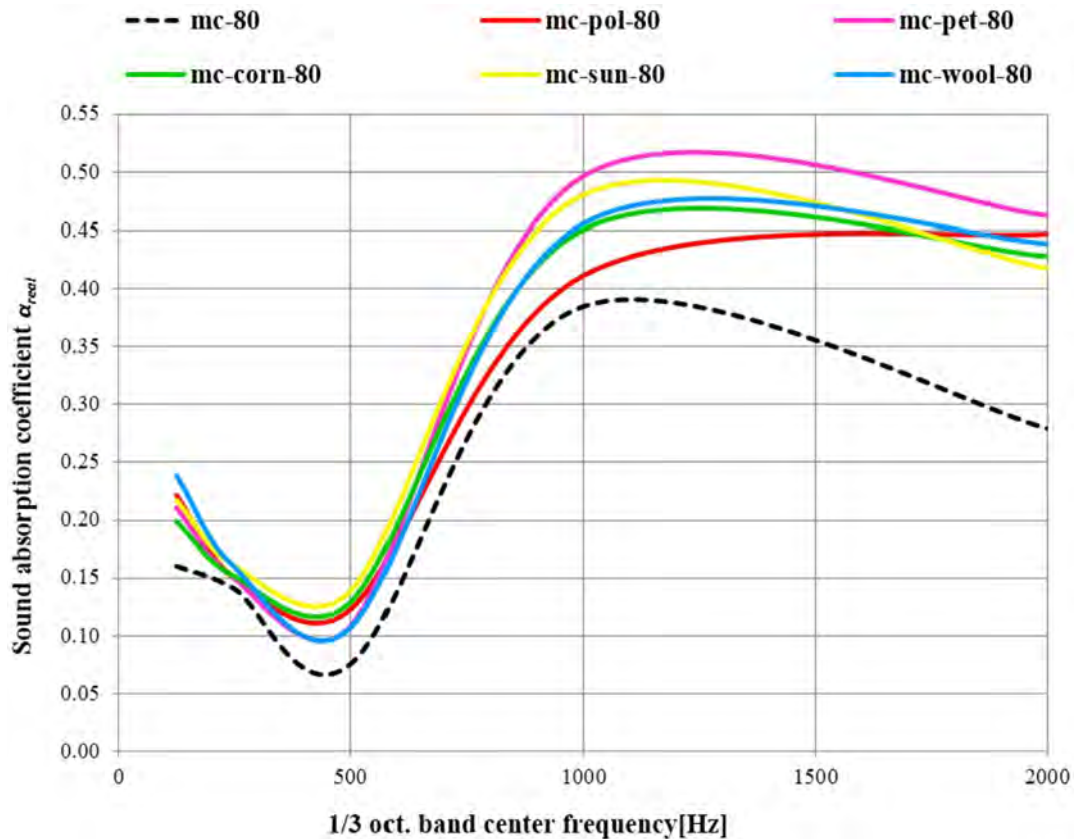


Fig. 10. Variation of sound absorption coefficients for the 80 mm samples.

Table 3

Noise reduction coefficients for each material.

thickness	mc	mc-pol	mc-pet	mc-corn	mc-sun	mc-wool
40 mm	0.157	0.184	0.181	0.193	0.177	0.178
80 mm	0.208	0.270	0.285	0.271	0.283	0.280
$\frac{NRC(80mm)}{NRC(40mm)}\%$	132%	147%	157%	140%	160%	157%

diameter. The fiber diameter is an important material parameter and it is directly related to the sound-absorbing characteristics (Arenas and Crocker, 2010).

Our results are promising for the studied composite materials, in the frequency range up to 2000 Hz. However, the literature (Wang et al., 2016) states that are needed different sound control strategies for different frequency components of road traffic noise and the absorption behavior at low frequency below 500 Hz should be more in-depth investigated.

Basically, the acoustical aspects of new materials is a complex task that must combine many parameters dependent upon frequency, composition, thickness, surface finish, method of mounting. For the best results in materials absorption performances, experimental investigations are needed.

4. Conclusions

In the paper the authors have analyzed the real sound absorption coefficients of five different sustainable materials, based on conventional concrete with waste additions, using two different thicknesses for the samples: 40 mm and 80 mm. The use of the Feng's procedure, with the impedance tube anechoic ending, allows

to separate the real absorption coefficient and transmission coefficient. The measured real absorption coefficients have smaller values than the standard ones, according to their conventional meaning. For all types of waste concrete analyzed in this paper, the sound absorption coefficients were considerably higher than the values recorded by conventional concrete. The measurements revealed that the best material within the 40 mm samples was the corn-cob concrete, with a noise reduction coefficient of 0.193. For the 80 mm samples, the PET concrete had the best sound absorption behavior, having a NRC of 0.285. By doubling the thickness of the material samples, the NRC increases with a substantial percentage of about 150%. It can be concluded that these types of concrete, with various substitutions of natural aggregates, can be successfully used in acoustic barriers. Such barriers made of concrete panels with various materials considered waste can have a positive impact on the noise level experienced in the affected area. The density, as well as the porosity of the composites are influence factors on sound absorption and will be a matter of future interest in our research on sound barriers. Further, we intend to find a way to treat the surface of these panels in a manner that they do not generate visual discomfort, avoiding the urban monotony.

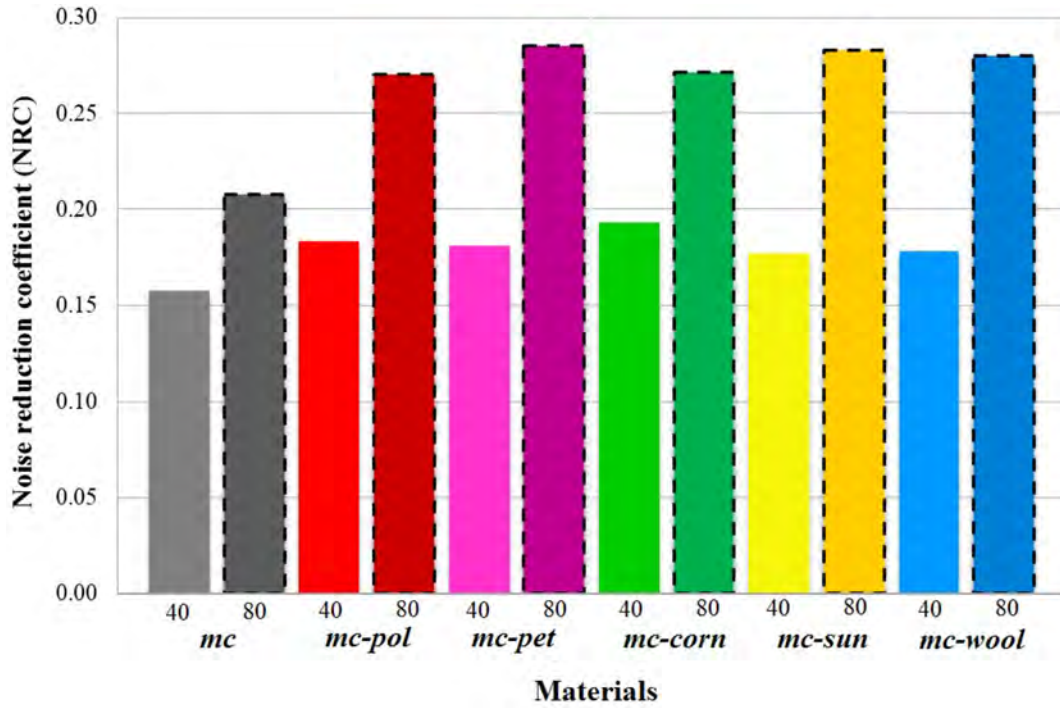


Fig. 11. Variation of NRC for 40 mm and 80 mm thickness of each material.

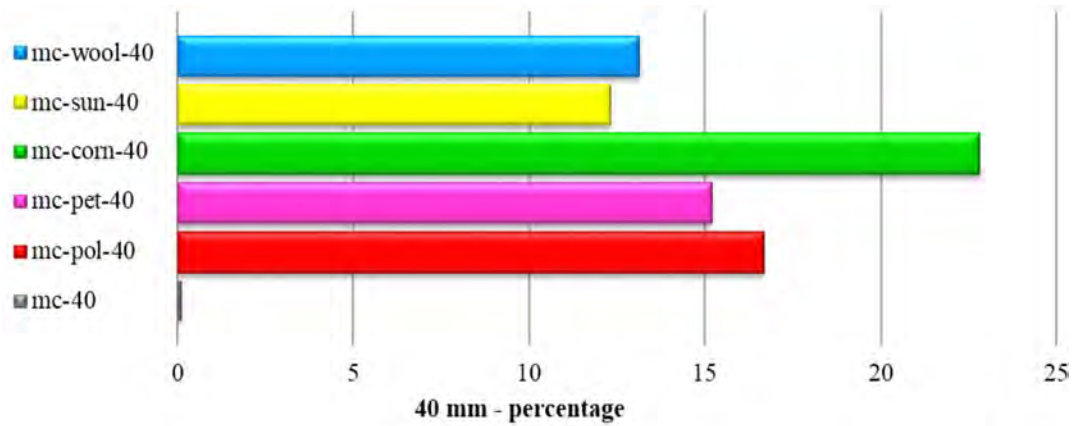


Fig. 12. Exceedings of the sound absorption coefficients for the 40 mm samples in percentage relative to the control sample coefficient.

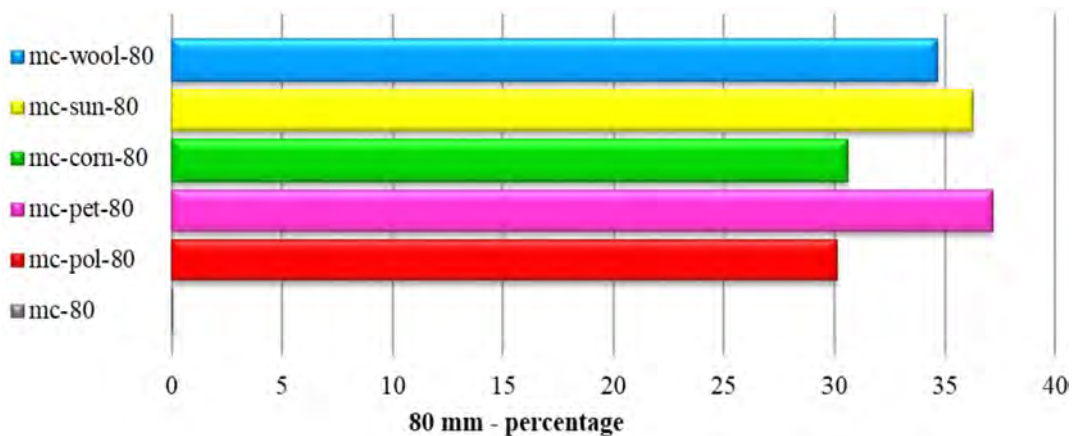


Fig. 13. Exceedings of the sound absorption coefficients for the 80 mm samples in percentage relative to the control sample coefficient.

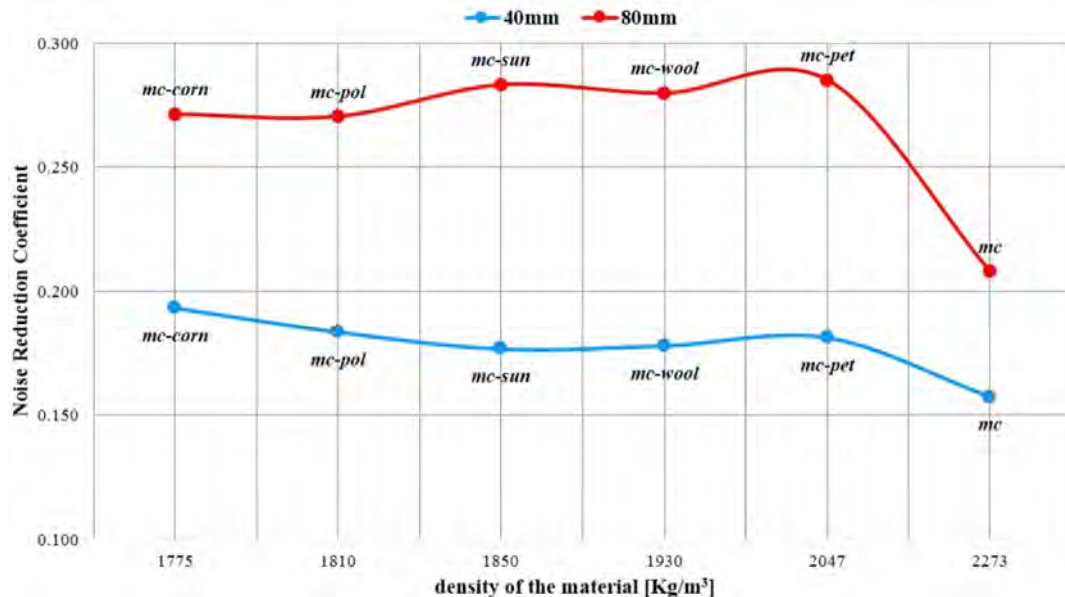


Fig. 14. Relationship between NRC and the density of the materials.

References

- Al-Azzawi, F., 2015. Degradation Studies on Recycled Polyethylene Terephthalate. Doctoral thesis. London Metropolitan University. <http://repository.londonmet.ac.uk/id/eprint/917>.
- Amares, S., Sujatmika, E., Hong, T.W., Durairaj, R., Hamid, H.S.H.B., 2017. A review: characteristics of noise absorption material. *J. Phys.: Conf. Series* 908, 012005.
- Arenas, J.P., Crocker, M.J., 2010. Recent trends in porous sound-absorbing materials. *Sound Vib.* 44, 12–17.
- Asdrubali, F., 2007. Green and sustainable materials for noise control in buildings. In: 19th Int. Congr. On Acoustics. PACS, Madrid, 2–7 September 2007. http://www.sea-acustica.es/WEB_ICA_07/fchrs/papers/rba-01-008.pdf, 43.55.Ev.
- Ashour, A., Amer, M., Marzouk, A., Shimizu, K., Kondo, R., El-Sharkawy, S., 2013. Corncobs as a potential source of functional chemicals. *Molecules* 18, 13823–13830.
- Ballagh, K.O., 1996. Acoustical properties of wool. *Appl. Acoust.* 48 (2), 101–120.
- Bujoreanu, C., Nedeff, F., Benchea, M., Agop, M., 2017. Experimental and theoretical considerations on sound absorption performance of waste materials including the effect of backing plates. *Appl. Acoust.* 119, 88–93.
- Chabriac, P.A., Gourdon, E., Gle, P., Fabbri, A., Lenorman, H., 2016. Agricultural by-products for building insulation: acoustical characterization and modeling to predict micro-structural parameters. *Construct. Build. Mater.* 112, 158–167.
- Chen, B., Liu, J., Chen, L.Z., 2010. Experimental study of lightweight expanded polystyrene aggregate concrete containing silica fume and polypropylene fibers. *J. Shanghai Jiao Tong Univ. (Sci.)* 15 (2), 129–137.
- Chowdhury, S., Maniar, A.T., Suganya, O., 2013. Polyethylene terephthalate (PET) waste as building solution. *Int. J. Chem. Environ. Biol. Sci.* 1 (2), 2320–4087 (online).
- Cook, D.J., 1983. In: *Expanded Polystyrene Concrete*. New Concrete Materials: Concrete Technology and Design, vol. 1. Surrey University press, London, pp. 41–69.
- Del Rey, R., Uris, A., Alba, J., Candelas, P., 2017. Characterization of sheep wool as a sustainable material for acoustic applications. *Materials* 10 (11), 1277. <http://doi.org/10.3390/ma10111277>. <https://www.ncbi.nlm.nih.gov/pmc/articles/PMC5706224/>.
- Faustino, J., Silva, E., Pinto, J., Soares, E., Cunha, V.M.C.F., Soares, S., 2015. Lightweight concrete masonry units based on processed granulate of corn cob as aggregate. *Mater. Construcción* 65 (318), e055. <https://doi.org/10.3989/mc.2015.04514>.
- Felix, J.S., Domeco, C., Nerin, C., 2013. Characterization of wood plastic composites made from landfill-derived plastic and sawdust: volatile compounds and olfactometric analysis. *Waste Manag.* 33, 645–655.
- Feng, L., 2013. Modified impedance tube measurements and energy dissipation inside absorptive materials. *Appl. Acoust.* 74, 1480–1485.
- Ferrandiz-Mas, V., Garcia-Alcoel, E., 2012. Physical and mechanical characterization of Portland cement mortars made with expanded polystyrene particles addition (EPS). *Mater. Construcción* 62, 547–566.
- Ghizdavet, Z., Stefan, B.M., Nastac, D., Vasile, O., Bratu, M., 2016. Sound absorbing materials made by embedding crumb rubber waste in a concrete matrix. *Construct. Build. Mater.* 124, 755–763.
- Helepciuc, C.M., Bărbuță, M., Ciocan, V., Serbanoiu, A.A., 2017. Characterization of a lightweight concrete with corn cob aggregates. In: *Multidisciplinary Scientific Geoconference SGEM 2017, Conf. Proc.*, vol. 17, pp. 49–56.
- Ioakeimidis, C., Fotopoulou, K.N., Karapanagioti, H.K., Geraga, M., Zeri, C., Papanthassiou, E., Galgani, F., Papatheodorou, G., 2016. The degradation potential of PET bottles in the marine environment: an ATR-FTIR based approach. *Sci. Rep.* 6 (23501). <https://www.nature.com/articles/srep23501>.
- ISO 10534, 1998. Acoustics - Determination of Sound Absorption Coefficient and Impedance in Impedance Tubes: Part 1: Method Using Standing Wave Ratio, Part 2: Transfer-function Method.
- Kim, H.K., Lee, H.K., 2010. Influence of cement flow and aggregate type on the mechanical and acoustic characteristics of porous concrete. *Appl. Acoust.* 71, 607–615.
- Liew, R.K., Nam, W.L., Chong, M.Y., Phang, X.Y., Su, M.H., Yek, P.N.Y., Ma, N.L., Cheng, C.K., Chong, C.T., Lam, S.S., 2018. Oil palm waste: an abundant and promising feedstock for microwave pyrolysis conversion into good quality biochar with potential multi-applications. *Process. Safe Environ.* 115, 57–69.
- Nozahic, V., Amziane, S., Torrent, G., Saidi, K., De Baynast, H., 2012. Design of green concrete made of plant-derived aggregates and a pumice-lime binder. *Cement Concr. Compos.* 34, 231–241.
- Oltean-Dumbrava, C., Miah, A., 2016. Assessment and relative sustainability of common types of roadside noise barriers. *J. Clean. Prod.* 135, 919–931.
- Pinto, J., Vieira, B., Pereira, H., Jacinto, C., Vilela, P., Paiva, A., Pereira, S., Cunha, V.M.C.F., Varum, H., 2012. Corn cob lightweight concrete for non-structural applications. *Construct. Build. Mater.* 34, 346–351.
- Rizwan, M., Saif, Y., Almansoori, A., Elkamel, A., 2018. Optimal processing route for the utilization and conversion of municipal solid waste into energy and valuable products. *J. Clean. Prod.* 174, 857–867.
- Saratale, R.G., Kumar, G., Banu, R., Xia, A., Periyasamy, S., Saratale, G.D., 2018. A critical review on anaerobic digestion of microalgae and macroalgae and co-digestion of biomass for enhanced methane generation. *Bioresour. Technol.* 262, 319–332.
- Saxena, M., Pappu, A., Sharma, A., Haque, R., Wankhede, S., 2011. Composite materials from natural resources: recent trends and future potentials. *Adv. Compos. Mater. Pavla Tesinova IntechOpen*. <https://doi.org/10.5772/18264>.
- Seddeq, H.S., 2009. Factors influencing acoustic performance of sound absorptive materials. *Aust. J. Basic & Appl. Sci.* 3 (4), 4610–4617.
- Shahani, F., Soltani, P., Zarrebini, M., 2014. The analysis of acoustic characteristics and sound absorption coefficient of needle punched nonwoven fabrics. *J. Eng. Fiber. Fabr.* 9 (2), 84–92.
- Sikora, J., Turkiewicz, J., 2010. Sound absorption coefficients of granular materials. *Mech. Contr.* 29 (3), 149–157.
- Sisman, C.B., Gezer, E., Kocaman, I., 2011. Effects of organic waste (rice husk) on the concrete properties for farm buildings. *Bulg. J. Agric. Sci.* 17 (1), 40–48.
- SR EN 12390–12393, 2009. Testing Hardened Concrete. Part 3: Compressive Strength of Test Specimens. Romanian Standard Association.
- SR EN 12390-7, 2009. Testing Hardened Concrete. Density of Hardened Concrete. Romanian Standard Association.
- Sukontasukkul, P., 2009. Use of crumb rubber to improve thermal and sound properties of pre-cast concrete panel. *Construct. Build. Mater.* 23 (2), 1084–1092.
- Tavares, R., Ramos, A., Rouboa, A., 2018. Microplastics thermal treatment by polyethylene terephthalate-biomass gasification. *Energy Convers. Manag.* 162, 118–131.

Vér, I.L., Beranek, L.L., 2006. *Noise and Vibrations Control Engineering: Principles and Applications*. John Wiley&Sons, Inc., Hoboken, New Jersey.

Wang, V.S., Lo, E.W., Liang, C.H., Chao, K.P., Bao, B.Y., Chang, T.Y., 2016. Temporal and spatial variations in road traffic noise for different frequency components in

metropolitan Taichung, Taiwan. *Environ. Pollut.* 219, 174–181.

Wijnant, Y.H., Keipers, E.R., de Boer, IrA., 2010. Development and application of a new method for the in-situ measurement of sound absorption. *Proc. Isma* 109–122.

Surface roughness influence on active surfaces geometry and modified rating life of rolling contacts

M Benchea¹ and S Crețu¹

¹Mechanical Engineering, Mechatronics and Robotics Department, “Gheorghe Asachi” Technical University of Iași, Iași, Romania

E-mail: marcelin.benchea@tuiasi.ro

Abstract. The active surfaces topography of bodies in rolling contact can be obtained by different manufacturing technology. The scope of this paper is to evidence the influence of the initial surface roughness on running-in process, working surface geometry and durability of rolling contacts. The paper presents a numerical study applied on a toroidal roller bearing where the modified rating lives have been evaluated with the methodologies mentioned by ISO 16281.

1. Introduction

The topography of the active surfaces in rolling contact depends on the surface manufacturing process technology. In the field of engineering the exact degree of roughness can be of considerable importance, affecting the function of a component or its cost [1,2,3].

The roughness of the surfaces that interacts has an important role on its tribological behaviour. The solutions of the models used in order to describe it [4,5] require the input of a three-dimensional rough profile. Since the experimental acquisition of such profiles does not allow a sufficiently large sample of profiles to be used, an essential requirement for any numerical algorithm is to generate arbitrarily rough surfaces with the same or similar proprieties of the real surfaces [6,7].

When two engineering surfaces are loaded for the first time changes in the topography of both surfaces generally occur. These changes appear between start-up and steady state and are associated with running-in process [8,9].

An analysis model was developed to model the nonlinear strain rate dependent deformation of materials stressed in elastic-plastic domain [10,11]. The model is developed in the frame of incremental theory of plasticity using the von Mises yield criterion and Prandtl-Reuss equations. Considering the isotropic and non-linear kinematic hardening laws of Lemaitre-Chaboche [12,13] the model accounts for the cyclic hardening phenomena.

The nano-asperities of contact surfaces generate high pressure peaks in pressure distributions that can severely diminish the modified rating life as is defined by [14].

2. Theory

2.1. Elastic-plastic model

The elastic-plastic model developed to evaluate the plastic deformation of the surfaces considers the material cyclic hardening characteristic that is described by a combined isotropic and nonlinear kinematic hardening laws [12,13].



The yield surface is defined by the von Mises yield criterion:

$$F = f(\sigma - \alpha) - \sigma_Y^0 = 0 \quad (1)$$

where $f(\sigma - \alpha)$ is the equivalent von Mises stress and σ_Y^0 is the yielding stress.

The non-linear kinematic hardening component describes the ratchetting effect by expressing the translation of the yield surface in the stress space through the back-stress α .

The isotropic hardening component of the model defines the yielding stress as a function of the equivalent plastic strain and is given by the relation:

$$\sigma_Y^0 = \sigma_{Y0} + Q_\infty \cdot \left(1 - e^{-b_\infty \cdot \bar{\varepsilon}^p}\right) \quad (2)$$

where Q_∞ is the limiting change in the yield surface size on the deviatoric plane and b_∞ describes how rapid the limit size is reached [15].

According to the energetic theory of fracture, the von Mises stress is an equivalent uniaxial traction stress [13]. For a 3D contact loading in each point of the stressed volume the equation of von Mises stress amplitude includes all 6 components of the stress tensor. For this consideration, when the yield limit is overcome, it can be used the pseudo-plastic Ramberg-Osgood's equation in the combined hardening laws, equation that gives the correspondence between the intensity of the stress tensor and the intensity of the strain tensor:

$$\bar{\varepsilon}_e = \frac{\bar{\sigma}_e}{E} + \left(\frac{\bar{\sigma}_e}{B}\right)^N \quad (3)$$

where B is the coefficient of plastic resistance and N is the hardening exponent [10,11].

The plastic deformation of the surfaces is given by the plastic strains accumulated in the sub-surface layer:

$$u^p(x, y) = \int_0^z \varepsilon^p(x, y, z) \cdot dz \quad (4)$$

2.2. Modified rating life

The classic computation of the rolling bearings basic rating life considers only the equivalent load on the bearing P , dynamic capacity load C and an exponent p depending of the rolling element:

$$L_{10} = \left[\frac{C}{P}\right]^p \quad (5)$$

where $p = 3$ for ball bearings and $p = 10/3$ for roller bearings [16].

To take into account the peaks of the pressure distributions generated by the presence of the nano-asperities on the surface, was developed a method to compute the basic rating life with methodology given by the standard ISO 16281 [14].

In the first instance, for the roller bearings, to evaluate the rating life is needed to determine the elastic deflection of each loaded roller j that depends on the radial load and internal radial clearance of the bearing:

$$\delta_j = \delta_r \cdot \cos \varphi_j - \frac{s}{2} \quad (6)$$

In the second instance, to consider de load on every loaded roller is used the lamina model as is described in [14] and the roller is divided into n_s identical laminae.

The load $q_{j,k}$ on lamina k of the roller j is:

$$q_{j,k} = c_s \cdot \delta_{j,k}^{10/9} \quad (7)$$

with the spring constant c_s :

$$c_s = \frac{35948 \cdot L_w^{8/9}}{n_s} \quad (8)$$

where L_w is the roller length and n_s is the laminae number [14].

In the third instance, the basic rating life L_{10r} of the roller bearings is calculated with:

$$L_{10r} = \left\{ \sum_{k=1}^{n_s} \left[\left(\frac{q_{kci}}{q_{kei}} \right)^{-9/2} + \left(\frac{q_{kce}}{q_{kee}} \right)^{-9/2} \right] \right\}^{-8/9} \quad (9)$$

where: q_{kci} - basic dynamic load rating of a bearing lamina of the inner ring,

q_{kce} - basic dynamic load rating of a bearing lamina of the outer ring,

q_{kei} - dynamic equivalent load on a lamina k of a rotating inner ring,

q_{kee} - dynamic equivalent load on a lamina k of a stationary outer ring.

According to standard [14], the dynamic equivalent loads on each lamina of the inner/outer ring q_{kei} and q_{kee} are computed as a function of the stress riser coefficients evaluated for each lamina of each roller. The stress risers are calculated considering the pressure distribution on the corresponding lamina.

In the last instance, the modified rating life L_{10mr} of the roller bearings is given by:

$$L_{10mr} = \left(\sum_{k=1}^{n_s} \left\{ a_{ISO} \left(\frac{\eta_c \cdot P_u}{P_{ks}}, \kappa \right) \right\}^{-9/8} \cdot \left[\left(\frac{q_{kci}}{q_{kei}} \right)^{-9/2} + \left(\frac{q_{kce}}{q_{kee}} \right)^{-9/2} \right] \right)^{-8/9} \quad (10)$$

where the life modification factor a_{ISO} is calculated for each bearing lamina k using its dynamic equivalent load P_{ks} :

$$P_{ks} = 0.323 \cdot Z \cdot n_s \cdot \cos \alpha \cdot \left[\frac{q_{kei}^{9/2} + (1.038 \cdot q_{kci}/q_{kce})^{9/2} \cdot q_{kee}^{9/2}}{1 + (1.038 \cdot q_{kci}/q_{kce})^{9/2}} \right]^{2/9} \quad (11)$$

In facts, the life modification factor a_{ISO} is a function that depends on the lubrication factor κ , oil contamination factor η_c and fatigue load limit P_u for the given application [16].

3. Results and Discussion

A toroidal roller bearing - CARB C2318, has been selected for the numerical case study. The main geometrical data are as follows: inner ring diameter $d_{ci} = 115 \text{ mm}$, outer ring diameter $d_{ce} = 165 \text{ mm}$, roller diameter $d_w = 25 \text{ mm}$, roller length $L_w = 54 \text{ mm}$, number of rollers $Z = 14$. The catalogue data [17]: dynamic capacity load $C = 610 \text{ kN}$ and fatigue load limit $P_u = 73.5 \text{ kN}$.

For numerical case study of the running-in process a medium radial loading $F_R = 0.185 \cdot C = 112.5 \text{ kN}$ and three magnitudes of the surface roughness parameters was used: a fine roughness with $R_{qw1} = 40 \text{ nm}$ for roller surface and $R_{qi1} = 70 \text{ nm}$ for inner ring raceway surface, similar to the surface roughness values measured with Taylor Hobson profilometer, a medium roughness with $R_{qw2} = 80 \text{ nm}$ and $R_{qi2} = 140 \text{ nm}$ and a grossly roughness with $R_{qw3} = 120 \text{ nm}$ and $R_{qi3} = 210 \text{ nm}$.

To consider the material behaviour, in the elastic-plastic model was used the following parameters of the roller bearing steel: the Young modulus $E = 209 \text{ GPa}$, the Poisson coefficient $\nu = 0.29$, the yielding stress $\sigma_{Y0} = 1650 \text{ MPa}$, the limiting change in the yield surface size on the deviatoric plane $Q_{\infty} = -100 \text{ MPa}$ and $b_{\infty} = 120$ which describes how rapid the limit size is reached [15], the coefficient of plastic resistance $B = 4320 \text{ MPa}$ and the hardening exponent $N = 12.6$ [10,11].

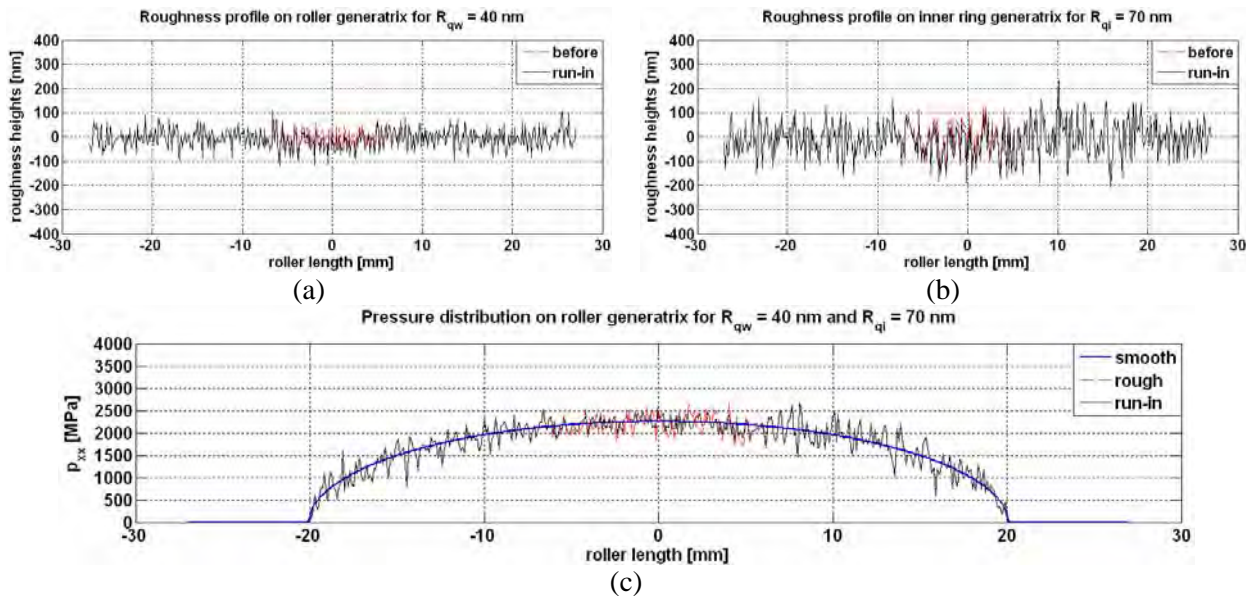


Figure 1. Numerical results for highest loaded roller-inner ring contact ($R_{qw1} = 40 \text{ nm}$, $R_{qi1} = 70 \text{ nm}$): (a) roughness profile on roller (before and after run-in), (b) roughness profile on inner ring (before and after run-in) and (c) pressure distribution.

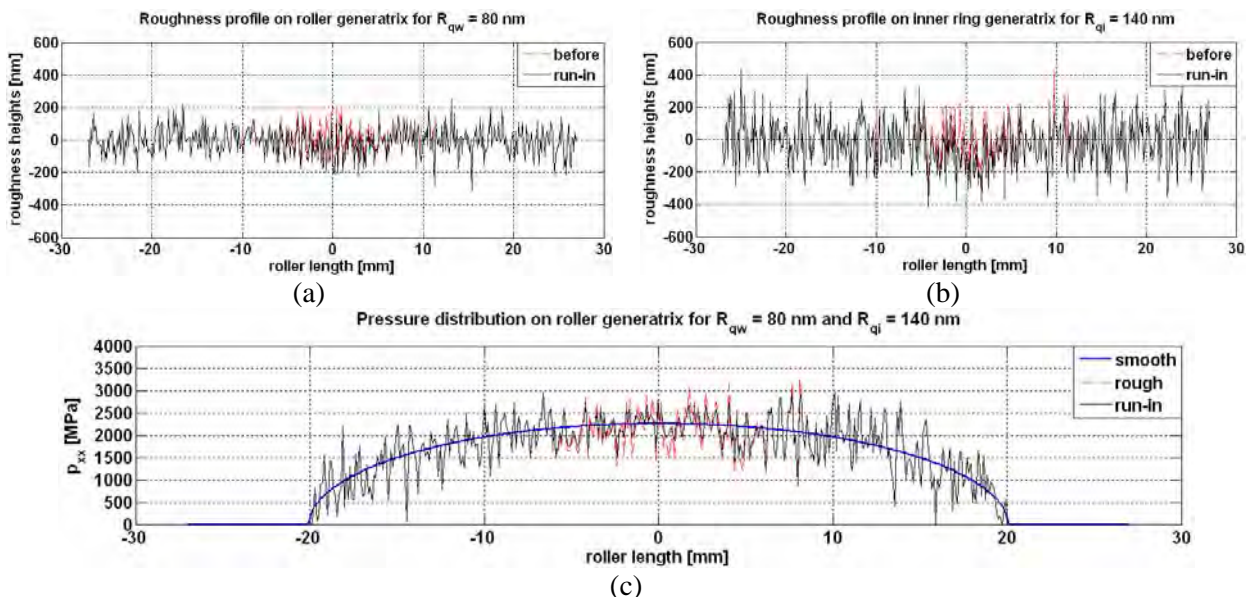


Figure 2. Numerical results for highest loaded roller-inner ring contact ($R_{qw1} = 80 \text{ nm}$, $R_{qi1} = 140 \text{ nm}$): (a) roughness profile on roller (before and after run-in), (b) roughness profile on inner ring (before and after run-in) and (c) pressure distribution.

In figures 1(a),(b), 2(a),(b) and 3(a),(b) are presented the 2D roller and inner ring roughness profiles before and after 300 running cycles. It can be observed that the running-in process is more pronounced for the inner ring and the roughness heights are plastic deformed in the middle contact

area for 10 mm in length for $R_{qi1} = 70\text{ nm}$, for 20 mm in length for $R_{qi2} = 140\text{ nm}$ and for 40 mm in length for $R_{qi3} = 210\text{ nm}$. The plastic deformations of the roughness peaks are higher as the roughness is coarser.

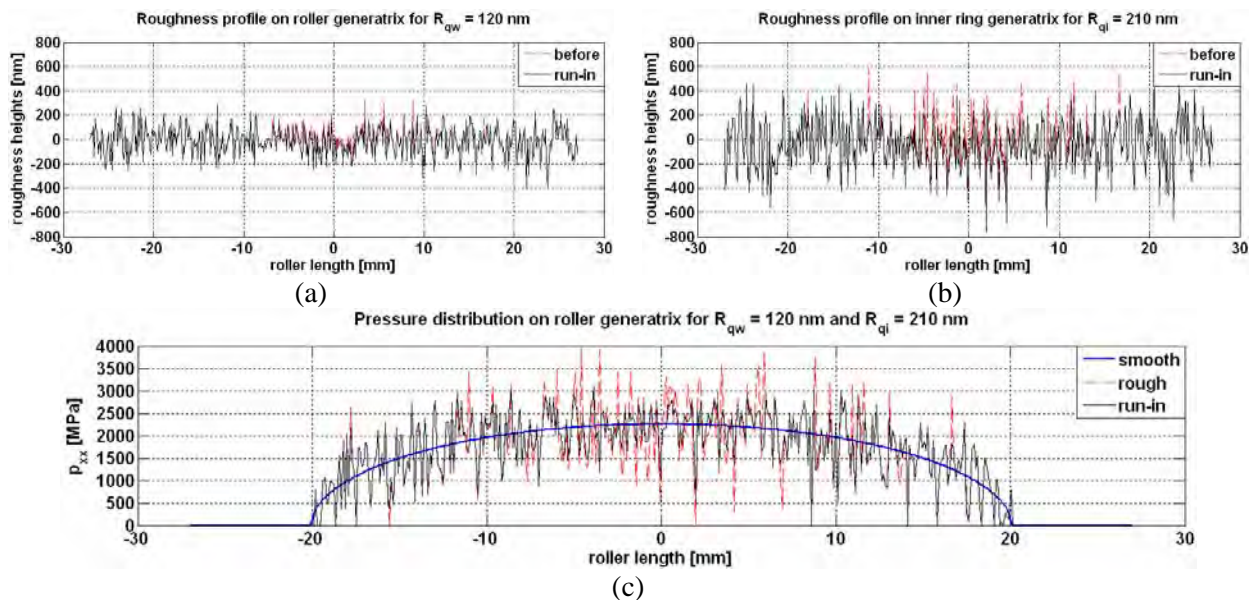


Figure 3. Numerical results for highest loaded roller-inner ring contact ($R_{qw1} = 120\text{ nm}$, $R_{qi1} = 210\text{ nm}$): (a) roughness profile on roller (before and after run-in), (b) roughness profile on inner ring (before and after run-in) and (c) pressure distribution.

The 2D pressure distributions on roller generatrix for the highest loaded roller-inner ring contact are presented in figures 1(c), 2(c) and 3(c). In comparison with a smooth contact surface it can be observed that the presence of the roughness on the contact surface generates peaks in pressure distributions. The pressure peaks are higher as the roughness is more grossly and have the maximum value of 2700 MPa for the fine roughness, 3200 MPa for the medium roughness and 4000 MPa for the grossly roughness. In the middle of the contact length the maximum pressure for the smooth contact surface is 2250 MPa .

It can be observed that after 300 running cycles the pressure peaks are slightly diminished in the middle of the contact length for the fine and medium roughness and are significantly diminished on the all contact length for the grossly roughness.

Table 1. Rating lives for light loading conditions ($F_R = 0.055 \cdot C = 33.5\text{ kN}$)

Roller roughness R_{qw} [nm]	Inner ring roughness R_{qi} [nm]	Rating life, L_{10} , hours, [16]	Modified rating life, L_{10mr} , hours, [14]	
			Before	Run-in
smooth	smooth		688750	
40	70	264700	218660	324140
80	140		28205	74993
120	210		2297	38602

In table 1 are presented the modified lives L_{10mr} for light loading conditions ($F_R = 0.055 \cdot C = 33.5\text{ kN}$). The values of the modified rating life are smaller for the rough surfaces than for the smooth surface. For the case of modified surfaces after 300 running cycles with medium radial loading, it can be

observed an increase of the modified rating life, apparently a higher increase for the grossly roughness, approximately 16 times more than before run-in (from 2297 hours to 38602 hours), but a significantly increase for the fine roughness, approximately 105000 hours more than before run-in (from 218660 hours to 324140 hours).

4. Conclusions

The topography of the active surfaces in rolling contact depends on the surface manufacturing process technology. Numerical results presented in this paper evidence the fact that the presence of nano-asperities on contact surfaces influence the running-in process and durability of rolling contacts.

It was used a numerical method to generate an arbitrarily defined three-dimensional rough surface, a elastic-plastic model to take into account the running-in process and the new methodology given by ISO 16281 to evaluate the modified rating life.

The presence of nano-asperities on contact surfaces generates peaks in pressure distributions, higher peaks for surfaces with grossly roughness. For surfaces with coarser roughness the running-in process is more pronounced than for surfaces with a finer roughness.


The modified rating life it is severely diminished for surfaces with coarser roughness (by two orders of magnitude), even after running-in process (by one order of magnitude) than for smooth surfaces or with a finer roughness.

5. References

- [1] Robbe-Valloire F 2001 Statistical analysis of asperities on a rough surface *Wear* **249** pp 401-408
- [2] Taylor Hobson Precision 2003 *Exploring surface texture* (TH Ltd)
- [3] Stawicki T, Sedlak P, Koniuszy A 2010 The testing of the influence of the roughness of the crankshaft journal upon the durability of the crankshaft bearing in engines of agricultural machines *Sci. probl. of mach. op. and maint.* **4** pp 7-17
- [4] Allwood J, Ciftci H 2005 An incremental solution method for rough contact problems *Wear* **258** pp 1601-1615
- [5] Allwood J 2005 Survey and performance assessment of solution methods for elastic rough contact problems *J. Tribol.* **127** pp 10-23
- [6] Bakolas V 2003 Numerical generation of arbitrarily oriented non-gaussian three-dimensional rough surfaces *Wear* **254** pp 546-554
- [7] Patrikar RM 2004 Modeling and simulation of surface roughness *App. Surf. Sci.* **228** pp 213-220
- [8] Jamari J 2006 *Running-in of rolling contacts* (PhD Thesis Twente)
- [9] Jamari J, de Rooij MB and Schipper DJ 2007 Plastic deterministic contact of rough surfaces *J. Tribol.* **129** pp 957-962
- [10] Benchea M, Iovan-Dragomir A, Crețu S 2014 Misalignment effects in cylindrical roller bearings *App. Mech. and Mat.* **658** pp 277-282
- [11] Crețu S, Benchea M, Iovan-Dragomir A 2016 On basic reference rating life of cylindrical roller bearings. Part II - Elastic-Plastic Analysis *J. Balk. Tribol. Assoc.* **22/1** pp 272-280
- [12] Chaboche JL 2008 A review of some plasticity and viscoplasticity constitutive theories *Int. J. Plasticity* **24** pp 1642-1693
- [13] Besson J, Cailletaud G, Chaboche JL, Forest S and Blétry M 2010 *Non-linear mechanics of materials* (Springer)
- [14] ISO 16281:2008, Rolling bearings-methods for calculating the modified reference rating life for universally loaded bearings
- [15] Linares Arregui I Alfredsson B 2010 Elastic-plastic characterization of a high strength bainitic roller bearing steel - experiments and modelling *Int. J. Mech. Sci.* **52** pp 1254-1268
- [16] ISO 281:2007, Rolling bearings-Dynamic load ratings and rating life
- [17] SKF Group 2013 *Rolling bearings catalogue*

Article

Improvements of Arboblend V2 Nature Characteristics through Depositing Thin Ceramic Layers

Simona-Nicoleta Mazurchevici ¹, Alina Marguta ¹, Bogdan Istrate ², Marcelin Benchea ² , Mihai Boca ¹
and Dumitru Nedelcu ^{1,3,*}

¹ Department of Machine, Manufacturing Technology, "Gheorghe Asachi" Technical University of Iasi, 700050 Iasi, Romania; simona0nikoleta@gmail.com (S.-N.M.); alinamarguta@yahoo.com (A.M.); mihaitzaboca@yahoo.com (M.B.)

² Department of Mechanical Engineering, Mechatronics and Robotics, Faculty of Mechanical Engineering, "Gheorghe Asachi" Technical University of Iasi, 700050 Iasi, Romania; bogdan.istrate@tuiasi.ro (B.I.); marcelin.benchea@tuiasi.ro (M.B.)

³ Mechanical Engineering Department, Technical Sciences Academy of Romania, 030167 Bucharest, Romania

* Correspondence: dnedelcu@tuiasi.ro

Abstract: The paper aims to investigate the behavior of Arboblend V2 Nature biopolymer samples covered with three ceramic powders, Amdry 6420 (Cr_2O_3), Metco 143 (ZrO_2 18 TiO_2 10 Y_2O_3) and Metco 136F (Cr_2O_3 -x SiO_2 -y TiO_2). The coated samples were obtained by injection molding, and the micropowder deposition was achieved by using the Atmospheric Plasma Spray (APS) method, with varied thickness layers. The present study will only describe the results for nine-layer deposition because, as the number of layers' increases, the surface quality and mechanical/thermal characteristics such as wear, hardness and thermal resistance are also increased. The followed determinations were conducted: the adhesion strength, hardness on a microscopic scale by micro-indentation, thermal analysis and structural and morphological analysis. The structural analysis has highlighted a uniform deposition for the ZrO_2 18 TiO_2 10 Y_2O_3 layer, but for the layers that contained Cr_2O_3 ceramic microparticles, the deposition was not completely uniform. The thermal analysis revealed structural stability up to a temperature of 230 °C, the major degradation of the biopolymer matrix taking place at a temperature around 344 °C. The samples' crystalline structure as well as the presence of the Cr_2O_3 compound significantly influenced the micro-indentation and scratch analysis responses. The novelty of this study is given by itself the coating of the Arboblend V2 Nature biopolymer (as base material), with ceramic microparticles as the micropowder coating material. Following the undertaken study, the increase in the mechanical, tribological and thermal characteristics of the samples recommend all three coated biopolymer samples as suitable for operating in harsh conditions, such as the automotive industry, in order to replace plastic materials.

Keywords: biodegradable thermoplastic; coating; Amdry 6420; Metco 143; Metco 136F; hardness; adhesion; structure



Citation: Mazurchevici, S.-N.; Marguta, A.; Istrate, B.; Benchea, M.; Boca, M.; Nedelcu, D. Improvements of Arboblend V2 Nature Characteristics through Depositing Thin Ceramic Layers. *Polymers* **2021**, *13*, 3765. <https://doi.org/10.3390/polym13213765>

Academic Editors: Domenico Acierno and Antonella Patti

Received: 7 October 2021

Accepted: 27 October 2021

Published: 30 October 2021

Publisher's Note: MDPI stays neutral with regard to jurisdictional claims in published maps and institutional affiliations.



Copyright: © 2021 by the authors. Licensee MDPI, Basel, Switzerland. This article is an open access article distributed under the terms and conditions of the Creative Commons Attribution (CC BY) license (<https://creativecommons.org/licenses/by/4.0/>).

1. Introduction

The thermal coating process finds its applicability in areas such as the automotive, aerospace and naval industries in order to improve the corrosion resistance, wear resistance and lifetime of the equipment part as follows: thermal barrier coatings for components that operate in severe thermal conditions (turbine blades, fuel parts, vanes) with the role of increasing their life by improving resistance to oxidation, heat and corrosion [1]; hard metal coatings such as tungsten and chromium carbide are commonly used to increase the wear and corrosion resistance of the parts surfaces [2]; corrosion resistance after heat treatment of a Cr_3C_2 -NiCr coating showed significant improvement due to both the microstructural changes and the presence of a metallurgical bond at the coating-substrate interface [3];

titanium plasma spraying (TPS) used on polymers as polyethylene/polyamide highlighted good mechanical properties and increased hardness [4].

One of the most common thermal deposition techniques is Atmospheric Plasma Spray (APS), and the coatings obtained by zirconium and chromium ceramic layer depositions are widely spread materials in mechanical applications [5]. The main drawbacks of these coatings are given by the micro-cracks, isolation inhomogeneity and residual stresses (appears during cooling process) [6].

The Al_2O_3 (aluminium oxide (alumina)) powder with high purity used for coating, usually applied by the plasma spray method, presents electrical insulation in terms of thermal conductivity and dielectric characteristics. Furthermore, the coatings are wear-resistant, have higher hardness, higher temperature stability and are chemically inert. The ceramic coating is suitable for electrical, electronic and semiconductor manufacturing tool applications, electrostatic chucks and capacitors, vacuum chamber lines, etc. The high purity of the material ensures that it will not contaminate the semi-conductor components [7]. Nickel, zirconium, aluminium, molybdenum and chromium, as powder elements, are a good choice for applications that require high toughness with moderate resistance to fretting, erosion and scuffing. Zinc-based coatings are widespread in applications that require increased corrosion resistance, but if this chemical element is not alloyed with other elements such as tungsten carbide or nickel, it has low mechanical characteristics [8]. The degradation of the Zn-polymer interface has been studied by the authors of the paper [9], and they point out that the delamination can be inhibited by CO_2 gas in a humid environment. Inhibition depends very much on the polymer matrix's affinity for carbon dioxide. Other researchers such as [10] have used nano-zinc-oxide (5 wt %) and epoxy acrylate in order to obtain a corrosion protection coating for mild steel panels.

It is well known that the addition of ceramic particles, metals particles and biopolymers as a substrate provides a combination of properties of all three types of materials: biopolymer matrices and metallic and ceramic reinforcement components. This may result in the improvement of the physical and mechanical properties of the composite [11].

In the literature, the applications of function coatings refer mainly to corrosion protection characteristic, and there is a limited emphasis on equally important properties—for example, mechanical robustness, which is significant for determining the applicability of developed coatings. However, there are discussions on the principal working theories, procedures for preparation, performance investigations and applications of superhydrophobic coatings, for instance: a viable preventative method for controlling metal corrosion due to their mechanical stability and durability, and the shortcoming consists in the ability of maintaining this characteristic for a prolonged period of time [12]; corrosion inhibition of metallic materials with the help of smart coatings involves difficulties in achieving some features as thermal stability, resistances to scratching and strong chemical acids, high optical transmission, in situ healing, etc. [13]; coating of stainless steel and titanium bipolar plates in order to improve the corrosion resistance and electrical conductivity in PEMFC (proton-exchange membrane fuel cells), which has, for the moment as the main impediment in the large-scale spread of the product, a high manufacturing cost [14]; excellent anticorrosion durability obtained by coating the polyaniline-graphene oxide composite with zinc-based waterborne [15]; anticorrosive coatings in the marine field face the degradation, loss of adhesion and failure of coating systems [16]; metallic substrates (aluminum alloy) coated with active corrosion protection systems (with self-healing ability) such as silica-zirconia nanoparticles highlighted long-term corrosion protection and the ability to self-heal defects, and these characteristics are obtained by rigorous control of the inhibitor regular release at the moment when the corrosion process begins to arise [17]. A comparative review that accounts for all factors, including the durability and other mechanical properties, is essential for understanding the applicability of an advanced coating at a practical level.

In addition, another area targeted by coating researchers is related to composites based on polymer matrices with the inclusion of magnetic nano-sized particles: Polydimethylsiloxane (PDMS) coated with different concentrations of nanosized Ni@C core-shell [18];

Ni-silicone elastomagnetic composites [19]; polyacrylamide-based hydrogels coated with Ni ferrite [20]; polyetherurethane (TFX) and a biodegradable multiblock copolymer (PDC) with poly(p-dioxanone) as hard segment and poly(ϵ -caprolactone) as soft segment were investigated as matrix component, coated with iron oxide particles [21]; and oligo(ϵ -caprolactone)dimethacrylate/butyl acrylate, coated with Fe_3O_4 [22]; carbon-fiber–epoxy composites coated with two thermal ceramic particles (lass flakes and aluminum titanate) in order to create a thermal barrier for the substrate [23]. The interest of researchers was focused mainly on elastomagnetic effects [19] and the wide prospects of applications as follows: Ni ferrite with a highly organized structure as humidity sensors [20]; magnetic nanoparticles for practical applications which involve sensors and biosensors [24]; magnetoresistive sensors for applications where the ultimate field detection limits are required or as readers in hard disk drives [25]; Mg substitution on Ni-ferrite ceramics with applications in biomedicine, gas detection, heterogeneous catalysis, adsorption, etc. [26]; shape-memory materials through the inductive heating of magnetic nanoparticles in thermoplastic polymers [21]; and the incorporation of surface-modified superparamagnetic nanoparticles into a polymer matrix [22]. These materials also demonstrate prospects for biomedicine: drug delivery, hyperthermia, magnetic resonance imaging contrast enhancement [27] and the manipulation of cell membranes [28]; recording media and high-frequency applications—electromagnetic-wave-absorption materials [29], microwave absorption [30] and gigahertz microwave absorption [31].

In this paper, the authors have analysed three types of plasma jet coatings for intermediate layers (micrometallic powder) and one type of ceramic coating (aluminium oxide). The coatings were made on Arboblend V2 Nature substrate materials. The samples were obtained using injection moulding, and the method used for coating was atmospheric plasma spraying.

The registered trademark Arboblend[®], developed by scientists and engineers from the German company Tecnar in collaboration with those from the Fraunhofer Institute for Chemical Technology, is a 100% biodegradable biopolymer [32], and a part of the current research group has investigated the behavior of samples covered with metallic intermediate layer and ceramic final layer in the past but not at such a deep level and not following an experimental plan [33].

The aim of the manuscript was to obtain a new material with improved properties that can then be used successfully as a substitute for synthetic plastics in the automotive industry. Given this objective, the biodegradable material Arboblend V2 Nature was chosen, for which the research team previously studied the properties. The next step was to realize the coating with ceramic microparticles by using the APS method, after which the same characteristics were studied. The present study is not found in the research activity of other authors, so the proposed research through both technology and experimental results is constituted as a novelty element.

The introduction section provides a coatings overview. This chapter is followed by a description of the materials and methods used in the analysis of the coated samples. The results of the experimental research are presented and commented on in Section 3.4, and the conclusions part suggestively presents general comments on the main obtained results.

2. Materials and Methods

The thermoplastic material selected to be coated with ceramic microparticles was Arboblend V2 Nature. According to the information provided by the producers but also to some studies from the specialized literature [32,34,35], the basic matrix of the polymer is lignin, this being extracted from annual vegetable plants, so it is not necessary to use wood raw materials that require dozens of years or even longer to reach maturity and be used in the forestry and paper industry. This is important to mention because another source of lignin used for this material comes from its extraction from the paper industry waste. In addition, the Arboblend V2 Nature structure can contain a significant amount of polylactic acid (PLA—also biodegradable polyester) and other constituents such as bio-polyamides

(bio-PA), cellulose, natural vegetable fibers and, for processing in good conditions, contains a small amount of natural additives (resins, waxes, shellac) [33,36,37].

Obtaining the necessary samples for coating with ceramic layers was realized by injection in the mold using the SZ-600H equipment (SHEN ZHOU, Zhangjiagang, China). The dimensions of the samples were $(70 \times 50 \times 10)$ mm³. The following technological parameters were used for injection: material melting temperature—165 °C; injection pressure—100 MPa; injection speed—80 m/min; cooling time—30 s.

The preparation of the rectangular biopolymer samples consisted in the fixed adhesion between metal strips, followed by the blasting and removal of impurities in order to obtain a surface roughness that was as low as possible. The final stage of preparation was degreasing with ethyl alcohol.

Atmospheric plasma spray (APS) technology (SPRAYWIZARD-9MCE, Sultzer-Metco, Westbury, New York, USA/9MBspraying gun) was used to cover the injected samples. The technological coverage parameters used are shown in Table 1.

The deposition rate of the microparticles was constant. The thickness of the deposited ceramic layer was of the micrometers order and for the thermal control of the samples' melting temperature, a laser pyrometer was used throughout the process.

Three ceramic powders were used for the coating: Amdry 6420 (Cr₂O₃), Metco 143 (Cr₂O₃-xSiO₂-yTiO₂) and Metco 136F (ZrO₂ 18TiO₂ 10Y₂O₃). The three micropowders were deposited on three samples injected from Arboblend V2 Nature. On each sample, a distinct number of passes was made, namely, 5, 7 and 9 passes, in order to study the improvement or not of the mechanical characteristics with the increase in the deposited ceramic layer. However, this manuscript will only present the results for the samples obtained by performing 9 passes, because the objective of the paper is to highlight the uniformity and homogeneity of the deposited layers, which is not entirely revealed by the samples obtained with 3 and 5 passes. The experimental plan used to cover the samples with ceramic micropowders is highlighted in Table 2.

Table 1. Technological parameters used during the counting process.

Powder	Gun Type	N ₂ Pressure (Bar)	N ₂ Gas Flow (NLPM)	H ₂ Pressure (Bar)	H ₂ Gas Flow (NLPM)	Electric		9MP Powder Dispenser			Amount (g/min)	Spray Distance (mm)
						DC (A)	DC (V)	Carrier Gas Flow (NLPM)	Air Pressure (Bar)			
ZrO ₂ 18TiO ₂ 10Y ₂ O ₃	9MB	3.4	44	3.4	6.6	400	70–80	5.3	1.4	144	137	
Cr ₂ O ₃		3.6	39	3.6	6.6	400	70–80	5.1	1.4	126	145	
Cr ₂ O ₃ -xSiO ₂ -yTiO ₂		3.7	42	3.7	6.6	400	70–80	5.1	1.4	132	145	

Table 2. Experimental plan used to cover the samples with ceramic layer.

No.crt.	Sample Number	Powder Type	Number of Passes
1	1	143	5
2	2	143	7
3	3	143	9
4	4	6420	5
5	5	6420	7
6	6	6420	9
7	7	136	5
8	8	136	7
9	9	136	9

The ceramic micro powders were purchased from the Oerlikon Metco manufacturer (Bella Vista, New South Wales, Australia). The microparticles dimensions and shapes are varied as follows [38]:

- Chromium Oxide Thermal Spray Powder, Amdry 6420 (Cr_2O_3): angular, blocky morphology, (10–105) μm ;
- Chromia–Silica composite powder, Metco 136F ($\text{Cr}_2\text{O}_3\text{-xSiO}_2\text{-yTiO}_2$): irregular or angular/blocky morphology, (9–110) μm , Cr_2O_3 —Balance; SiO_2 —(3.0–4.5)%; $\text{TiO}_2 < 4.0\%$;
- Zirconia–Titania–Yttria Composite Powder, Metco™ 143 ($\text{ZrO}_2\ 18\text{TiO}_2\ 10\text{Y}_2\text{O}_3$): spheroidal morphology; typically particle size between (3–40) μm ;
- The microindentation and scratch tests used the CETR UMT-2 microtribometer (Universal Materials Tester, CETR®, Campbell, SUA). Test conditions were as follows:
- Scratch analysis: a blade with a tip of 0.4 mm (radius at the tip) was used, the samples were fixed on the table and during the test samples were pressed with a vertical force of 10 N NVIDIA blade, moving the table over a distance of 10 mm in 60 s, and the test speed was 0.167 mm/s. The software performed the automatic test and recorded the following parameters: vertical force F_z , horizontal force F_x , time and distance of movement in the horizontal direction Y (of the fixing mass of the sample).
- Microindentation test: the Rockwell type indenter was used (cone with diamond tip having an angle of 120° and a radius at the peak of 200 microns), the samples were fixed on the table and during the test samples were pressed with a vertical force of 10 N (with steps/times described in work). Three samples of each type of powder were tested in order to be able to calculate the parameters statistically with the highest possible accuracy (hardness and Young's modulus). The software performed the automatic test and recorded the following parameters: vertical force F_z , time and vertical travel distance C of the indenter (with capacitive sensor). Other process parameters were loading time—30 s; holding time—15 s; unloading time—30 s; and sensor of (0.2–20) N. Microindentation tests involved testing three samples for each type of ceramic powder in order to confirm experimental repeatability. The average values were obtained by calculating the arithmetic average, and the standard deviation highlights the variation in a set of numbers compared to the calculated average value.

In order to determine the thermal, structural and morphological behavior, only the samples with 9 successive passes were selected for this study: sample 3 coated with Zirconia–Titania–Yttria Composite Powder, Metco™ 143, further noted with P3–143–9 passes; sample 6 coated with Chromium Oxide powder, Amdry 6420, noted with P6–6420–9 passes; sample 9 coated with Chromia–Silica composite powder, Metco 136F, noted with P9–136–9 passes. The used equipments for these analyzes were as follows:

Differential scanning calorimetry (DSC) was performed on a DSC 200 F3 Maia differential scanning calorimeter (NETZSCH-Gerätebau GmbH, Selb, Germany). The calibration of the device was realised in accordance with mercury (Hg), zinc (Zn), Indium (In), Tin (Sn) and Bismuth (Bi) standards. The mass of the analyzed samples was less than 30 mg. The experiments were analyzed in the atmosphere of inert gas (Ar). In this experiment, a sample and a reference (an empty crucible) were subjected to the same temperature program. The temperature program consisted of heating from room temperature ($\text{RT} \approx 20^\circ\text{C}$) to 200°C , then cooling from this temperature to RT. The heating and cooling speed used was 10 K/min. During the experiment, the reference and sample temperatures were measured and the temperature difference recorded between the two was converted into heat flux. The recorded thermograms were then evaluated using Proteus software (provided by NETZSCH). The tangent method was used to determine the transition temperatures. The area was determined by using a rectilinear baseline. Temperature of the transformation beginning (T_{onset}), temperature assigned to the peak (T_{peak}), temperature at the end of the transformation (T_{end}) and the amount of absorbed or dissipated heat were determined.

Thermogravimetric curves (TG), derived thermogravimetric curves (DTG) and differential thermal analyzes (DTA), were determined using Mettler Toledo TGA/SDTA 851

equipment. The mass of samples subjected to thermal decomposition was between 2.9 and 3.9 mg. It was worked in an air atmosphere with a flow rate of 20 cm³/min. The study was realized in the temperature range of 25–700 °C using a heating rate of 10 °C/min. The processing of thermogravimetric curves was performed with the STARe SW 9.10 software from Mettler Toledo (Columbus, OH, USA). As in the case of DSC analysis, the beginning (T_{onset}), maximum (T_{peak}) and end (T_{end}) temperatures of each thermal degradation stage were determined. For each identified stage, it is indicated the loss mass percentage residue (W%).

SEM structural analysis (Scanning Electron Microscopy) was performed on the QUANTA 200 3D electron microscope (FEI Company, Fremont, CA, USA). Micrographic maps of the samples coated with ceramic micropowders were made on their surface to observe mainly the uniformity of the deposition. The main parameters considered were the following: the pressure inside the microscope chamber—60 Pa; detector—(Large Field Detector) for the analysis of non-conductive samples such as polymers, textile fibers, powders, etc.; tilt angle—0°; secondary electron acceleration voltage—20 Kv; working distance—15 mm; magnification power—500×–2000×.

To determine the chemical elements that appeared with the deposition of the ceramic layers, an Energy-dispersive X-ray spectroscopy (EDX) together with a SEM was performed. The SEM equipment was VegaTescan LMHII (TESCAN ORSAY HOLDING, Kohoutovice, Czech Republic) with EDX detector X Flash 6I10 from Bruker, Germany, using Esprit 2.2 software. The type of EDX analysis was in-line in order to capture as accurately as possible the difference in chemical composition between the resulted microceramic layer and substrate material.

X-ray diffraction analysis (XRD) was performed with the X'Pert Pro MRD X-ray diffractometer, which has a Cu $k\alpha$ anode X-ray tube, λ –1.54 Å, Panalytical equipment (PANalytical, Almelo, the Netherlands), on which a voltage of 45 kV was applied, the variation of the diffraction angle (2θ) being between 10 and 90°. Two X'Pert Data Collector programs were used to process the data and make the diagrams, namely X'Pert High Score Plus version number 3 and X'Pert Data Viewer version number 2.2 g (Malvern Panalytical, Malvern, UK). This analysis aimed to identify the existence of crystallization phases specific to ceramic micropowders deposited on the surface of the samples from Arboblend V2 Nature. The identification of the crystallization phases was performed by comparing the obtained data with those from the scientific literature.

The chemical composition analyses were performed in five distinct points, and an overall average composition was made with the help of Minitab software.

3. Results and Discussion

3.1. DSC Analyse

In order to establish the physical transformations that take place during the gradual heating of the Arboblend V2 Nature samples coated with ceramic micropowders, a DSC analysis was performed. Three distinct samples were used, one from each type of powder: P3–143–9 passes; P6–6420–9 passes; and P9–136–9 passes. The sample size was less than 5 mm; their mass was less than 20 mg.

During the heating of the three selected samples, three transformations were highlighted, two of them endothermic (Ist and IIIrd) and one exothermic (IInd), the same thermal behavior being highlighted for the sample injected from Arboblend V2 Nature but not covered with a ceramic layer [34,35].

The variation in the heat flow in relation to the recorded temperature for the three phase transformations of each analyzed sample is shown in Figure 1. In order to highlight the possible different thermal compartments of the coated samples, the three signals were overlapped.

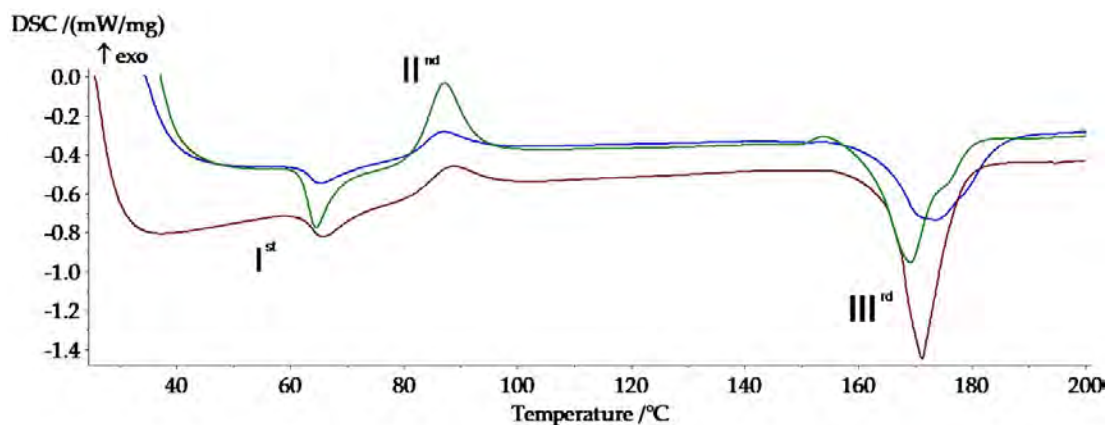


Figure 1. Highlighting the thermal behaviors of the tested samples: Ist—first transformation; IInd—second transformation; IIIrd—third transformation; P3–143–9 passes (green), P6–6420–9 passes (blue), P9–136–9 passes (red).

Both Figure 1 and Table 3 reveal changes in the temperatures at which the phase transformations take place. This aspect can be attributed to the small but still existing mass difference between the three analyzed samples (P3–143–9 passes 12.6 mg, P6–6420–9 passes 16.7 mg, P9–136–9 14.5 mg). At the same time, the amount of heat absorbed or dissipated is slightly different [39]. Another reason that could have generated this difference is the thickness of the deposited layer with the completion of the nine passes. As the dimensions of the microparticles differ in the case of the three ceramic powders, it is expected that the powder, whose microparticles are larger, will form a thicker layer, and thus the phase transitions will take place at slightly higher temperatures and the amount of absorbed or dissipated heat will be lower.

The critical temperatures of the three transformations are as follows: T_{onset} is the starting temperature; T_{peak} is the middle temperature; T_{end} is the finishing temperature (determined using the tangent method); and $\Delta H/m$ is the amount of dissipated/absorbed heat (using a rectilinear baseline).

Analyzing the first phase transformation, it is observed that the three samples register an endothermic maximum around 65 °C, a slightly lower transition temperature (64.7 °C) than the P3–143–9 passes sample (Zirconia–Titania–Yttria Composite Powder), whose powder has a smaller granulation. The first peak can be associated with a slow monotropic transformation of the solid–solid type and of some metastable crystals [40], which takes place with reduced heat absorption, −8.81 kJ/kg for P3–143–9 passes, −4.29 kJ/kg for the P6–6420–9 passes and −5.57 kJ/kg in the case of the P9–136–9 passes. The variation in the absorbed heat can be attributed, first of all, to the thickness of the deposited layers but also to the mass difference of the analyzed samples.

Table 3. Calorimetric characterization of samples coated with ceramic layers.

Sample	Transformation	T_{onset} [°C]	T_{peak} [°C]	T_{end} [°C]	$\Delta H/m$ [kJ/kg]
P3–143–9 passes	I st	62.0	64.7	68.5	−8.81
	II nd	81.9	87.2	93.0	19.36
	III rd	162.7	169.3	175.3	−40.1
P6–6420–9 passes	I st	62.1	65.3	71.2	−4.29
	II nd	81.4	87.2	94.2	7.16
	III rd	164.0	173.7	185.3	−38.14
P9–136–9 passes	I st	61.8	65.8	71.8	−5.57
	II nd	81.7	88.7	95.6	8.66
	III rd	166.0	171.4	178.0	−48.38

The second peak takes place around the temperature of 86 °C, the powder with the highest granulation, the P9–136–9 passes, registering an increase in the transformation with 1.5 °C higher than the other two covered samples. The exothermic peak can be associated with the base biopolymer crystallization or with the reticular reorganization of lignin, the basic matrix of the biopolymer [39].

The third peak occurs with considerable heat absorption, in the case of all analyzed samples: −40.1 kJ/kg for the sample with smaller microparticles (P3–143–9 passes) and −48.38 kJ/kg for the sample with higher granulation (P9–136–9 passes). The endothermic transformation is attributed to the melting of the Arboblend V2 Nature biopolymer around the temperature of 170 °C, with small variations depending on the size of the ceramic microparticles.

3.2. TG Analyses

Knowing the thermal stability of Arboblend V2 Nature samples coated with ceramic powders is essential because their use in applications that require operation in severe working conditions, whether it is wear resistance or thermal resistance, requires the study of thermogravimetric behavior. It is desirable that the coating with ceramic microparticles increases the mechanical characteristics but also the thermal stability. Figure 2 compares the thermogravimetric (TG), derived thermogravimetric (DTG) and differential thermal (DTA) curves for the three samples coated with ceramic layers made from nine successive passes.

The main thermogravimetric characteristics of the P3–143–9 passes, P6–6420–9 passes and P9–136–9 passes samples are presented in Table 4.

Table 4. Thermogravimetric characteristics of the samples covered with ceramic micropowders.

Sample	Stage	T _{onset} [°C]	T _{peak} [°C]	T _{end} [°C]	W [%]	DTA Characteristic	Residue [%]
P3–143–9 passes	I	289	341	369	84.98	exo	3.81
	II	413	423	436	11.21	exo	
P6–6420–9 passes	I	282	346	373	84.61	exo	6.60
	II	413	426	438	8.79	exo	
P9–136–9 passes	I	281	347	367	88.06	exo	1.68
	II	415	426	438	10.26	exo	

T_{onset}, the temperature at which thermal degradation begins at each stage; T_{end}, the temperature at which the thermal degradation ends at each stage; T_{peak}, the temperature at which the degradation rate at each stage is maximum; W%, percentage mass loss at each stage; residue, the amount of degraded sample remaining at a temperature above 700 °C.

The three coated samples with different ceramic layers highlight two decomposition stages, the first recorded being around a temperature of 345 °C, with a significant mass loss of over 85%: this decomposition is attributed to the structural degradation of the basic constituent of the material, lignin. This stage consists of the formation of aromatic hydrocarbons, guaiacyl-/syringyl-type and hydroxy-phenolic compounds and more [40]. According to the manufacturer [32], another constituent contained by the analyzed biopolymer is PLA, which decomposes in considerable proportions in this temperature range [41,42]. According to the literature [43,44], PLA and pure lignin degrade completely up to a temperature of 500 °C.

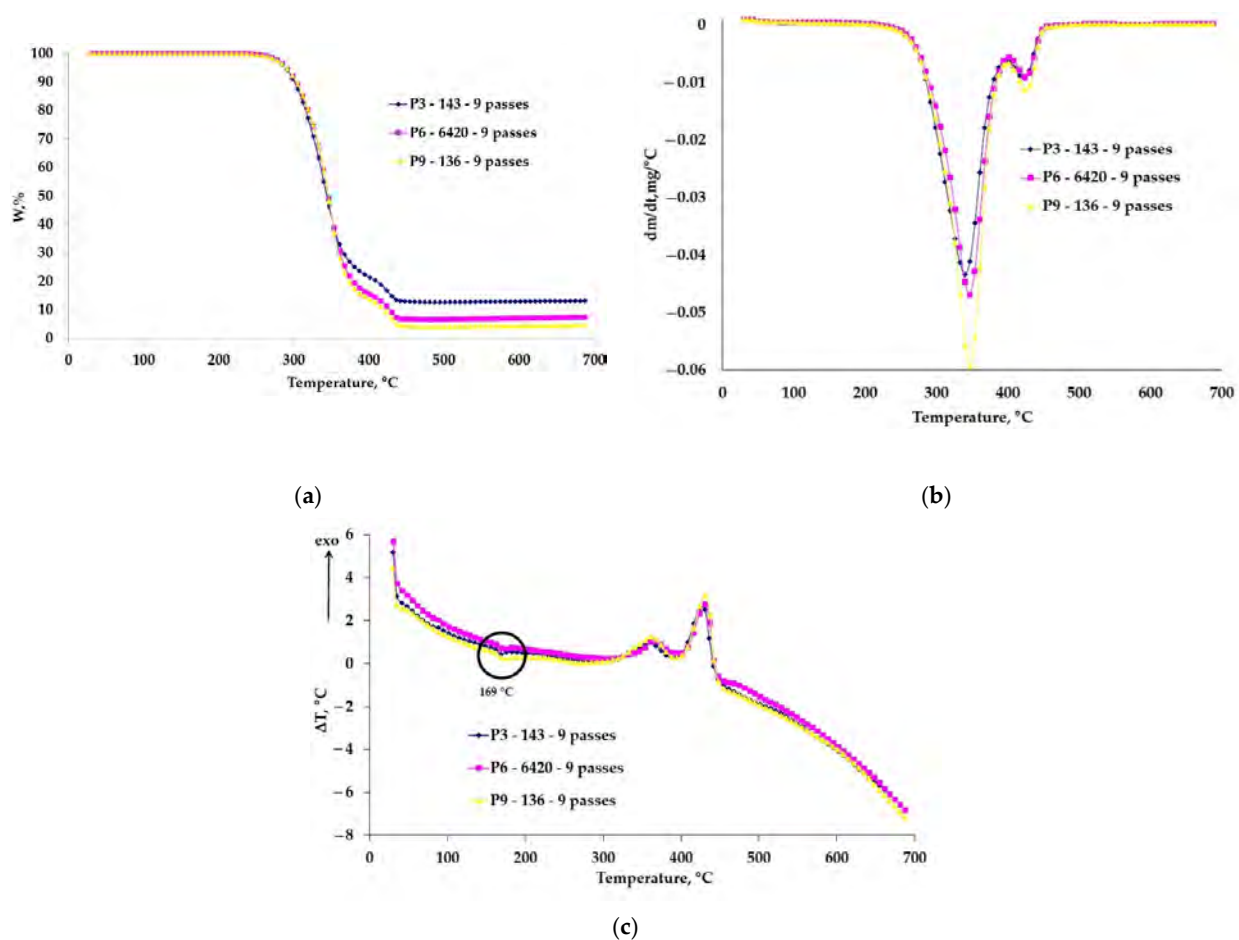


Figure 2. Thermogravimetric curves of the coated samples: (a) TG, (b) DTG and (c) DTA.

The curves obtained from the TG analysis were overlapped to highlight their difference in behavior, and the thermal stability of the coated samples is similar (Figure 2).

In the second stage with a T_{peak} around 425 °C, there is a mass loss in a percentage much lower than 10%, attributed to the thermal oxidation of the carbonic residue that appeared from the pyrolysis of lignin and/or PLA but also of another biodegradable constituent of the biopolymer that was introduced by the manufacturer as a binder (resin, wax, shellac, etc.) [33]. At a temperature of 700 °C, depending on the used ceramic powder type, a certain amount of residual mass is found. It is observed that the sample P6-6420-9 passes has the highest percentage of residue, 6.6%, most likely due to the higher amount of microparticles than, for example, in the case of the P3-143-9 passes sample, where the amount of ceramic powder deposited is much lower. The ceramic powders at the end of the analysis temperature have not yet reached the melting point of approximately 2500 °C, their working temperature varying from 540 °C (P6-6420-9, P9-136-9 passes) to 980 °C (P3-143-9 passes) [38]. In addition, inorganic substances that are found in the composition of the biopolymer are very likely to be part of the residual mass [45].

Figure 2c shows the DTA curves where the melting temperature of Arboblend V2 Nature can be observed, 169 °C, very close to the values obtained by calorimetric analysis, especially in the case of the P3-143-9 passes sample.

3.3. Surface and Structure Analysis of Coated Samples

3.3.1. SEM Analysis

Figure 3 shows the morphological aspect of the Arboblend V2 Nature material coated with Metco™ 143 (ZrO_2 18 TiO_2 10 Y_2O_3). A uniform coating of the biopolymer mass is observed. The coating consists of spherical component particles having a dimensions

variation between 1 and 27 μm . The particles retain their spherical shape due to the very rapid cooling on contact with the base matrix. They do not flatten in the form of splats as is conventional in the case of coatings on metal substrate [46]. The fact that the basic matrix contains various particles in shape and size, in large quantities and evenly distributed, leads to an increase in mechanical properties.

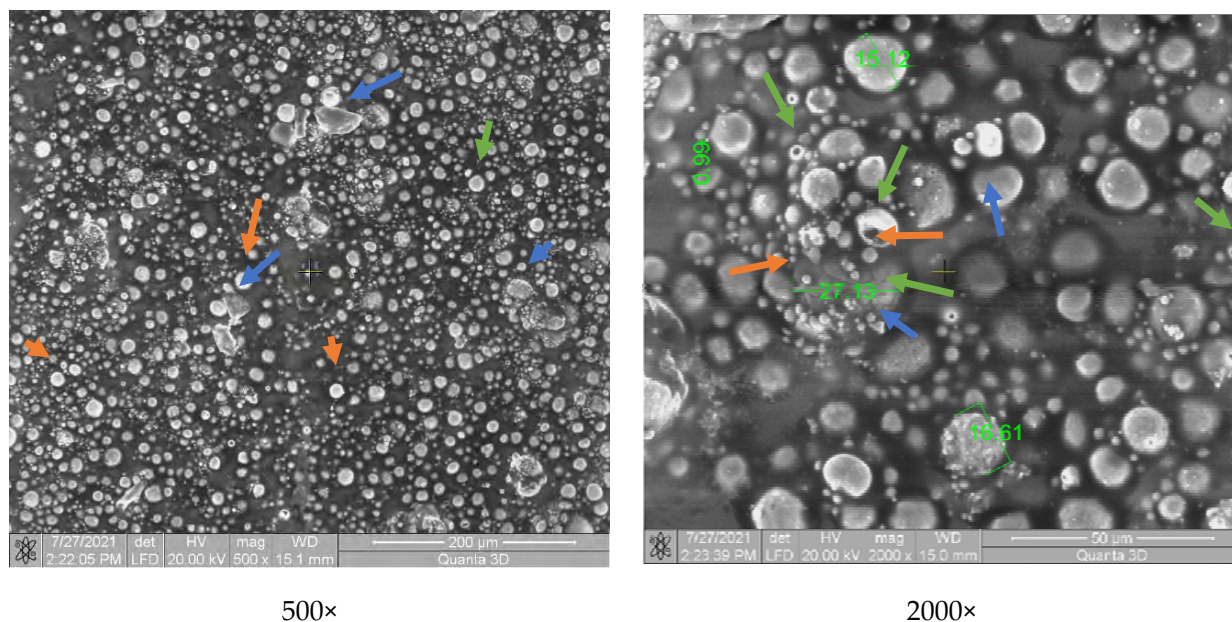


Figure 3. SEM analysis of the P3-143-9 passes samples: Zirconium dioxide (bearing balls)—orange arrow; Titanium dioxide—blue arrow; Yttrium oxide—green arrow.

Yttrium oxide (green arrow, Figure 3) shows a porous spherical morphology in the form of a sintered agglomerate.

Figure 4 shows the polymer matrix containing particles from the coating formed by chromium oxide. Some of these particles are heterogeneously distributed, and another part is embedded in the polymeric structure. Their size varies from 18 μm to 30 μm , and they have rectangular shapes specific to chromium oxide. The spherical microparticles can be attributed to the presence of Fe_2O_3 and SiO_2 , which are released in small quantities in the structure of the Amdry 6420 powder, maximum 0.4% and 0.45%, respectively. Compared to the P3-143-9 passes sample, the material incorporated a smaller amount of powder appearance, which represents the lower capacity of the coating and embedding chromium oxide in the polymeric structure.

The coating of chromium oxide, silicon oxide and titanium oxide ($\text{Cr}_2\text{O}_3\text{-xSiO}_2\text{-yTiO}_2$, Figure 5) highlights a relatively uneven distribution of microparticles, similar to the situation presented in Figure 4. The particles are of different shapes with mostly polyhedral appearance (TiO_2 —green arrow) but there are also spherical (SiO_2 —blue arrow) and rectangular (Cr_2O_3 —orange arrow) structures, their dimensions varying between 1 and 63 μm . The particles are embedded in the polymer mass. Both Figures 4 and 5 show chromium oxide, and this compound does not have a better adhesion compared to the sample coated with P3-143-9 passes (Figure 3), which does not contain chromium oxide.

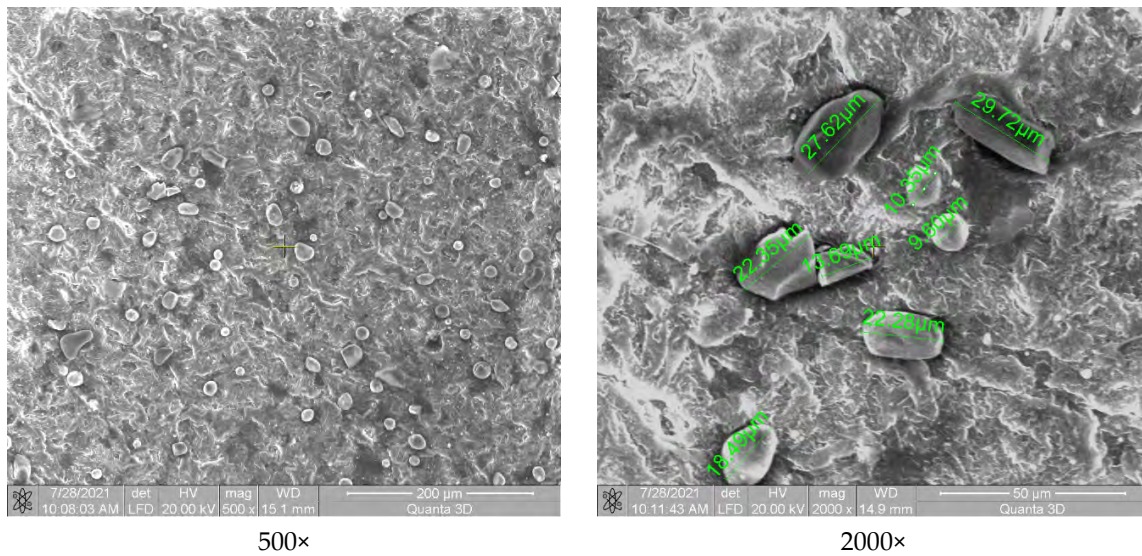


Figure 4. SEM analysis of the P6-6420-9 passes samples.

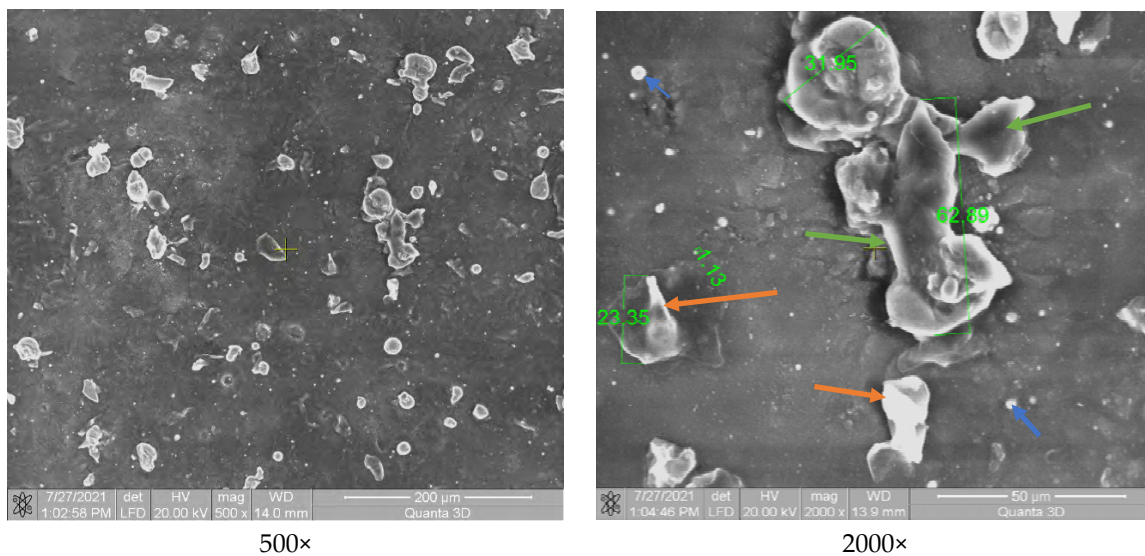


Figure 5. SEM analysis of the P9-136-9 passes samples.

3.3.2. EDX Analysis

In order to observe the presence of the deposited ceramic layers, the line EDX analysis was performed together with the SEM analysis of the P3-143-9 passes, P6-6420-9 passes and P9-136-9 passes samples. This analysis series had as the point of study the edge area of the samples in order to highlight as accurately as possible the presence, distribution and concentration of the chemical elements which form the ceramic microlayers and also the biopolymeric support.

The EDX in-line analysis (Figure 6—yellow arrow) of all samples reflects the abundant presence of two chemical elements, carbon and oxygen. Their existence is closely related to the chemical composition of the biopolymer matrix which presents, according to the previous determinations, C and O in similar mass proportions, $48 \pm 0.02\%$ and $52 \pm 0.02\%$, respectively [35]. The acquisition of data is a difficult one because the polymer matrix is not an electrical conductor, so the electrons coming out of the material are of much lower intensity than, for example, in the case of an analyzed metallic material.

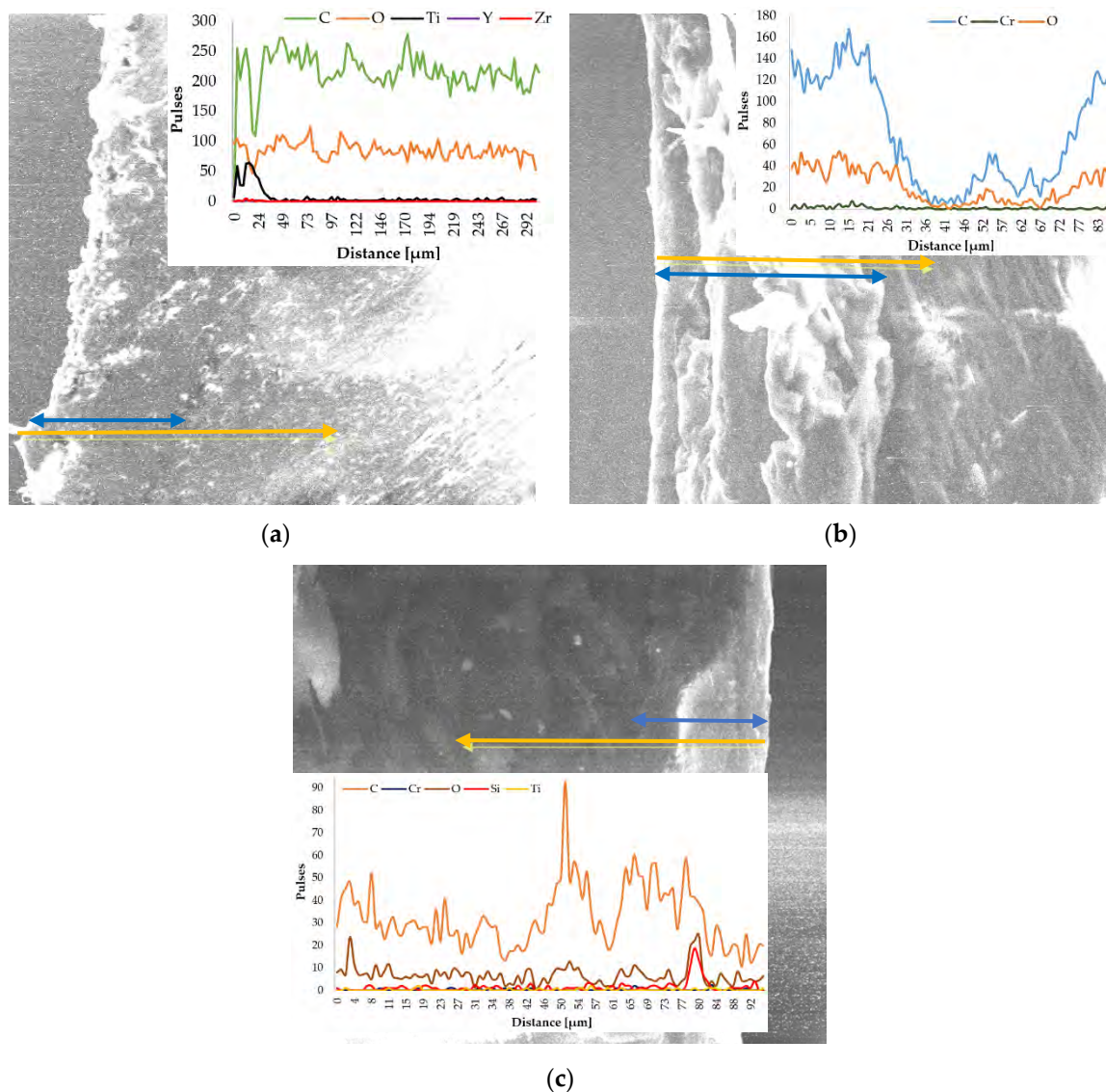


Figure 6. In line EDX analysis of the coated samples. (a) P3–143–9 passes, (b) P6–6420–9 passes, (c) P9–136–9 passes.

For the sample covered with Zirconia–Titania–Yttria Composite Powder (Figure 6a), the presence of ceramic microparticles in the first 20 μm is observed, an area that we consider to coincide with the thickness of the deposited ± 0.02 ceramic layer (blue arrow). Titanium is the chemical element found in the most significant amount in the area of the ceramic layer, but the other two elements are highlighted by the graphic. The presence of a small amount of Zr and Ti during the entire test distance is due to the microparticles that came off of the brittle ceramic layer in the moment of EDX preparation. The higher amount of carbon than oxygen is attributed to the carbides that form during the embedding of molten microparticles in the solid (cold) polymeric matrix, carbides that provide surface hardness. Oxides are also formed but in a much smaller amount.

Chromium being a hard metallic element during the preparation of the P6–6420–9 passes sample, this one is visible over the entire analyzed surface; however, it can be observed that in the first part of the analyzed distance (first 20 μm), the amount of chromium is higher (Figure 6b). As in the case of the P3–143–9 passes sample, the amount of carbon is higher than that of oxygen. In the 35–75 μm interval, the graph highlights a steep decrease in the amount of elements reflected by the sample, but most likely this can be attributed to the transition between the deposited layer and the biopolymer support.

For the P9–136–9 passes sample (Figure 6c), the in-line analysis reveals the presence of the ceramic layer on the right side of the SEM image (last 15 μm), and the graph reflects the existence of the micropowder chemical elements. Silicon being a semiconductor chemical element reflects its presence in the structure of the ceramic layer much more than the other constituents. The Cr, Ti and O of the composite micropowders were highlighted by the analyzed sample.

3.3.3. XRD Analysis

The main purpose of the XRD analysis was to determine the structure of the samples made of Arboblend V2 Nature and coated with ceramic micropowders, Amdry 6420 (Cr_2O_3), Metco 143 (ZrO_2 18 TiO_2 10 Y_2O_3) and Metco 136F (Cr_2O_3 -x SiO_2 -y TiO_2), but also to identify possible crystal phases.

Figure 7 shows the phase diffractograms for the three samples with distinct ceramic coatings: P3–143–9 passes, P6–6420–9 passes and P9–136–9 passes. It can be seen that two of the three samples have a crystalline structure (P3–143–9 passes, P9–136–9 passes) highlighted by specific peaks, and the third (P6–6420–9 passes green diffractogram) has a semi-crystalline structure with the presence of small peaks of chromium oxide at four distinct 2θ angles, 24.25° , 33.39° , 35.88° and 54.61° , respectively, of low intensity, 1036 to 1356 [47–49]. The major peak registered at 16.73° , with a diffraction intensity of 2643, which, according to the literature, may be associated with the presence of polylactic acid in its the chemical composition $((\text{C}_3\text{H}_4\text{O}_2)_n)$ [50,51]. The presence of this compound is not accidental because it is due to the fact that the thickness of the deposited layer is very thin (small microparticles), thus, the equipment is detecting one of the basic material constituents.

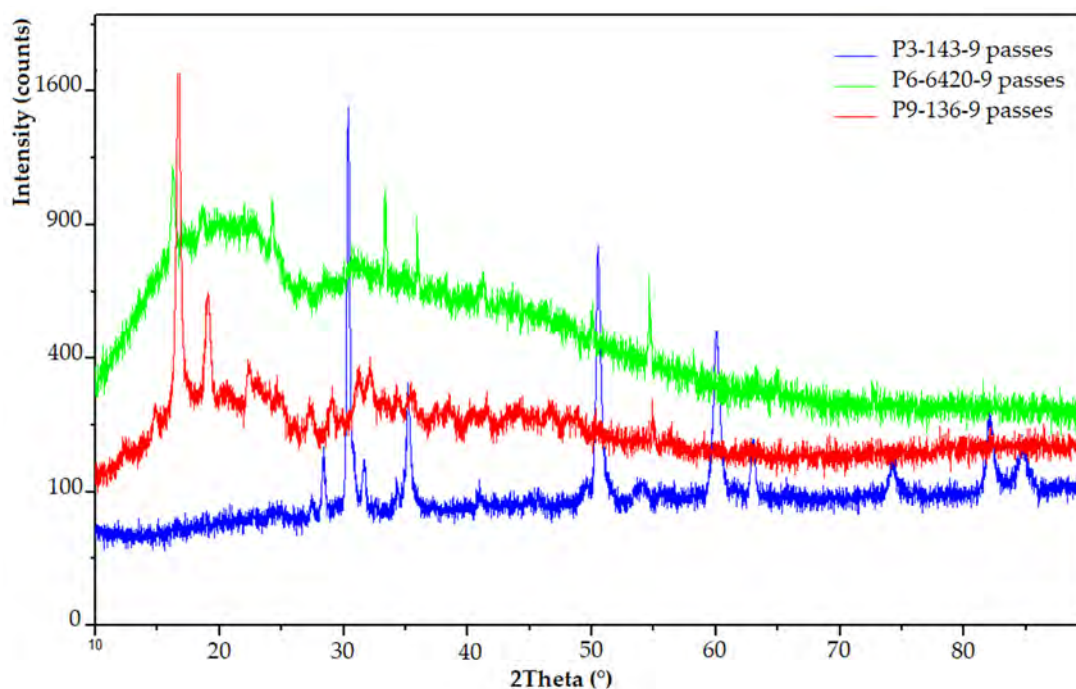


Figure 7. XRD analysis for ceramic coated samples: P3–143–9 passes (blue), P6–6420–9 passes (green), P9–136–9 passes (red).

In the case of the other two coatings, the presence of predominant peaks is observed, which correspond to the crystallization of certain compounds as follows:

- The P3–143–9 passes sample (blue diffractogram) has a strong crystalline aspect due to the large amount of zirconium dioxide particles present in the structure of the ceramic powder. Thus, to the ZrO_2 compound can be assigned the peaks from $2\theta = 31.14^\circ$, 38.43° , 60° , 82° and 84.78° [46,52,53]. Titanium dioxide, as in the case of the P9–136–9 passes sample, is found at angles of 27.43° , 28.34° , 63.02° and 74.41° [54,55]. However,

the intensity of the diffraction peaks is quite low, the highest being registered in the case of the $2\theta = 28.34^\circ$ angle. The low angle from $2\theta = 43^\circ$, was identified as the specific angle of Y_2O_3 crystallization [56].

- The P9–136–9 passes sample (red diffractogram) shows diffraction maxima associated with the presence of the polymer matrix, which has in its structure polylactic acid (16.73°) and lignin or natural fibers (19.04°) [53,57]. Diffraction angles corresponding to the coating with ceramic micropowder are also visible: The specific peaks to Cr_2O_3 crystallization at 2θ angles of low intensity are 30.35° , 31.70° , 35.16° , 50.48° and 54.12° [47–49,58]. For SiO_2 microspheres, a peak located at about $2\theta = 22.5$ is observed [59]. No other diffraction peaks can be detected for this compound. According to the literature [54,55], the diffraction angles that can be attributed to the titanium dioxide (TiO_2) present are at 27.33° and 32.13° in the case of Metco 136F micropowder.

3.4. Scratch Analysis

The scratch test was performed in order to evaluate the adhesion of the hard (ceramic) coatings made on the surface of the Arboblend V2 Nature biopolymeric material.

Analyzing the curves presented in Figure 8, it is observed that one of them, the green curve (P6–6420–9 passes), shows a sudden and gradual transition of the apparent friction coefficient (A-COF), which means that the adhesion between the deposited thin layer and the polymeric material is better than in the case of the other two coatings due to the presence of chromium oxide. The other two tests have a good scratching behavior, but the P3–143–9 passes test (blue curve), recorded higher A-COF values than in the case of the P9–136–9 passes test.

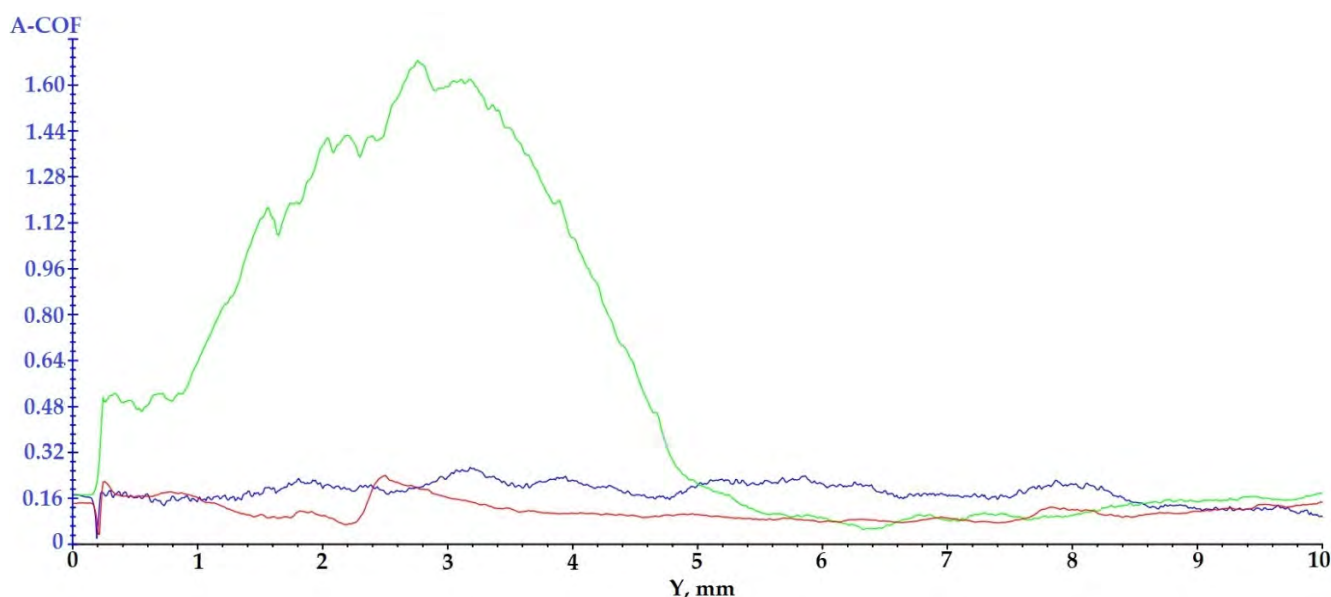


Figure 8. Results regarding the scratching behavior of the samples coated with ceramic layers: blue curve—P3–143–9 passes; green curve—P6–6420–9 passes; red curve—P9–136–9 passes.

The more peaks that appear in the variation of the apparent friction coefficient, the better the adhesion between the deposited layer and the polymeric material is.

For the P6–6420–9 passes sample, a high amplitude peak of A-COF is registered at the beginning of the test; the explanation for this would be related to the deposition granulation. It is very possible that the tip of the cutting tool (pin) has hung an area of deposited material with a larger granulation.

The samples injected from Arboblend V2 Nature and coated with ceramic micropowders showed the following behavior during the 60 s of testing (Figure 9): For sample P3–143–9 passes, blue curve, an increase in A-COF is observed in the first 4 s, after which

its value begins to decrease sharply until the 16 s when it registers an increase followed quickly by a decrease. Starting with at 19 s, the average value of A-COF increases and begins to stabilize, reaching a maximum value of 0.53 at 50 s. The mean value of A-COF was 0.29 ± 0.16 . The behavior of the sample coated with Zirconia–Titania–Yttria composite powder is a typical one, and the coatings in the first part of the test register variations of A-COF in order to later stabilize. Sample P6–6420–9 passes, green curve, reflects a completely different behavior from the first test. In the first part of scratching, the first 3 s, it reaches the maximum value of A-COF at 1.62, followed by a sudden decrease until 6 s. Next, the sample registers two fluctuations, and starting at 40 s, the A-COF value begins to increase, at the end of the 60 s reaching the value of 1.37. These fluctuations can be attributed to the variable dimensions (9–30 μm) of the microparticles that constitute the ceramic powder. The progressive increase recorded in the last 20 s of testing reflects the fact that the test pin detached ceramic microparticles from the sample surface, thus gradually becoming more and more rough. The mean value of A-COF for this sample, 0.56 ± 0.42 , is the highest compared to the other two tested samples. The last test subjected to tribological determination, P9–136–9 passes, red curve, as well as the previous test, records fluctuations throughout the test with the A-COF value at the end of the test reaching a maximum of 0.37. The average value of A-COF for this sample is the lowest, 0.18 ± 0.08 . The value registered is very close to that of the injected samples and not covered with ceramic layer, 0.16 for rotational determinations and 0.13 for oscillation ones [60]. This similarity comes from the fact that the coverage of the sample was not uniform, the adhesion and incorporation of Chromia–Silica composite powder, as it could be observed in the SEM images being very low, had a very high percentage both in the P6–6420–9 passes test and in the P9–136–9 passes test. This lack of deposition is due to the thermal behavior of chromium oxide, which is found in a very high percentage both in the P6–6420–9 passes and P9–136–9 passes samples.

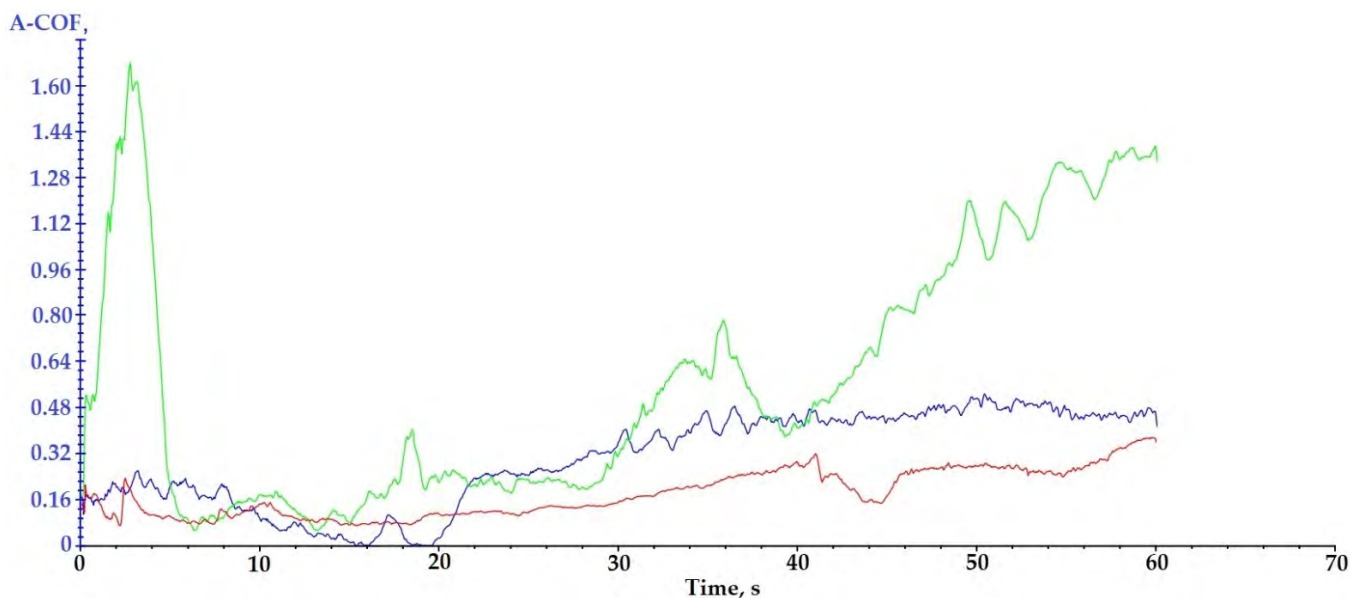


Figure 9. A-COF variation with test time for samples coated with ceramic micropowders: (blue) P3–143–9 passes; (green) P6–6420–9 passes; (red) P9–136–9 passes.

Table 5 shows the results of scratch testing in the case of the three samples covered with ceramic micropowders.

Table 5. Values of A-COF recorded by samples covered with ceramic layers.

Sample	A-COF Medium Value	A-COF Maximum	Time of A-COF Maximum[s]
P3-143-9 passes	0.29 ± 0.16	0.53	50
P6-6420-9 passes	0.56 ± 0.42	1.62/1.37	3.0/60
P9-136-9 passes	0.18 ± 0.08	0.37	60

3.5. Microindentation Test

To conduct the microindentation test, three samples were tested for each type of ceramic powder used to coat the Arboblend V2 Nature biopolymeric material. Repeated testing was to confirm the experimental stability. Figure 10 shows the evolution of the force as a function of the depth of penetration for all three samples subjected to analysis. The software package used (UMT Test Viewer, 2.16) allowed the reading of both the microhardness values and the Young's modulus. These values are presented in Table 6.

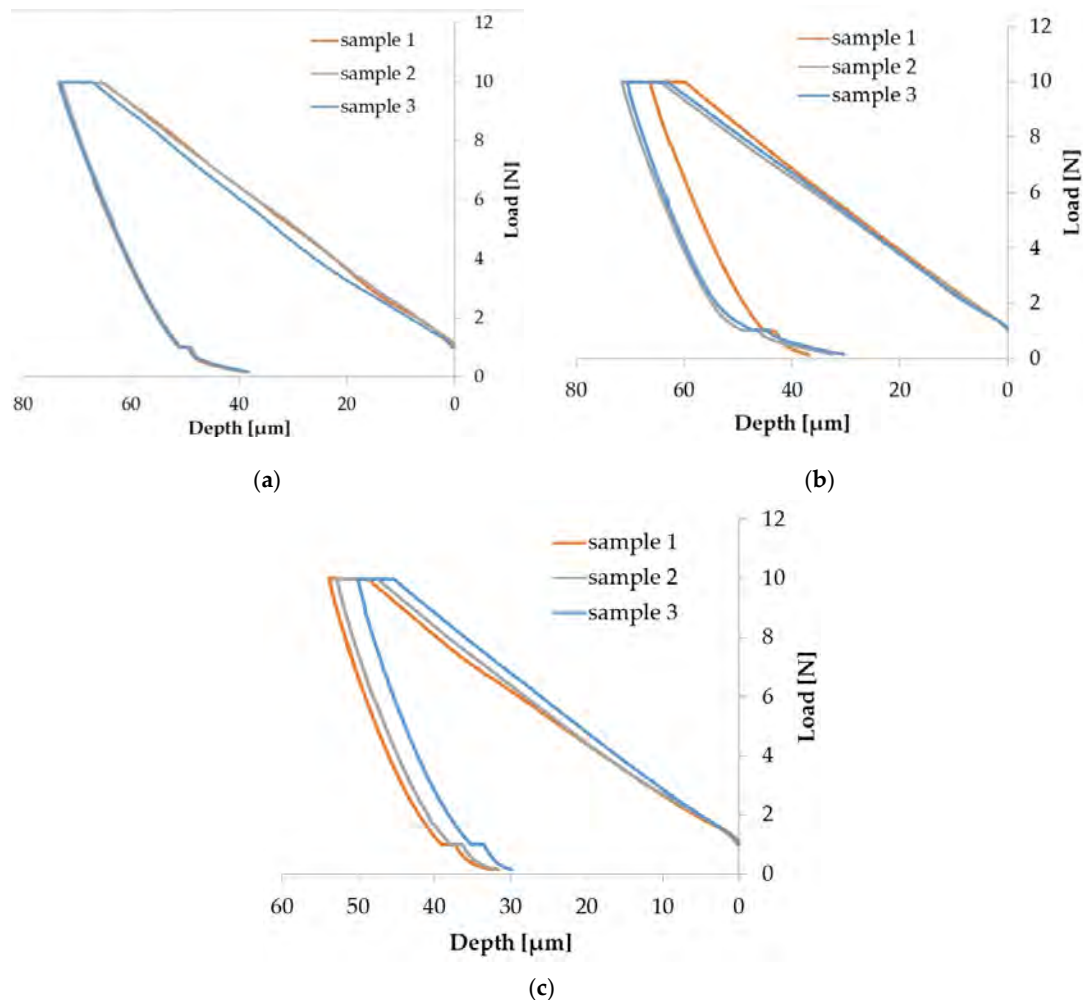


Figure 10. Results of microindentation tests for samples coated with ceramic micropowders: (a) P3-143-9 passes; (b) P6-6420-9 passes; (c) P9-136-9 passes.

The force applied to the indenter increases constantly during the charging phase and is maintained at the maximum value of 10 N. This phase is called creep, after which there is a decrease to zero in the discharge phase.

Table 6. Results obtained by microindenting the samples coated with ceramic micropowders.

Sample	Test	Max Load (N)	Max Depth (μm)	Young's Modulus (GPa)	Micro Hardness (GPa)
P3–143–9 passes	1	8.99	73.55	1.52	0.11
	2	8.7	72.78	1.69	0.11
	3	8.98	73.02	1.48	0.11
Average		8.98 ± 0.01	73.12 ± 0.4	1.56 ± 0.11	0.11 ± 0.00
P6–6420–9 passes	1	8.99	66.64	1.69	0.13
	2	8.98	71.70	1.91	0.11
	3	8.98	71.02	2.53	0.10
Average		8.99 ± 0.01	69.79 ± 2.75	2.04 ± 0.44	0.12 ± 0.01
P9–136–9 passes	1	8.99	53.77	2.92	0.16
	2	8.99	53.08	3	0.16
	3	8.97	50.42	2.9	0.17
Average		8.99 ± 0.01	52.42 ± 1.77	2.94 ± 0.05	0.17 ± 0.01

According to the data obtained from the micro-indentation, the P9–136–9 passes sample, although it does not have a uniform coating, presents the best values of microdurability, (0.17 ± 0.01 GPa), the maximum indentation depth being $52.42 \pm 1.77 \mu\text{m}$. Compared to the zirconium-based ceramic coating (P3–143–9 passes), the chromium oxide coatings have a higher hardness (P6–6420–9 passes, P9–136–9 passes) [35]. Another justification of the results comes from the reduced layer thickness due to the small dimension of microparticles (P3–143–9 passes) than in the case of the other two types of ceramic micropowders.

The lowest dispersion of the results was obtained in the case of the P3–143–9 passes sample, most likely due to the fact that the deposited ceramic layer was uniform. In addition, the other samples tested did not show large differences.

4. Conclusions

The coating of bio-based polymers has gained the attention of researchers worldwide. The purpose of coatings with various layers, be they ceramic, metal, etc., as well as in the case of reinforcements, is to increase the characteristics of the base material so that it responds better to certain industrial applications and can even replace a certain material, such as metal. The coatings have been realized in order to increase the mechanical, tribological and thermal characteristics of the samples (wear, hardness and increase in thermal resistance), thus becoming suitable in applications that require harsh working conditions, especially in the automotive industry. The coating of sample with ceramic microlayers led to the following results:

- A slight increase in the melting point, from $172 \text{ }^\circ\text{C}$ (base material [35,61]) up to $174 \text{ }^\circ\text{C}$, varying depending on the thickness of the deposited layer. The thickness value is closely influenced by the microparticles size that constitute the ceramic powder. Thus, the larger the size of the microparticles, the higher the thermal resistance of the coated material is.
- No significant changes were visible both in terms of temperature range and the amount of mass lost during the thermal degradation, and the differences were also attributed in this situation to the size of the ceramic microparticles.
- Regarding the coatings' uniformity, the SEM surface analysis indicated a good and uniform incorporation of microparticles in the case of composite powder based on zirconium oxide. The other two ceramic micropowders in contact with the polymer matrix did not reveal a good adhesion due to the lower working temperature than the melting point ($2435 \text{ }^\circ\text{C}$).
- XRD and EDX analyses highlighted the presence of microceramic layers. Their crystalline/semi-crystalline structure confers hardness; thus, they are suitable for applications that require this feature. The coating with $\text{Cr}_2\text{O}_3\text{-xSiO}_2\text{-yTiO}_2$ (sample

9) formed the hardest layer (0.17 ± 0.01 GPa), which was demonstrated during the microindentation test. Analyzing the obtained results from the SEM and scratch analyses point of view, it can be concluded that the deposition was not uniform due to the fact that the adhesion between the microparticles of chromium oxide, silicon oxide and titanium oxide is lower than in the case of the other two samples, the average value of the apparent friction coefficient (A-COF) being 0.18 ± 0.08 .

According to the obtained results regarding the adhesion of the ceramic layers on the polymer surface, it can be stated that the samples showed strong chemical bonds at the interface between the thin layers and Arboblend V2 Nature bio-based polymer. Thus, these coated materials can be used in industrial applications that require high surface hardness and thermal resistance. They can also successfully replace various non-biodegradable polymeric materials used in various applications such as those in the automotive and electronics industry (telephone covers, housings, worm wheels, car wiper system, etc.).

Author Contributions: Conceptualization, D.N.; data curation, B.I. and M.B. (Marcelin Benchea); formal analysis, S.-N.M. and A.M.; methodology, M.B. (Mihai Boca); supervision, D.N. and B.I.; validation, D.N.; writing—original draft, S.-N.M. and A.M.; writing—review and editing, S.-N.M.; funding acquisition, D.N. All authors have read and agreed to the published version of the manuscript.

Funding: This work was supported by a publication grant of the TUIASI, project number GI/P21/2021.

Institutional Review Board Statement: Not applicable.

Informed Consent Statement: Not applicable.

Data Availability Statement: The data presented in this study are available on request from the corresponding author.

Acknowledgments: This work was supported by a publication grant of the TUIASI, project number GI/P21/2021.

Conflicts of Interest: The authors declare no conflict of interest.

Nomenclature

TPS	Titanium Plasma Spraying
APS	Atmospheric Plasma Spray
PDMS	Polydimethylsiloxane
PDC	biodegradable multiblock copolymer
TFX	Polyetherurethane
PLA	polylactic acid
NLPM	normal litre per minute
DC	Direct Current
DSC	Differential scanning calorimetry
RT	room temperature
TG	Thermogravimetric curves
DTG	derived thermogravimetric curves
DTA	differential thermal analyzes
T _{onset}	starting temperature
T _{peak}	middle temperature
T _{end}	finish temperature
SEM	Scanning Electron Microscopy
LFD	Large Field Detector
EDX	Energy-dispersive X-ray spectroscopy
XRD	X-ray diffraction analysis
W%	percentage mass loss at each stage
A-COF	apparent friction coefficient
Y	testing distance (mm)

References

1. Lu, Z.; Myoung, S.W.; Kim, E.H.; Lee, J.; Hand Jung, Y.G. Microstructure Evolution and thermal durability with coating thickness in APS thermal barrier coatings. *Mater. Today Proc.* **2014**, *1*, 35–43. [CrossRef]
2. Matikainen, V.; Bolelli, G.; Koivuluoto, H.; Sassatelli, P.; Lusvarghi, L.; Vuoristo, P. Sliding wear behaviour of HVOF and HVOF sprayed Cr₃C₂-based coatings. *Wear* **2017**, *388–389*, 57–71. [CrossRef]
3. Suarez, M.; Bellayer, S.; Traisnel, M.; Gonzalez, W.; Chicot, D.; Lesage, J.; Puchi-Cabrera, E.S.; Staia, M.H. Corrosion behavior of Cr₃C₂-NiCr vacuum plasma sprayed coatings. *Surf. Coat. Technol.* **2008**, *202*, 4566–4571. [CrossRef]
4. Wypych, A.; Siwak, P.; Andrzejewski, D.; Jakubowicz, J. Titanium Plasma-sprayed coatings on polymers for hard tissue applications. *Materials* **2018**, *11*, 2536. [CrossRef]
5. Gariboldi, E.; Rovatti, L.; Lecis, N.; Mondora, L.; Mondora, G.A. Tribological and mechanical behaviour of Cr₃C₂-NiCr thermally sprayed coatings after prolonged aging. *Surf. Coat. Technol.* **2016**, *305*, 83–92. [CrossRef]
6. Tsui, Y.C.; Clyne, T.W. An analytical model for predicting residual stresses in progressively deposited coatings Part 1: Planar geometry. *Thin Solid Films* **1997**, *306*, 23–33. [CrossRef]
7. Thermal Spray Materials Guide. Available online: https://www.oerlikon.com/ecomaXL/files/oerlikon_BRO-0001.17_TS_MaterialGuide_EN.pdf (accessed on 4 August 2020).
8. Channagiri Mohankumar Praveen, K.; Avinash, L.; Manjunath Patel Gowdru, C.; Pimenov, D.Y.; Khaled, G. Electrodeposition based preparation of Zn–Ni alloy and Zn–Ni–WC nano-composite coatings for corrosion-resistant applications. *Coatings* **2021**, *11*, 712. [CrossRef]
9. Shkirskiy, V.; Uebel, M.; Maltseva, A.; Lefèvre, G.; Volovitch, P.; Rohwerder, M. Cathodic driven coating delamination suppressed by inhibition of cation migration along Zn polymer interface in atmospheric CO₂. *npj Mater. Degrad.* **2019**, *3*, 2. [CrossRef]
10. Aung, M.M.; Wong, J.L.; Hong, N.L. Improvement of anticorrosion coating properties in bio-based polymer epoxy acrylate incorporated with nano zinc oxide particles. *Ind. Eng. Chem. Res.* **2020**, *59*, 1753–1763. [CrossRef]
11. Rajkovic, A.; Uyttendaele, M.; Deley, W.; Van Soom, A.; Rijsselaere, T.; Debevere, J. Dynamics of boar semen motility inhibition as a semi-quantitative measurement of *Bacillus cereus* emetic toxin (Cereulide). *J. Microbiol. Methods* **2006**, *65*, 525–534. [CrossRef]
12. Divine, S.; Chun-Wei, Y.; Ian, L. Mechanical durability of engineered superhydrophobic surfaces for anti-corrosion. *Coatings* **2018**, *8*, 162. [CrossRef]
13. Ulaeto, S.; Rajan, R.; Pancrecius, J.; Rajan, T.; Pai, B. Developments in smart anticorrosive coatings with multifunctional characteristics. *Prog. Org. Coat.* **2017**, *111*, 294–314. [CrossRef]
14. Asri, N.; Husaini, T.; Sulong, A.; Majlan, E.; Daud, W. Coating of stainless steel and titanium bipolar plates for anticorrosion in PEMFC: A review. *Int. J. Hydrogen Energy* **2017**, *42*, 9135–9148. [CrossRef]
15. Fengjuan, X.; Cheng, Q.; Mingyang, G.; Junzhong, W.; Xinrui, Y.; Hongli, L.; Lin, Y. Anticorrosive durability of zinc-based waterborne coatings enhanced by highly dispersed and conductive polyaniline/graphene oxide composite. *Prog. Org. Coat.* **2018**, *125*, 79–88. [CrossRef]
16. Sorensen, P.; Kiil, S.; Dam-Johansen, K.; Weinell, C. Anticorrosive coatings: A review. *J. Coat. Technol. Res.* **2009**, *6*, 135–176. [CrossRef]
17. Zheludkevich, M.; Shchukin, D.; Yasakau, K.; Möhwald, H.; Ferreira, M. Anticorrosion coatings with self-healing effect based on nanocontainers impregnated with corrosion inhibitor. *Chem. Mater.* **2007**, *19*, 402–411. [CrossRef]
18. Plyushch, A.; Macutkevicius, J.; Banys, J.; Kuzhir, P.; Kalanda, N.; Petrov, A.; Silvestre, C.; Uimin, M.A.; Yermakov, A.Y.; Shenderova, O. Carbon-coated nickel nanoparticles: Effect on the magnetic and electric properties of composite materials. *Coatings* **2018**, *8*, 165. [CrossRef]
19. Ausanio, G.; Hison, C.L.; Iannotti, V.; Lanotte, L.; Lanotte, L. Magneto-piezoresistance in elastomagnetic composites. *J. Appl. Phys.* **2011**, *110*, 063903. [CrossRef]
20. Dumitrescu, M.; Lisa Iordan, A.R.; Tudorache, F.; Petrila, I.; Borhana, A.I.; Palamaru, M.N.; Mihailescu, C.; Leontie, L.; Munteanu, C. Ni ferrite highly organized as humidity sensors. *Mater. Chem. Phys.* **2015**, *156*, 170–179. [CrossRef]
21. Mohr, R.; Kratz, K.; Weigel, T.; Lucka-Gabor, M.; Moneke, M.; Lendlein, A. Initiation of shape-memory effect by inductive heating of magnetic nanoparticles in thermoplastic polymers. *Proc. Nat. Acad. Sci. USA* **2006**, *103*, 3540–3545. [CrossRef]
22. Schmidt, A.M. Electromagnetic activation of shape memory polymer networks containing magnetic nanoparticles. *Macromol. Rapid Commun.* **2006**, *27*, 1168–1172. [CrossRef]
23. Baljinder, K.; Forkan, S.; Piyanuch, L.; Myler, P. Thermal protection of carbon fiber-reinforced composites by ceramic particles. *Coatings* **2016**, *6*, 22. [CrossRef]
24. Rocha-Santos, T.A. Sensors and biosensors based on magnetic nanoparticles. *TrAC Trends Anal. Chem.* **2014**, *62*, 28–36. [CrossRef]
25. Freitas, P.; Ferreira, R.; Cardoso, S.; Cardoso, F. Magnetoresistive sensors. *J. Phys. Condens. Matter* **2007**, *19*, 165221. [CrossRef]
26. Mocanu, Z.; Airimioaei, M.; Ciomaga, C.; Curecheriu, L.; Tudorache, F.; Tascu, S.; Iordan, A.; Palamaru, N.; Mitoseriu, L. Investigation of the functional properties of Mg_xNi_{1-x}Fe₂O₄ ceramics. *J. Mater. Sci.* **2014**, *49*, 3276–3286. [CrossRef]
27. Pankhurst, Q.A.; Connolly, J.; Jones, S.; Dobson, J. Applications of magnetic nanoparticles in biomedicine. *J. Phys. D Appl. Phys.* **2003**, *36*, R167. [CrossRef]
28. Berry, C.C.; Curtis, A.S. Functionalisation of magnetic nanoparticles for applications in biomedicine. *J. Phys. D Appl. Phys.* **2003**, *36*, R198. [CrossRef]

29. Liu, X.; Li, B.; Geng, D.; Cui, W.; Yang, F.; Xie, Z.; Kang, D.; Zhang, Z. (Fe, Ni)/C nanocapsules for electromagnetic-wave-absorber in the whole Ku-band. *Carbon* **2009**, *47*, 470–474. [CrossRef]
30. Wu, N.; Liu, X.; Zhao, C.; Cui, C.; Xia, A. Effects of particle size on the magnetic and microwave absorption properties of carbon-coated nickel nanocapsules. *J. Alloys Compd.* **2016**, *656*, 628–634. [CrossRef]
31. Li, Y.; Wang, J.; Liu, R.; Zhao, X.; Wang, X.; Zhang, X.; Qin, G. Dependence of gigahertz microwave absorption on the mass fraction of Co@C nanocapsules in composite. *J. Alloys Compd.* **2017**, *724*, 1023–1029. [CrossRef]
32. TECNARO—The Biopolymer Company. Available online: <https://www.tecnaro.de/en/> (accessed on 20 August 2020).
33. Nedelcu, D.; Marguta, A.; Mazurchevici, S.; Munteanu, C.; Istrate, B. Micro-structural and morphological analyses of coated 'liquid wood' samples by ceramic particles. *Mater. Res. Express* **2019**, *6*, 085326. [CrossRef]
34. Mazurchevici, S.-N.; Mazurchevici, A.-D.; Nedelcu, D. Dynamical mechanical and thermal analyses of biodegradable raw materials for additive manufacturing. *Materials* **2020**, *13*, 1819. [CrossRef] [PubMed]
35. Mazurchevici, S.-N.; Motaş, J.G.; Diaconu, M.; Lisa, G.; Lohan, N.M.; Glod, M.; Nedelcu, D. Nanocomposite biopolymer arboblend V2 nature AgNPs. *Polymers* **2021**, *13*, 2932. [CrossRef]
36. Broitman, E.; Nedelcu, D.; Mazurchevici, S.; Glenat, H.; Grillo, S. Tribological and nanomechanical behavior of liquid wood. *J. Tribol.* **2019**, *141*, 022001. [CrossRef]
37. Nedelcu, D.; Santo, L.; Santo, A.G.; Plavanescu Mazurchevici, S. Mechanical behaviour evaluation of arboform material samples by bending deflection test. *Mater. Plast.* **2015**, *52*, 423–426.
38. Oerlikon Metco—Materials and Surface Solutions. Available online: <https://www.oerlikon.com/metco/en/> (accessed on 12 June 2020).
39. Wagner, M. Thermal analysis in practice, fundamental aspects. In *Thermal Analysis in Practice*; Wagner, M., Ed.; Hanser: München, Germany, 2018; pp. 1–9. ISBN 9781569906439.
40. Brebu, M.; Vasile, C. Thermal degradation of lignin—A review. *Cell Chem. Technol.* **2010**, *44*, 353–363.
41. Cai, Y.H.; Xie, Y.C.; Tang, Y.; Zhao, L.S. Thermal decomposition kinetics of Poly(L-lactic acid) after heat treatment. *Open Mater. Sci. J.* **2015**, *9*, 28–32. [CrossRef]
42. Mofokeng, J.P.; Luyt, A.S.; Tabi, T.; Kovacs, J. Comparison of injection moulded, natural fibre-reinforced composites with PP and PLA as matrices. *J. Thermoplast. Compos. Mater.* **2011**, *25*, 927–948. [CrossRef]
43. Prieur, B.; Meub, M.; Wittemann, M.; Klein, R.; Bellayer, S.; Fontaine, G.; Bourbigot, S. Phosphorylation of lignin: Characterization and investigation of the thermal decomposition. *RSC Adv.* **2017**, *7*, 16866–16877. [CrossRef]
44. Chien, Y.C.; Liang, C.; Liu, S.H.; Yang, S.H. Combustion kinetics and emission characteristics of polycyclic aromatic hydrocarbons from polylactic acid combustion. *J. Air Waste Manag. Assoc.* **2012**, *60*, 849–855. [CrossRef] [PubMed]
45. Sameni, J.; Krigstin, S.; Rosa, D.d.S.; Leao, A.; Sain, M. Thermal characteristics of lignin residue from industrial processes. *BioResources* **2014**, *9*, 725–737. [CrossRef]
46. Istrate, B.; Rau, J.V.; Munteanu, C.; Antoniac, I.V.; Saceleanu, S. Properties and in vitro assessment of ZrO₂-based coatings obtained by atmospheric plasma jet spraying on biodegradable Mg-Ca and Mg-Ca-Zr alloys. *Ceram. Int.* **2020**, *46*, 15897–15906. [CrossRef]
47. Fatemeh, T.; Alireza, S.; Hossein, M. Synthesis of Cr₂O₃/TiO₂ nanocomposite and its application as the blocking layer in solar cells. *J. Environ. Anal. Chem.* **2018**, *5*, 1000231. [CrossRef]
48. Bhagyashri, K.; Mahesh, N.; Garadkar, K.M.; Rahul, B.M.; Kiran Kumar, K.S.; Balu, D.A.; Shivaji, T. Ionic liquid assisted synthesis of chromium oxide (Cr₂O₃) nanoparticles and their application in glucose sensing. *J. Mater. Sci. Mater. Electron.* **2019**, *30*, 13984–13993. [CrossRef]
49. Sone, B.T.; Manikandan, E.; Gurib-Fakim, A.; Maaza, M. Single-phase α-Cr₂O₃ nanoparticles' green synthesis using Callistemon viminalis' red flower extract. *Green Chem. Lett. Rev.* **2016**, *9*, 85–90. [CrossRef]
50. Benwood, C.; Anstey, A.; Andrzejewski, J.; Misra, M.; Mohanty, A.K. Improving the impact strength and heat resistance of 3d printed models: Structure, property, and processing correlations during fused deposition modeling (FDM) of Poly(Lactic Acid). *ACS Omega* **2018**, *3*, 4400–4411. [CrossRef]
51. Teixeira, E.d.M.; Campos, A.d.; Marconcini, J.M.; Bondancia, T.J.; Wood, D.; Klamczynski, A.; Mattosoa, L.H.C.; Glenn, G.M. Starch/fiber/poly(lactic acid) foam and compressed foam composites. *RSC Adv.* **2014**, *4*, 6616–6623. [CrossRef]
52. Wu, C.-S. Analysis of mechanical, thermal, and morphological behavior of polycaprolactone/wood flour blends. *J. Appl. Polym. Sci.* **2004**, *94*, 1000–1006. [CrossRef]
53. Onkar, M.; Savita, R. Monoclinic zirconium oxide nanostructures having tunable band gap synthesized under extremely non-equilibrium plasma conditions. *Proceedings* **2019**, *3*, 10. [CrossRef]
54. Sagadevan, S.; Jiban, P.; Isha, D. Hydrothermal synthesis of zirconium oxide nanoparticles and its characterization. *J. Mater. Sci. Mater. Electron.* **2016**, *27*, 5622–5627. [CrossRef]
55. Suning, L.; Qian, W.; Tao, C.; Zhihua, Z.; Ying, W.; Jiajun, F. Study on cerium-doped nano-TiO₂ coatings for corrosion protection of 316 L stainless steel. *Nanoscale Res. Lett.* **2012**, *7*, 227. [CrossRef]
56. Vorrada, L.; Natnapin, J.; Thirawich, C.; Achanai, B. The photocatalytic reduction of hexavalent chromium by controllable mesoporous anatase TiO₂ nanoparticles. *Adv. Mater. Sci. Eng.* **2014**, *2014*, 348427. [CrossRef]
57. Tamrakar, R.K.; Upadhyay, K.; Bisen, D.P. Gamma ray induced thermoluminescence studies of yttrium (III) oxide nanopowders doped with gadolinium. *J. Radiat. Res. Appl. Sci.* **2014**, *7*, 526–531. [CrossRef]

58. Gupta, A.K.; Mohanty, S.; Nayak, S.K. Preparation and characterization of lignin nanofibre by electrospinning technique. *Int. J. Sci. Eng. Appl. Sci.* **2015**, *1*, 184–190, ISSN:2395-3470.
59. Adnan, A.; Shahid, A.; Murtaza, S.; Shahid, M.R.; Shahzad, N.; Saadat, A.S. Structural and magnetic phase transition of sol-gel-synthesized Cr₂O₃ and MnCr₂O₄ nanoparticles. *J. Sol-Gel Sci. Technol.* **2016**, *80*, 96–102. [[CrossRef](#)]
60. Ferreira, C.S.; Santos, P.L.; Bonacin, J.A.; Passos, R.R.; Aparecido Pocrifka, L. Rice husk reuse in the preparation of SnO₂/SiO₂ nanocomposite. *Mater. Res.* **2015**, *18*, 639–643. [[CrossRef](#)]
61. Nedelcu, D.; Comaneci, R. Microstructure, mechanical properties and technology of samples obtained by injection from arboblend. *Indian J. Eng. Mater. Sci.* **2014**, *21*, 272–276.



Acoustic Performance of Some Lined Dissipative Silencers

Marcelin Benchea , Carmen Bujoreanu , and Gelu Ianus

Mechanical Engineering Faculty, Mechatronics and Robotics Department, “Gheorghe Asachi”
Technical University of Iași, 43 Prof. Dr. Doc. D. Mangeron, 700050 Iași, Romania
{marcelin.benchea, cbujorea}@tuiasi.ro

Abstract. Heating ventilating and air-conditioning systems which equip our buildings/rooms represent noise sources unfavorable affecting the people decent living and working conditions. Usually, silencers are used to reduce the annoying sound from these systems. They are lined with different materials and they have various geometries in order to satisfy the consumer needs, in terms of acoustic comfort. Sound absorption and sound transmission loss characterize the materials acoustic properties, but it is not mandatory that a good absorbent material to be also an efficient one from transmission loss (attenuation) point of view. Our paper is focused on an acoustic study of different materials lining three commercial silencers of same geometry and size. We have recorded the sound data according to standards: ISO 10534-1:1998 for the sound absorption coefficient and ISO 7235:2009 for the transmission loss rating. Third octave analysis with LabView soft is used to process the sound information and then the two parameters values are calculated. The acoustic characteristics of the tested materials are discussed and features that recommend them to be used as lining materials for silencers are highlighted.

Keywords: Dissipative silencer · Sound absorption · Sound transmission loss

1 Introduction

The continuum industrial development promotes more and more powerful equipments, but their benefits are also accompanied by issues related to the human comfort. It's about the environmental pollution under all its forms: NO_x, thermal, acoustic. Acoustic protection is strong linked to the sound absorption concept which quantifies the energy dissipated within the material and the transmission through it. The sound reaching the material releases an energy which can be absorbed and reflected, in relation to the material sound absorption performance. The materials acoustic behaviors are very different, depending on the configurations in which they are included and also, on the material properties [1–4].

Comfort is required in our buildings/rooms and heating ventilating and air-conditioning (HVAC) systems are important equipments for that, ensuring the proper conditions for the air quality and temperature. On the other hand, they constitute noise

sources affecting not only the people comfort, but also the human health. To reduce this noise, it is usually used a silencer. Common silencers are in-duct installed on the intake and/or discharge side of the air handler. Also, they can be located on the receiver side of other noise generators (terminal boxes, valves, dampers). Literature describes the silencers types used in the sound attenuation as: reactive, active and dissipative [5]. Dissipative silencers are recommended to attenuate broadband noise [6]. Plenum boxes are dissipative ones, most widely used in ducts realizing minimal pressure drop along the silencer. They are available in various shapes and geometries according to the duct design and commonly lined with different materials in order to realize the sound attenuation. These materials are usually porous. The sound absorption performances are predicted through theoretical approaches which lead to the materials structural design from this point of view [7, 8]. The sound absorption/transmission theory is often modeled by Johnson-Champoux-Allard (JCA) approach which calculates the sound absorption coefficient taking into account of some material physical parameters such as flow resistivity, open porosity, tortuosity, and the viscous/thermal characteristic lengths [9]. Another approaches, such as Johnson-Champoux-Allard-Lafarge model and Johnson-Champoux-Allard-Pride-Lafarge modify the JCA model, introducing more parameters difficult to be analytical calculated [10]. Therefore, the theoretical models are not sufficient to predict the materials acoustic performances and the experimental investigations are needed to complete their accuracy. Our paper focuses on the acoustic performances, experimental determined, of some different lined plenum boxes in terms of sound absorption and transmission loss. These two parameters must be corroborated in order to obtain an optimized acoustic behavior, beneficial for people comfort and health.

2 Theoretical Considerations

The absorption coefficient of a material is linked to the sound frequency and also depends on the angle at which the sound wave reaches the material. Figure 1 depicts the sound wave behavior according to the energy conservation:

$$E_i = E_r + E_e \quad (1)$$

The energy E_e represents the sum of the transmitted and absorbed sound energy of the tested material.

The absorption coefficient, α , is classical defined as the ratio of all energy not reflected to incident energy [11]:

$$\alpha = 1 - \frac{E_r}{E_i} \quad (2)$$

Absorption coefficient values are settled using various standardized methods. Measurements can be made in a reverberant room, according to the ISO 354:2003 standard. Another method uses the standing wave tube technique (ISO 10534-1:1998 standard) and the impedance tube method (ISO 10534-2:1998 standard). The last method is often mentioned as the transfer-function method.

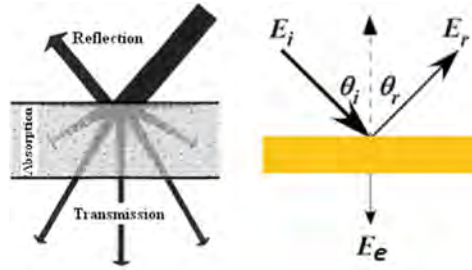


Fig. 1. Sound energy conservation [12].

ISO 354:2003 standard promotes a methodology to evaluate the reverberation time delay in diffuse sound field (reverberation room) for a tested sample placed in this room. The standard refers to the Sabine absorption coefficient.

Sabine equation is used to extract the Sabine absorption coefficient, α_{sab} .

$$\alpha_{sab} = 0.9210 \frac{V}{cS} (d_2 - d_1) + \alpha_1 \tag{3}$$

V is the room volume; c is the sound speed; S is the sample surface area; α_1 is the absorption coefficient of covered surface; d_1 and d_2 are sound decay rates (dB/s) with and without the sample. Applying this standard leads to some measurement inaccuracies, reported by literature, due to the sample room location influence and also due to its edge effects [7, 13].

ISO 10534:1998 standard presents two methods for the sound absorption coefficient determination in a normal incident sound field [14].

The standard first part describes the method for calculating the peak to minimum amplitude ratio in a standing wave tube. Thus, it is determined the magnitude and phase of the pressure reflection coefficient, and then the sound absorption coefficient α .

$$\alpha = \frac{I_1}{I_2} = \frac{|p_i|^2 - |p_r|^2}{|p_i|^2} = 1 - \left(\frac{n-1}{n+1} \right)^2 \text{ where } n = \frac{p_{max}}{p_{min}} \tag{4}$$

where I_1 and I_2 are the intensities of incident and reflected waves, respectively; p_i and p_r are the sound pressures of incident and reflected waves, respectively; n is the standing wave ratio; p_{max} and p_{min} are the maximum and minimum values of the sound pressure, respectively.

The second part of the standard uses the transfer function H concept, between two spaced microphones, and also spaced from sample. The method considers that the sound reflection coefficient, r , can be evaluated from the measured transfer function H between the two microphones. So, the pressure reflection coefficient r , then the sound absorption coefficient α , are obtained.

$$H = \frac{p_1}{p_2} \text{ and } r = |r|e^{j\varphi_r} = r_r + jr_i = \frac{H - e^{-jks}}{e^{jks} + H} e^{-j2k(l+s)}, \alpha = 1 - r^2 \tag{5}$$

p_1 and p_2 are the sound pressure measured by the microphones positioned behind the sample in the tube; r_r is the real component; r_i is the imaginary component; φ_r is the

phase angle of the normal incidence reflection coefficient; k is the wave number; l is the distance from the sample to the first microphone; s is the distance between the microphones.

To facilitate the comparison between materials, usually a single number is chosen to evaluate the sound absorption coefficients of each material [15]. Therefore, an indicator has been introduced, Noise Reduction Coefficient (NRC), with the value equal to the arithmetic average of the sound absorption coefficients related to frequency.

Another important parameter to characterize the silencers acoustic performance is represented by the sound transmission loss Tl . This evaluates the attenuation of the sound power level in the duct behind the silencer (as test object). It can be expressed as [16]:

$$Tl = SWL_I - SWL_{II} \text{ [dB]} \quad (6)$$

where: SWL_I - the sound power level in certain frequency band, with in-duct silencer; SWL_{II} - the sound power level in the same frequency band, without in-duct mounted silencer. The transmission loss Tl is usually measured using sound pressure levels at identical points or paths [16].

Sound absorption coefficient together with sound transmission loss values provide more complete indications of the system's performance regarding the noise sources.

3 Experimental Methodology

3.1 Method

Our method for sound absorption coefficient evaluation follows ISO 10534-1:1998 standard. We have used the acoustic interferometer technique, taking into account that in the impedance tube the sound waves are reflected from the sample, and then received by a microphone movable along the tube. So, it can be measured and recorded the incident and reflecting sound pressure. Our experimental work was conducted in an anechoic room, but it uses a modified impedance tube [2] adapted to our work space. This means that the anechoic termination of the modified impedance tube is the anechoic room itself. The whole procedure and explanations are detailed in [12, 15].

As result, the real absorption coefficient determined in the modified tube has lower values than those obtained by standard measurements (with rigid support at the end of the tube) [15].

Brief, in order to realize these measurements, our experimental setup includes a special sound-source equipment (consists of a white noise generator B&K, an amplifier and a broad band loudspeaker), impedance duct, special receiving-sound equipment including a movable microphone B&K and a soundmeter B&K connected with the microphone and NIDAQ board, data acquisition board type-NIDAQPad and laptop with LabVIEW soft.

On the other hand, the transmission loss measurements were realized according to the procedure from ISO 7235:2009, which describes, among others, the methods for determining the transmission loss, in frequency bands, of ducted silencers with and without airflow [16].

Ranging different airflows is supplied by a centrifugal fan (0 V ÷ 10 V with 1 V ratio) over which it overlaps white noise coming from the sound-source equipment. In this case the experimental setup is modified and additionally contains the above mentioned centrifugal fan, device for the flow rate (flow meter), device for the pressure drop (pressure meter), test object (the dissipative silencers); transition elements on either side of the test object. The procedure is detailed in [17].

Third-octave band analyses of recorded sound data collected, according to the above procedures (ISO 10534-1:1998 and ISO 7235:2009), were performed. The next step is to use relations (4) and (6) to calculate the sound absorption coefficient and the transmission loss (attenuation) values, respectively.

3.2 Test Samples

We have tested, from absorption point of view, three materials types lining some commercial plenum boxes.

They are denoted with “green” (glass based), “blue” (mineral based), “black” (nylon based). The lining materials thickness and porosity are the same, as specified by the manufacturer. Then we have tested, from transmission loss point of view, the three plenum boxes. They have the same width, height and length, with $\Phi 100$ mm inlet/outlet diameter for in-duct placement.

Figures 2, 3 and 4 present both the experimental stands, adapted for the anechoic room and according to standards.



Fig. 2. Sound absorption coefficient experimental setup (according to ISO 10534-1:1998).

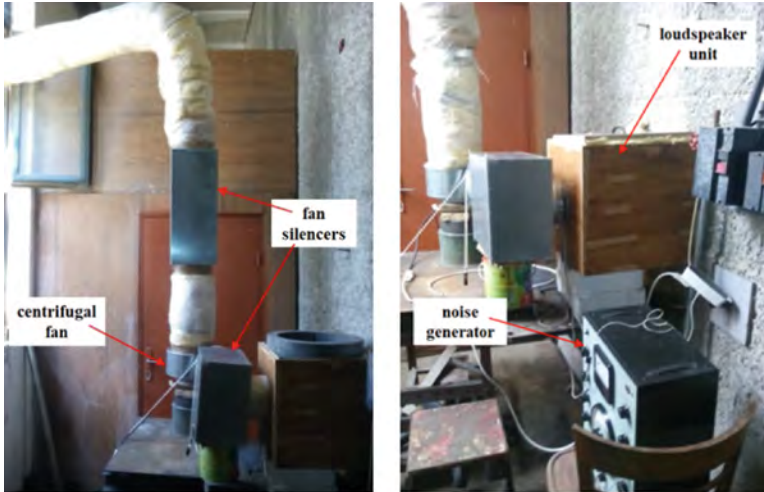


Fig. 3. Transmission loss experimental setup (outside the anechoic room).

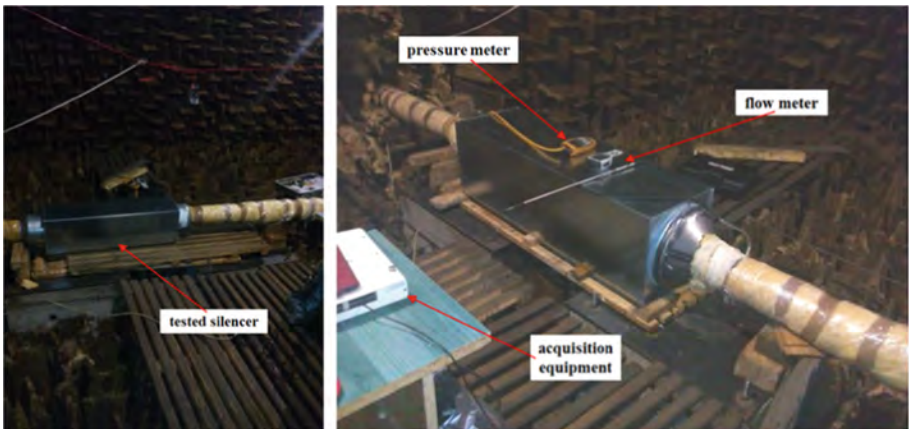


Fig. 4. Transmission loss experimental setup (inside the anechoic room).

4 Results and Discussion

As we have above explained, first, we present the sound absorption coefficients values for the three materials lining three commercial plenum boxes (Fig. 5).

An obvious increasing tendency of the absorption coefficient can be observed at frequencies higher than 1450 Hz (Fig. 5), values over 0.6 and greater for the green lining. For frequencies lower than 1450 Hz the absorption coefficient presents values under 0.6 and higher for the blue lining. Using the average absorption coefficient (NRC) concept, as absorption performance indicator, the following values were obtained: 0.50 for the green lining, 0.56 for the blue lining and 0.44 for the black lining. Obvious, the blue lining can be considered the better sound absorbent material.

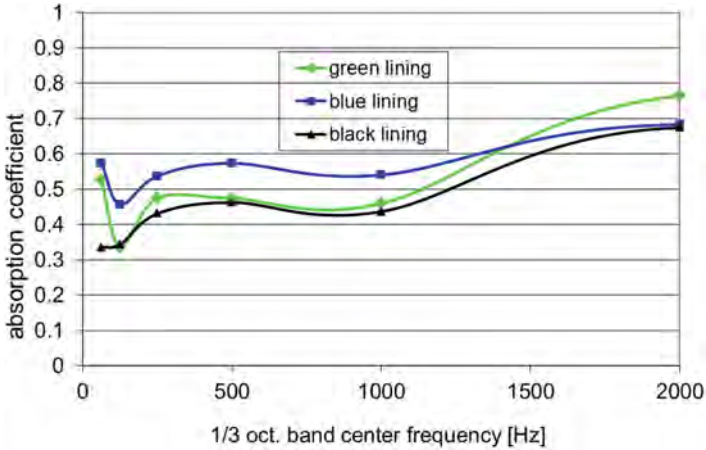


Fig. 5. Sound absorption coefficients for materials lining commercial plenum boxes.

Figures 6, 7 and 8 present the sound attenuation (transmission loss) values, recorded on the plenum boxes and then calculated, as we have above described in paragraph 2. The figures are selected for variable airflow provided by the centrifugal fan (a supply of 3 V, 7 V, 10 V). They show that the attenuation of the silencers is also influenced by the airflow in the HVAC systems, supplied by the centrifugal fan. It is observed an increasing tendency for frequencies higher than 500 Hz, with values lower than 40 dB for small airflows and maximum 15 dB for higher airflows. For small airflows, over 1450 Hz in frequencies domain of interest, the green lining has a greater attenuation compared to the others materials.

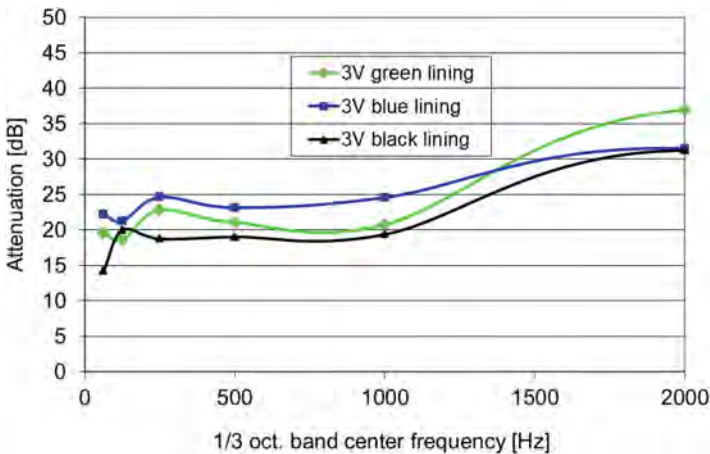


Fig. 6. Attenuation versus frequency for low airflow.

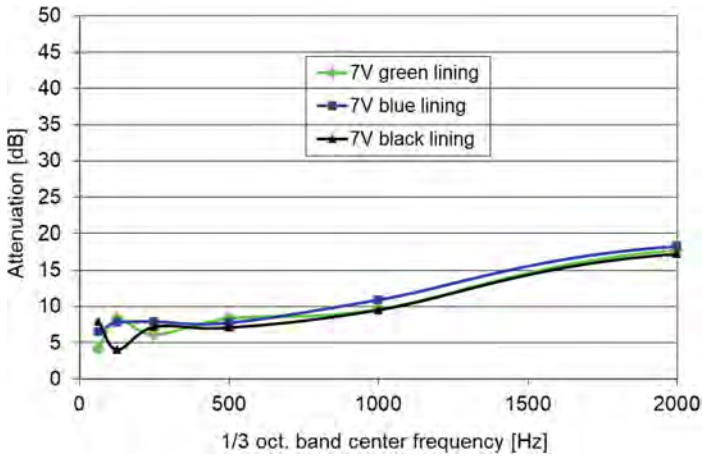


Fig. 7. Attenuation versus frequency for medium airflow.

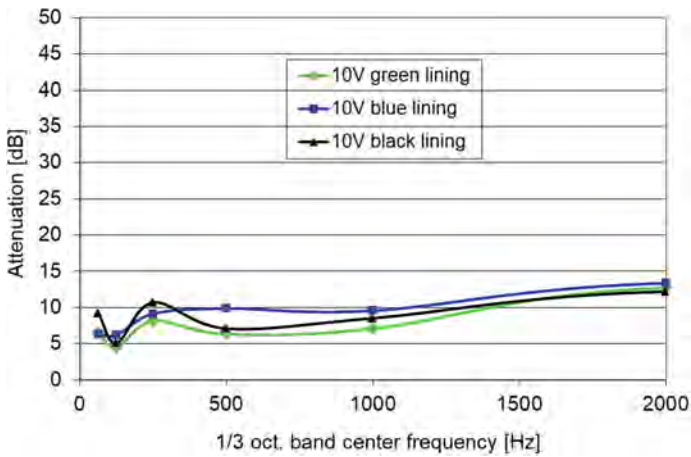


Fig. 8. Attenuation versus frequency for high airflow.

However, in the explored third octave band, at different airflows from low to high values provided by the centrifugal fan, the blue lining presents the best attenuation despite the fact that the silencer lined with this material creates a greater pressure drop in the duct's airflow path, as Fig. 9 depicts.

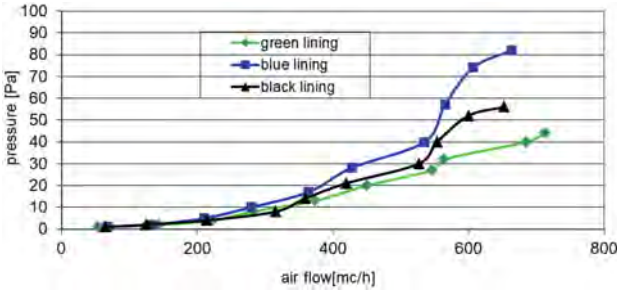


Fig. 9. Pressure versus airflow.

5 Conclusions

Materials acoustic properties are linked to their sound absorption and transmission loss characteristics. The blue lining material presents better acoustic properties under 1450 Hz frequencies according to the absorption coefficient evolution and average value, also, according to attenuation evolution. The attenuation has higher values as the air flow through the silencer is lower, because the dynamic flow of air negatively influences the noise.

The main conclusion is that the acoustical architecture takes into account of both concepts. Sound absorption, usually represented by NRC (ranging from 0 to 1), is expressed by the sound dissipation inside the material. Sound transmission loss (attenuation) is related to the sound insulation, therefore it is expressed by the reflecting sound energy. It is obvious that there is difficult to select a material and also, it's mounting system, to realize absorption and insulation at the same time.

References

1. Long, M.: *Architectural Acoustics*, 2nd edn. Academic Press, Cambridge (2014)
2. Leping, F.: Modified impedance tube measurements and energy dissipation inside absorptive materials. *Appl. Acoust.* **74**, 1480–1485 (2013)
3. Istvan, L.V., Beranek, L.L.: *Noise and Vibration Control Engineering: Principles and Applications*, 2nd edn. Wiley, Hoboken (2005)
4. Shen, C., Xin, F.X., Lu, T.J.: Theoretical model for sound transmission through finite sandwich structures with corrugated core. *Int. J. Non-Linear Mech.* **47**(10), 1066–1072 (2012)
5. *Handbook Sound and Vibration Control*. American Society of Heating, Refrigerating, and Air Conditioning Engineers 48, USA (2011)
6. Borelli, D., Schenone, C., Pittaluga, I.: Theoretical and numerical modelling of a parallel-baffle rectangular duct. In: *Proceedings of Meetings on Acoustics*, San Diego, vol. 14, p. 040004 (2012)
7. Wijnant, Y.H., Kuipers, E.R., de Boer, Ir.A.: Development and application of a new method for the in-situ measurement of sound absorption. In: *Proceedings of ISMA*, Leuven, Heverlee, pp. 109–122 (2010)
8. Cao, L., Fu, Q., Si, Y., Ding, B., Yu, J.: Porous materials for sound absorption. *Compos. Commun.* **10**, 25–35 (2018)

9. Chevillotte, F., Perrot, C.: Effect of the three-dimensional microstructure on the sound absorption of foams: a parametric study. *J. Acoust. Soc. Am.* **142**, 11–30 (2017)
10. Yang, X.H., Ren, S.W., Wang, W.B., Liu, X., Xin, F.X., Lu, T.J.: A simplistic unit cell model for sound absorption of cellular foams with fully/semi-open cells. *Compos. Sci. Technol.* **118**, 276–283 (2015)
11. Beranek, L.L., Ver, I.L.: *Noise and Vibration Control Engineering: Principles and Applications*. Wiley, Hoboken (1992)
12. Bujoreanu, C., Nedeff, F., Benchea, M., Agop, M.: Experimental and theoretical considerations on sound absorption performance of waste materials including the effect of backing plates. *Appl. Acoust.* **119**, 88–93 (2017)
13. McGroary, M., Castro, C.D., Gaussen, O., Cabrera, D.: Sound absorption coefficient measurement: Re-examining the relationship between impedance tube and reverberant room methods. In: *Proceedings of Acoustics*, Fremantle, Australia, pp. 1–8 (2012)
14. ISO 10534:1998, *Acoustics - Determination of sound absorption coefficient and impedance in impedance tubes: Part 1: Method using standing wave ratio, Part 2: Transfer-function method*
15. Oancea, I., Bujoreanu, C., Budescu, M., Benchea, M., Grădinaru, C.: Considerations on sound absorption coefficient of sustainable concrete with different waste replacements. *J. Clean. Prod.* **203**, 301–312 (2018)
16. ISO 7235: 2009, *Acoustics- Measurement procedures for ducted silencers- Insertion loss, flow noise and total pressure*
17. Bujoreanu, C., Benchea, M.: Experimental investigation of noise characteristics for HVAC silencers. In: *MATEC Web of Conferences*, Iasi, vol. 112, p. 07001 (2017)



An Investigation Regarding the Impact of Running-In on Rolling Contacts Lives

Marcelin Benchea^(✉)  and Spiridon Crețu 

Mechanical Engineering Faculty, Mechatronics and Robotics Department, “Gheorghe Asachi”
Technical University of Iași, 43 Prof. Dr. Doc. D. Mangeron, 700050 Iași, Romania
marcelin.benchea@tuiasi.ro

Abstract. Microtopography of the working surfaces subjected on rolling contact can be realized by various manufacturing technologies (lapping, polishing, turning, grinding, etc.). The aim of this work is to point out the impact of the initial surface asperities on running-in phenomenon, geometry of active surface and rolling contacts durability. At first, the article exhibit the experimental tests carried out by using the two discs AMSLER machine with proper samples for pure rolling motion. The microtopography of the working surfaces have been measured before and after tests. Secondly, a numerical study is presented for the samples used on the two discs AMSLER machine, where the measured topography data and loading conditions are used as input data in the analysis model. The last part of the article exhibit a numerical investigation for the rolling bearing CARB C2318 where the modified rating life have been computed with methodology given by ISO 16281.

Keywords: Surface rugosity · Running-in process · Plastic displacement · Modified rating life

1 Introduction

When the working surfaces of two bodies are loaded for the first time the microtopography of both surfaces generally suffer. The microtopography modifies that occur from starting to stable condition are related with the running-in process [1–3] and affect the contact pressures repartitions, and stress state, especially in the shallow surface layers, and consequently the various wear types involved in the durability of contacting bodies [4–6]. Recently studies on running-in [7–10] show that changes in the surface asperities likewise alter the chemistry of surface, remanent stresses and microstructure close to the active surfaces.

The numerical models used to describe the microtopography changes [11, 12] require the input of a 3D rough surface. Because the experimental acquirement of such data does not grant enough samples of profile to be used, a main necessity for any micronumerical analysis is to produce random rough surfaces with identical or similar characteristics as the effective surfaces [13, 14].

The running-in and steady-state experimental investigation were conducted on two rollers [15] and was observed the evolution of wear depth/weight and surface rugosity during the experiment. It was evidenced that the slope of wear depth and worn weight decreases as the asperities are smoothed and the number of plastically deformed asperities is reduced. In the assessment of rugosity parameters of hardened steel surfaces [16] it was pointed out that in the running-in process the most prominent asperity heights suffer plastic strain through the primary loading period.

The impact of the relative sliding movement on rolling contact fatigue life of surfaces with sinusoidal rugosity in mixed lubrication was investigated in [17] without considering the surface modification due to wear. A model for the rising of rolling contact fatigue (RCF) cracks initiated from the surface in the material of rolling bearings was presented in [18]. In this study the greatest value of the von Mises subsurface stress was considered as the critical stress for the RCF developed in the number of stress cycles which carry, finally, to critical damage.

Recently, in [19] was pointed out that in the running-in process of rolling bearings, the microgeometry of the working surfaces has two major effects: *i*) an increase in the regional clearances due to elastic deflection and, *ii*) the initiation of pressure fluctuations affect the rolling bearing life. Also, in the evaluation of the bearing life was considered the lubricate quality parameter κ as a function of the lubricate parameter λ whichever depends on the film thickness and the surface rugosity. Furthermore, in recent studies [20, 21], to compute the rolling bearing life was used Ioannides and Harris model, taking into account the surface and subsurface stress.

To model the non-linear strain rate under deformation of materials stressed in elastic-plastic field, an analysis model was build [22, 23]. The model is developed in the framework of incremental hypothesis of plasticity using the von Mises plastic flow principle and Prandtl-Reuss equations. Take into account the nonlinear kinematic and isotropic hardening laws of Lemaitre-Chaboche [24, 25] the model considers the cyclic hardening phenomenon.

The microtopography of working surfaces generate sharp peaks in pressure repartitions which disturb the von Mises equivalent stress repartition with a negative influence on fatigue life of rolling contact [26].

2 Material and Methods

2.1 Experiment

Experimental tests on the two discs machine (AMSLER), Fig. 1, have been carried out to evaluate the surface rugosity modification during the running-in process.

The two discs are rolling one versus other with constant rotating velocity rate $k = n_2/n_1 = 0.906$, where n_2 and n_1 are rotating speed of the upper and lower disc respectively.

Two discs with size dimensions of 59 mm and 53.5 mm manufactured from 42 CrMo4 steel were used. The upper disc with size dimension of 59 mm was crowned with radius of 300 mm and the lower disc with size dimension of 53.5 mm was cylindrical. The discs had 10 mm in width and were hardened and tempered resulting a hardness of 425 HB.

Trying conditions: rotating velocity $n_1 = 181$ rpm, normal loading $F = 140$ N, running time 10 min, SAE46 (H46) lubricant, working temperature 25 °C.



Fig. 1. Two discs machine (AMSLER).

2.2 Methods

Rough Surface Simulation. All surfaces have some form of structure microtopography that change according to its textures and the way it have been made. Corresponding to [5] there are three types of parameters for the rugosity contour: magnitude parameters (the normal characteristics of the surface deflections), array parameters (the straight characteristics of the surface deflections) and composite parameters.

Rugosity Amplitude Parameters. The experimental acquirement of the rugosity contours is time overwhelming, so that, the various characters of the rough surfaces have to be established analytically or numerically, in order to study their role upon the evolution of a particular rolling contact. Majority of the statistical properties of a rough surface can be defined from knowledge of two statistical functions, the autocorrelation function and the frequency density function.

The probability function is used to point out the spatial characteristics. Some real surfaces, particularly recently grinded surfaces, expose a height repartition close to the normal Gaussian probability function:

$$p(z) = \frac{\sigma}{\sqrt{2 \cdot \pi}} \cdot \exp\left(\frac{-z^2}{2\sigma^2}\right) \quad (1)$$

where σ is standard deviation (r.m.s.) from the average height.

However if the grinded surface is subsequently polished its rugosity is no longer Gaussian. A mathematical representation of the probability function shape can be achieved by using the central moments, defined as:

$$\mu_k = \int_{-\infty}^{+\infty} z^k \cdot p(z) \cdot dz \quad (2)$$

or in discrete form:

$$\mu_k = \frac{1}{n} \cdot \sum_{i=1}^n z_i^k \quad (3)$$

Any spatial rugosity parameter presented in the specialized literature can be mathematically established utilizing the first four moments. However, because the first moment equals to zero the arithmetic mean rugosity R_a is defined instead:

$$R_a = \frac{1}{n} \cdot \sum_{i=1}^n |z_i| \tag{4}$$

The second moment is the rugosity peaks variance, signifying the root mean square R_q (r.m.s.), or the standard deviation σ , of the surface peaks:

$$R_q = \sigma = \sqrt{\mu_2} \tag{5}$$

The relation from σ and R_a rely, to certain measure, on the surface nature; for a regularly sinusoidal contour $\sigma = \pi/(2 \cdot 2^{1/2}) \cdot R_a \approx 1.11 \cdot R_a$, and for a Gaussian contour $\sigma = (\pi/2)^{1/2} \cdot R_a \approx 1.25 \cdot R_a$.

Rugosity Spectral Characterization. The Autocorrelation Function (ACF). The ACF, $R(x, y)$ is the supposed valuables of the multiplication: $z(x, y) \cdot z(x + \lambda_x, y + \lambda_y)$ of the surface peak at point (x, y) and at the point $(x + \lambda_x, y + \lambda_y)$, and λ_x, λ_y are the delay lengths. Under the stationarity assumption this expectation is independent:

$$R(\lambda_x, \lambda_y) = E\{z(x, y) \cdot z(x + \lambda_x, y + \lambda_y)\}, R(0, 0) = \sigma^2. \tag{6}$$

For majority of the fabrication processes the ACF attend a negative exponential function. In this presumption the required parameters to provide an ACF are the dissolution length in two directions that are normal one to other. These lengths are well-known as the autocorrelation lengths λ_x, λ_y , and are fully described as the length in the x and y directions where the autocorrelation length falls to 10% from its initial value.

Archard and Whitehouse considered the shape of an arbitrary surface as an arbitrary signal depicted by a peak distribution and an ACF and revealed that all characteristics of a surface with Gaussian dispersion of peaks and a negative exponential ACF can be depicted by two parameters: σ and λ [27].

Gaussian Surfaces with a Prescribed ACF. A numerical method has been developed to generate a random 3D rough surface, [14]. The surface rugosity peaks were generated corresponding to the next equation:

$$z_{ij} = \sum_{k=1}^n \sum_{l=1}^m \alpha_{kl} \cdot \eta_{i+k, j+l} \tag{7}$$

where α_{kl} are parameters that give the ACF needed and $\eta_{i+k, j+l}$ are individual arbitrarily values that have the variance unit, [13, 14], the following equations are valid:

$$E(\eta_{ij}\eta_{kl}) = \begin{cases} 1 & \text{if } i = k, j = 1 \\ 0 & \text{if } i \neq k, j \neq 1 \end{cases} \tag{8}$$

Using Eqs. (8) the ACF is obtained as:

$$R_{pq} = \sum_{k=1}^{n-p} \sum_{l=1}^{m-q} \alpha_{kl} \cdot \alpha_{k+p, l+q} \quad \begin{matrix} p = 0, 1, 2, \dots, n-1 \\ q = 0, 1, 2, \dots, m-1 \end{matrix} \tag{9}$$

Equations (9) it is a non-linear system with the unknowns parameters α_{kl} , [13]. An iterative method has been applied to resolve the non-linear system (9) and its solutions were introduced in Eq. (7) to achieve the rugosity peaks with the prescribed *ACF*.

For two coarse surfaces considered in contact an equivalent surface [28] can be defined by adding corresponding values of the rugosity heights:

$$z = z_1 + z_2 \tag{10}$$

Elastic-Plastic Model. An elastic-plastic analytical model has been made to estimate the plastic displacement of the surfaces in rolling contact, that take into account the material cyclical strengthening particularity as depicted by a nonlinear kinematic and an isotropic strengthening law [24, 25]. The plastic flow surface is depicted by the von Mises plastic flow principle:

$$F = f(\sigma - \alpha) - \sigma_Y^0 = 0 \tag{11}$$

where σ_Y^0 is the plastic flow stress and $f(\sigma - \alpha)$ is the von Mises equivalent stress.

The isotropic strengthening part of the model describes the yielding stresses σ_{Y0} as a relationship of the equivalent plastic deformation ε^p :

$$\sigma_Y^0 = \sigma_{Y0} + Q_\infty \cdot \left(1 - e^{-b_\infty \cdot \bar{\varepsilon}^p}\right) \tag{12}$$

where Q_∞ is the limit modifies in the plastic flow surface dimension on the deviatoric level and b_∞ present how fast the limit dimension is achieved [29].

The Ramberg-Osgood’s equation has been applied to consider the connection between the strain tensor intensity ε_e and the stress tensor intensity σ_e :

$$\bar{\varepsilon}_e = \frac{\bar{\sigma}_e}{E} + \left(\frac{\bar{\sigma}_e}{B}\right)^N \tag{13}$$

where N is the plastic strengthening index and B is the plastic strengthening parameter [22].

The surfaces plastic displacement w^p was computed by the plastic deformations ε^p gathered in the subsurface stratum:

$$w^p(x, y) = \int_0^z \varepsilon^p(x, y, z) \cdot dz \tag{14}$$

3 Experimental vs. Numerical Results and Discussion

3.1 Experimental Results

The rugosity contours for two discs studied on AMSLER machine are depicted in Fig. 2, before and after the running-in experiment. The original discs rugosity were $R_{q1} = 610$ nm and $R_{q2} = 280$ nm, respectively $R_{a1} = 460$ nm and $R_{a2} = 220$ nm.

The evaluation of discs rugosity before and after experiments revealed modifications for the bottom disc, with a coarser rugosity, for the estimate length of l mm in the middle. After the running-in experiment the root mean square of the bottom disc decreases to $R_{q1} = 550$ nm and the arithmetic mean rugosity peaks to $R_{a1} = 390$ nm.

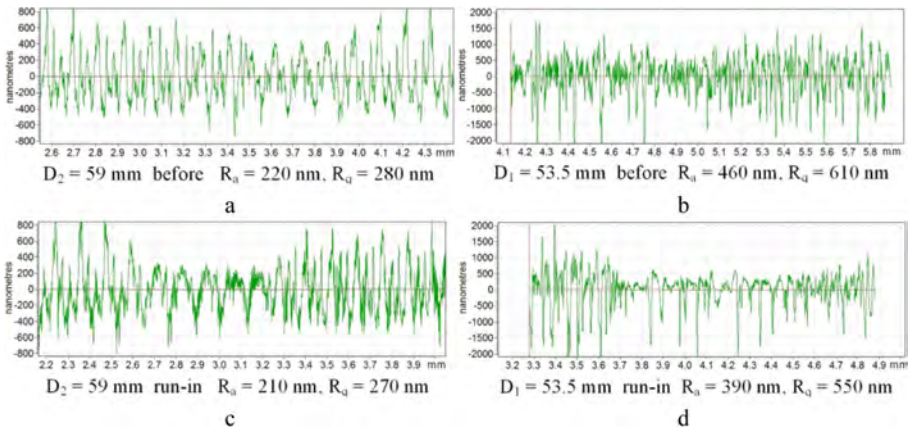


Fig. 2. 2D rugosity contours before and after running-in experiment.

3.2 Experimental vs. Numerical Results Provided by Elastic-Plastic Model

The plastic changes of the surface rugosity are due to the raised peaks in the pressure repartition on the two discs contact area, Fig. 4. These pressure peaks can induce a state stress above the plastic flow limit resulting plastic displacement of the rugosity peaks.

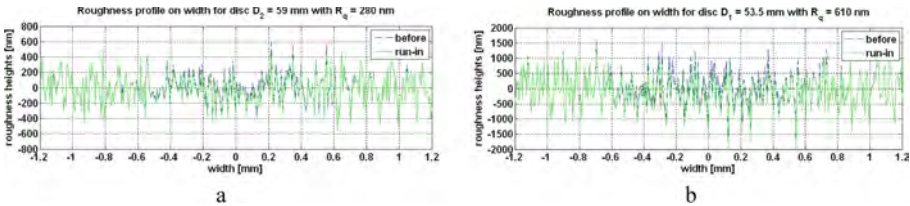


Fig. 3. 2D rugosity contours ahead and further 300 run-in cycles (numerical).

The elastic-plastic running-in model presented in [1, 2] provided numerical results in good agreement with those obtained experimentally. In Fig. 3 are comparatively exemplified the experimental and numerical results obtained after 300 running cycles.

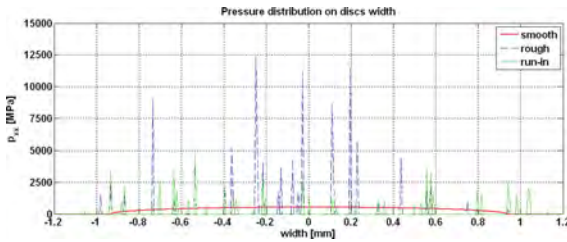


Fig. 4. Pressure distribution on discs width (hypothetic full elastic range).

3.3 Rolling Bearing Application. Numerical Results

The CARB C2318 rolling bearing has been considered for the numerical investigation. The geometry of rolling bearing, Fig. 5a, is depicted by the following parameters: the diameter of outer ring $d_{ce} = 165$ mm, the diameter of inner ring $d_{ci} = 115$ mm, the diameter of roller $d_w = 25$ mm, the length of roller $L_w = 54$ mm, roller crown radius $R_1 = 7000$ mm, inner/outer ring crown radius $R_2 = 7210$ mm, rollers number $Z = 14$, [30]. The measured roughness for rollers, inner and outer raceways are presented in Fig. 5b.

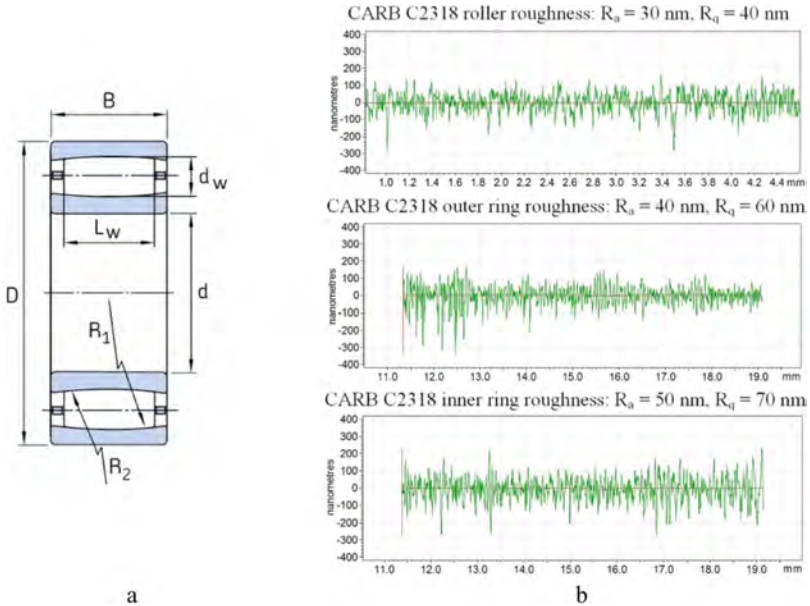


Fig. 5. (a) Toroidal roller bearing geometry [30] and (b) Rugosity of bearing elements.

A moderate radial charging $F_R = .185 \cdot C = 112.5$ kN has been considered in the numerical investigation of the running-in process. Three sizes of the surface rugosity characteristics have been chosen: *i*) a small rugosity with $R_{qw1} = 40$ nm for roller surface and $R_{qi1} = 70$ nm for the raceway surface of the inner ring, like the surface rugosity characteristics determined on Taylor Hobson equipment, Fig. 5b; *ii*) a moderate rugosity with $R_{qw2} = 80$ nm and $R_{qi2} = 140$ nm, and *iii*) a coarse rugosity with $R_{qw3} = 120$ nm and $R_{qi3} = 210$ nm.

For the roller bearing steel loaded in the elastic-plastic field the following parameters were used: the plastic flow stress $\sigma_{Y0} = 1650$ MPa, the coefficient of Poisson $\nu = 0.27$, the modulus of Young $E = 203$ GPa, $b_\infty = 120$ that shows how fast the limit dimension is achieved and $Q_\infty = -100$ MPa, the limit modifies in the plastic flow surface dimension on the deviatoric level [28], the plastic strengthening index $N = 12.6$ and the plastic strengthening parameter $B = 4320$ MPa [22, 23].

The 2D rugosity contours of roller/inner ring ahead and further 300 run-in cycles are presented in Fig. 6. It may be remarked so the running-in process is more pronounced for the inner ring and the rugosity peaks are plastic flattened in the middle: a length of 10 mm for $R_{qi1} = 70$ nm, a length of 20 mm for $R_{qi2} = 140$ nm and a length of 40 mm for $R_{qi3} = 210$ nm.

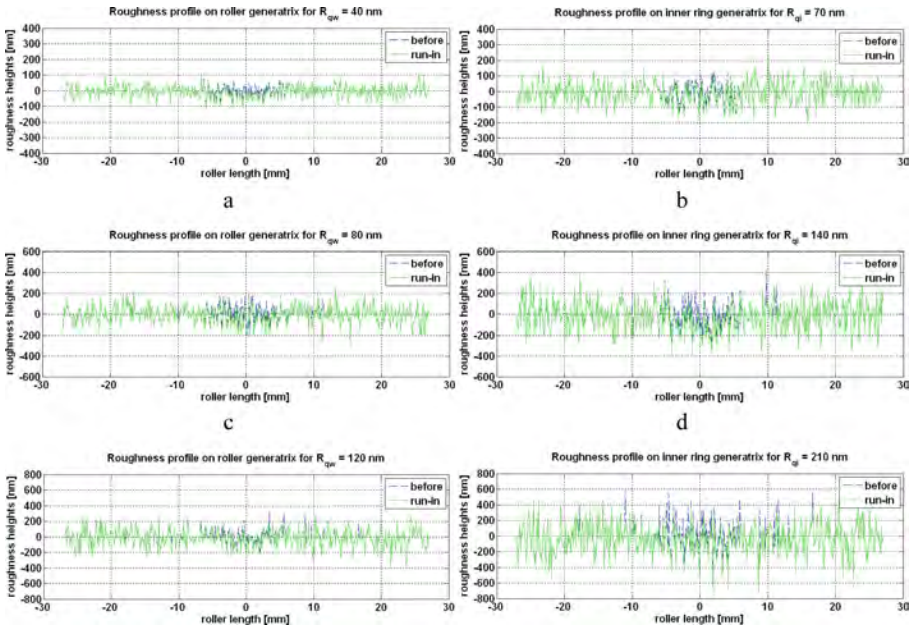


Fig. 6. 2D rugosity contours of roller/inner ring ahead and further 300 run-in cycles.

The higher is the rugosity peaks the larger is the plastic deformation.

The 2D pressures repartitions on roller generatrix for the heavy charged roller/inner ring contact are depicted in Fig. 7. In the center of the contact area the maximum peak pressure for the smooth surface is 2250 MPa. The existence of the rugosity on the working surfaces causes high peaks in pressures repartition. The higher are pressure peaks as the rugosity it is coarser and have the highest magnitude of 2700 MPa for the small rugosity, 3200 MPa for the moderate rugosity and 4000 MPa for the coarse rugosity.

It may be noticed that after 300 run-in cycles the pressure peaks are a little attenuated in the center of the contact area for the small and moderate rugosity and are much attenuated on all contact region for the coarse rugosity.

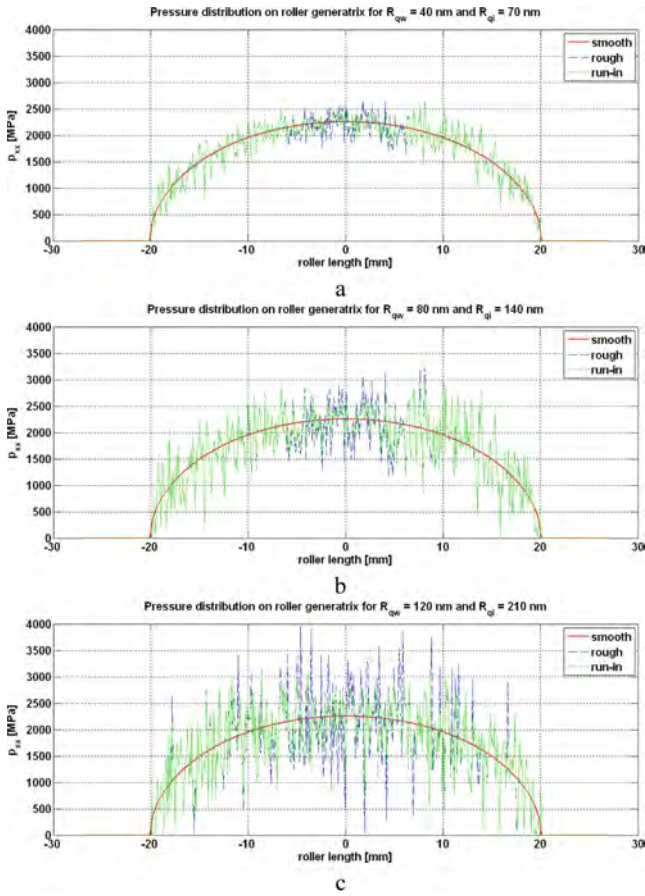


Fig. 7. Pressures repartitions for the heavy charged roller/inner ring contact.

4 Bearing Lives Comparisons

The generally evaluation of the rolling bearings basic rating life take into account just the dynamic capacity charge C , the equivalent charge on the bearing P and an exponent p relying on the shape of rolling element:

$$L_{10} = \left[\frac{C}{P} \right]^p \quad (15)$$

where $p = 10/3$ for rollers and $p = 3$ for balls [31, 33].

To consider the changes of microtopography on the active surfaces as result of the running-in process, the basic reference rating life and modified rating life as described in [26, 31, 34] have been evaluated in this article.

4.1 Modified Bearing Life

The κ Parameter Approach. Viscosity Rate and Film Parameter Approach. The magnitude of the dynamic capacity charge C given by the rolling bearing manufacturers and the calculation method depicted in [31] are often utilized for general estimation of the modified rating life, L_{10m} :

$$L_{10m} = a_{ISO} \cdot L_{10} = a_{ISO} \cdot \left[\frac{C}{P} \right]^p \quad (16)$$

The modification factor, a_{ISO} , is given by the subsequent relation:

$$a_{ISO} = f\left(\frac{\eta_c \cdot P_u}{P}, \kappa\right) \quad (17)$$

where: f is a function described by ISO 281:2007, (Eqs. (34)–(37) [31]), η_c is the contamination index, and P_u is the fatigue charge threshold.

Corresponding to [31], for lubrication with mineral oil and raceway surfaces of rolling bearing processed with *quality of good manufacture*, the state of lubrication is depicted by a complex lubricate parameter κ , described as the relation between the current kinematic viscosity ν and the reference kinematic viscosity ν_1 , [32]:

$$\kappa = \nu / \nu_1 \quad (18)$$

The lubricate parameter λ just rely on two factors: the thickness of lubricating layer and rugosity, although κ , it is just associated to the thickness of lubricating layer, and permits for more manageability the consideration of another specific life of rolling bearing associated to safety factors as inlet shear heating effects and starvation.

In [19] it is remarked that the actual meaning of κ (ISO 281:2007 [31]) still fails to consider important effects as: an actual film height equation and rugosity deformation.

4.2 Rolling Bearing Durability

To evaluate the roller bearing durability with the methodology given by standards ISO 281:2007 [31] and ISO 16281:2008 [26] two levels of loading have been considered: a medium radial loading (for running-in process presented previously) and a light radial loading (for normal operating condition).

Table 1 presents the modified reference rating lives L_{10m} for a medium load ($F_R = 112.5$ kN), smooth and three values of the surface rugosity parameters. The same running conditions have been considered in all three simulations: working temperature $t = 50$ °C, level of contamination $\eta_c = 0.8$, rotation speed $n = 1000$ rpm.

The modified reference rating life has lower values for rough surfaces like smooth surface, and more lower as the rugosity is coarser. Further the running-in process the modified reference rating life increase with approximate 1000 h for the smaller and moderate rough surfaces and with more than 1250 h for the coarser rough surface.

Table 1. Modified reference rating life for a medium load ($F_R = 0.185 \cdot C = 112.5$ kN).

Rugosity of roller	Rugosity of inner ring	Basic rating life, L_{10} , hours	Modified reference rating life, L_{10m} , hours	
R_{qw} [nm]	R_{qi} [nm]		Before	Run-in
Smooth	Smooth	4668	10796	
40	70		5997	6915
80	140		1567	2561
120	210		246	1505

Table 2. Modified reference rating life for a light load ($F_R = 0.055 \cdot C = 33.5$ kN).

Rugosity of roller	Rugosity of inner ring	Basic rating life, L_{10} , hours	Modified reference rating life, L_{10m} , hours	
R_{qw} [nm]	R_{qi} [nm]		Before	Run-in
Smooth	Smooth	264700	688750	
40	70		218660	324140
80	140		28205	74993
120	210		2297	38602

The modified reference rating lives L_{10m} for a light load ($F_R = 33.5$ kN) are presented in Table 2. As in the previous table, the modified reference rating life has lower values for rough surfaces like smooth surface. For the modified surfaces subjected to a medium load further 300 run-in cycles, the modified reference rating life increase, seemingly a greater enhancement for the coarser rugosity, approximately 16 times higher like ahead run-in, however a importantly enhancement for the smaller rugosity, almost 105500 h furthermore like ahead run-in.

5 Conclusions

The microtopography of the working surfaces subjected on rolling contact rely primarily on the surface machining technologies and secondly on the evolution of the running-in process.

To simulate the running-in phenomenon, random three-dimensional rough surfaces have been generated numerically and further considered into an elastic-plastic numerical model. For the case of CARB rolling bearing the values for modified reference rating life have been considered to estimate the effect of the run-in.

The experimental data, of running-in process, acquired on AMSLER machine present a very good agreement with the numerical data for two discs test and with numerical data obtained with the running-in model exhibited in [1, 35].

The asperities presence on working surfaces in rolling contact causes high peaks in pressure repartitions, and as the rough surfaces are coarser the higher are the pressure peaks.

The modified rating life is seriously reduced for the coarse rough surface, by two size order, right further running-in process, by one size order, like for the fine rough surface or smooth surface.






References

1. Jamari, J.: Running-in of rolling contacts. Ph.D. thesis, Twente (2006)
2. Jamari, J., de Rooij, M.B., Schipper, D.J.: Plastic deterministic contact of rough surfaces. *ASME Trans. J. Tribol.* **129**, 957–962 (2007)
3. Tasan, Y.C., de Rooij, M.B., Schipper, D.J.: Changes in the micro-geometry of a rolling contact. *Tribol. Int.* **40**, 672–679 (2007)
4. Robbe-Valloire, F.: Statistical analysis of asperities on a rough surface. *Wear* **249**, 401–408 (2001)
5. Taylor Hobson Precision: Exploring surface texture. TH Ltd. (2003)
6. Stawicki, T., Sedlak, P., Koniuszy, A.: The testing of the influence of the roughness of the crankshaft journal upon the durability of the crankshaft bearing in engines of agricultural machines. *Sci. Probl. Mach. Op. Maint.* **4**, 7–17 (2010)
7. Jacobson, S., Hogmark, S.: Surface modifications in tribological contacts. *Wear* **266**, 370–378 (2009)
8. Andersson, M., Sosa, M., Olofsson, U.: The effect of running-in on the efficiency of superfinished gears. *Tribol. Int.* **93**, 71–77 (2016)
9. Sjöberg, S., Sosa, M., Andersson, M., Olofsson, U.: Analysis of efficiency of spur ground gears and the influence of running-in. *Tribol. Int.* **93**, 172–181 (2016)
10. Mallipeddi, D., Norell, M., Sosa, M., Nyborg, L.: Influence of running-in on surface characteristics of efficiency tested ground gears. *Tribol. Int.* **115**, 45–58 (2017)
11. Allwood, J., Ciftci, H.: An incremental solution method for rough contact problems. *Wear* **258**, 1601–1615 (2005)
12. Allwood, J.: Survey and performance assessment of solution methods for elastic rough contact problems. *ASME Trans. J. Tribol.* **127**, 10–23 (2005)
13. Bakolas, V.: Numerical generation of arbitrarily oriented non-gaussian three-dimensional rough surfaces. *Wear* **254**, 546–554 (2003)
14. Crețu, S.: Random simulation of Gaussian rough surfaces: Part I. Theoretical formulation. *Bul. Institut. Pol. Iași* **1–2(LII)**, 1–16 (2006)
15. Akbarzadeh, S., Khonsari, M.M.: Experimental and theoretical investigation of running-in. *Tribol. Int.* **44**, 92–100 (2011)
16. Clarke, A., Weeks, I.J.J., Snidle, R.W., Evans, H.P.: Running-in and micropitting behavior of steel surfaces under mixed lubrication conditions. *Tribol. Int.* **101**, 59–68 (2016)
17. Pu, W., Zhu, D., Wang, J., Wang, Q.J.: Rolling-sliding contact fatigue of surfaces with sinusoidal roughness. *Int. J. Fatigue* **90**, 57–68 (2016)
18. Rycerz, P., Olver, A., Kadiric, A.: Propagation of surface initiated rolling contact fatigue cracks in bearing steel. *Int. J. Fatigue* **97**, 29–38 (2017)
19. Morales-Espejel, G.E., Gabelli, A., Ioannides, E.: Micro-geometry lubrication and life ratings of rolling bearings. *Proc. Inst. Mech. E Part C: J. Mech. Eng. Sci.* **224**, 2610–2628 (2010)
20. Morales-Espejel, G.E., Gabelli, A., de Vries, A.J.C.: A model for rolling bearing life with surface and subsurface survival-tribological effects. *Tribol. Trans.* **58**, 894–906 (2015)

21. Liu, M., Wu, C., Yan, C.: Predicting fatigue life for finite roller contacts based on a mixed EHL model using realistic surface roughness. *J. Mech. Sci. Technol.* **31**(7), 3419–3428 (2017)
22. Benchea, M., Iovan-Dragomir, A., Crețu, S.: Misalignment effects in cylindrical roller bearings. *Appl. Mech. Mater.* **658**, 277–282 (2014)
23. Crețu, S., Benchea, M., Iovan-Dragomir, A.: On basic reference rating life of cylindrical roller bearings. Part II - elastic-plastic analysis. *J. Balk. Tribol. Assoc.* **22**, 272–280 (2016)
24. Chaboche, J.L.: A review of some plasticity and viscoplasticity constitutive theories. *Int. J. Plast.* **24**, 1642–1693 (2008)
25. Besson, J., Cailletaud, G., Chaboche, J.L., Forest, S., Blétry, M.: *Non-Linear Mechanics of Materials*. Springer (2010)
26. ISO 16281:2008: Rolling bearings-methods for calculating the modified reference rating life for universally loaded bearings
27. Whitehouse, D.J., Archard, J.F.: The proprieties of random surface of significance in their contact. *Proc. R. Soc. Lond. A* **316**, 97–121 (1970)
28. Crețu, S.: The influence of the correlation length on pressure distribution and stress state in concentrated rough contacts. In: *Proceedings of ASME/ASLE IJTC-2006, San Antonio, USA* (2006)
29. Linares Arregui, I., Alfredsson, B.: Elastic-plastic characterization of a high strength bainitic roller bearing steel - experiments and modelling. *Int. J. Mech. Sci.* **52**, 1254–1268 (2010)
30. SKF Group: *Rolling bearings catalogue* (2013)
31. ISO 281:2007: *Rolling bearings-dynamic load ratings and rating life*
32. Ioannides, E., Bergling, G., Gabelli, A.: An analytical formulation for the life rating of rolling bearings. *Acta Polytech. Scand. Mech.* **137**, 1–80 (1999)
33. Crețu, S., Benchea, M., Crețu, O.: Compressive residual stresses effect on fatigue life of rolling bearings. In: *Proceedings of IMECE-07, Seattle, paper 43561* (2007)
34. Benchea, M., Crețu, S.: Profile evolution in cylindrical roller bearings. II. Rating lives evaluation. *Bull. Inst. Polit. Iași* **62/66**(3), 35–42 (2016)
35. Jamari, J., Schipper, D.J.: Deformation due to contact between a rough surface and a smooth ball. *Wear* **262**, 138–145 (2007)

Article

Ni-Cr Alloys Assessment for Dental Implants Suitability

Dragos Cristian Achitei ¹, Mădălina Simona Baltatu ^{1,*} , Petrică Vizureanu ^{1,2} , Andrei Victor Sandu ^{1,3} ,
Marcelin Benchea ^{4,*}  and Bogdan Istrate ⁴ 

¹ Department of Technologies and Equipments for Materials Processing, Faculty of Materials Science and Engineering, Gheorghe Asachi Technical University of Iași, Blvd. Mangeron, No. 51, 700050 Iași, Romania

² Technical Sciences Academy of Romania, Dacia Blvd. 26, 030167 Bucharest, Romania

³ National Institute for Research and Development in Environmental Protection INCDPM, Splaiul Independentei 294, 060031 Bucharest, Romania

⁴ Faculty of Mechanical Engineering, Gheorghe Asachi Technical University of Iași, Blvd. Mangeron, No. 51, 700050 Iași, Romania

* Correspondence: cercel.msimona@yahoo.com (M.S.B.); marcelin.benchea@tuiasi.ro (M.B.)

Abstract: The performance of the field and the condition of success in oral implantology today require the review and reevaluation of the means that contribute essentially to ensuring the stability and durability of the implant, starting from the nature of the biomaterial and continuing with the characteristics of the optimally designed biosurface. This paper proposes a comparative analysis of three commercial alloys, VeraBond, Kera N, and VeraSoft, compared to a modified dental alloy, with the aim of improving some mechanical properties. They have been studied structurally and mechanically. The microstructural structure shows that the alloys crystallize in the face-centered cube system, and the cast alloy has a dendritic structure with large grains. XRD diffractograms highlight that alloys exhibit three compounds Cr156.00 Al596.00: 9013031, Ni4.00, and Cr30.00Al48.00. The hardness measurements showed values between 203 HV and 430 HV. As the percentage of silicon increases, the hardness decreases. The modulus of elasticity obtained by the indentation method for the dental alloys was in the range of 46–153 GPa. The results showed that the hardness and elastic modulus of the new alloy was significantly minimized compared to the classical alloys used.

Keywords: Ni-Cr; properties; cast samples; dental alloys



Citation: Achitei, D.C.; Baltatu, M.S.; Vizureanu, P.; Sandu, A.V.; Benchea, M.; Istrate, B. Ni-Cr Alloys Assessment for Dental Implants Suitability. *Appl. Sci.* **2022**, *12*, 12814. <https://doi.org/10.3390/app122412814>

Academic Editor: Antonio Scarano

Received: 17 November 2022

Accepted: 11 December 2022

Published: 13 December 2022

Publisher's Note: MDPI stays neutral with regard to jurisdictional claims in published maps and institutional affiliations.



Copyright: © 2022 by the authors. Licensee MDPI, Basel, Switzerland. This article is an open access article distributed under the terms and conditions of the Creative Commons Attribution (CC BY) license (<https://creativecommons.org/licenses/by/4.0/>).

1. Introduction

The dental implant, with all its forms, can be defined as a body foreign to the body (alloplastic material), which is surgically inserted at the level of the jawbone, with the main purpose of supporting the prosthetic elements used in the treatment of edentulousness. Unlike other types of medical implants, the dental implant is considered “open” due to the communication between it and the oral cavity, which is a septic environment with many potential factors of aggression [1,2].

Current research regarding the modification and control of the biomaterial–tissue interaction to improve the osseointegration process of the implant is oriented towards capitalizing on the progress made in regenerative medicine [3–5], using tissue engineering techniques and developing the field of biomimetic materials (so-called smart biomaterials) [6–9].

The applications of biomaterials in the field of medicine are primarily due to the requirements imposed by medical practice [10,11] but also by the continuous evolution of science. A permanent correlation of research in the fields of chemistry, biology, engineering, and medicine leads the science of biomaterials to obtain new materials that can solve the multiple existing medical problems to the current requirements [12].

The physical, chemical and mechanical properties of dental materials are of particular importance to support the desire to forecast and design new devices and material assemblies. Thus, the review of these properties has the aim of creating a specific framework for

starting the complete study of dental materials; without the knowledge of these data, new designs will be stuck or simply deviate from the expected results [13,14].

It has been proven that the general properties and the surface properties of the metals that have been used for implants directly influence and, in some cases, even control the dynamics at the tissue interface from the time of initial placement on the live to the final removal. It is admitted that compatibility is a two-way process between the biomaterials incorporated in the device and the implant host environment [15,16].

Remarkable advances have been made in dentistry. In the last 25 years, the rapid progress of discoveries regarding biomaterials and implants has only been possible through close collaboration between doctors, biologists, and engineers. Both the improvement in the types of implants and the discovery of new materials that are best tolerated by the body were pursued [17–19].

Ni-Cr alloys have appeared as an alternative to Co-Cr alloys that present a low ductility, increase shrinkage upon solidification, and have a tendency to oxidize. In the industry, these alloys are known as NIMONIC and are used in the construction of reaction engines [20–22].

Ni-Cr alloys contain up to 70% nickel. Several types of alloys containing Ni are used in dentistry:

- Ni-Cr-Fe alloys (wipla type, classic) with a percentage of 48–66%Ni;
- Ni-Cr alloys also contain small percentages of Mo, Al, Mn, Be, Cu, Co, Ga, and Fe to improve certain properties of the alloy.
- Co-Cr-Ni alloys are used in skeletal prosthesis technology [23–25].

Biocompatibility is a very important aspect of alloys that have medical applications. The release of metal ions from these alloys is determined by the percentage of chromium and must be above 20% for proper passivation of the alloy. Chromium, as an element in the composition of an alloy, changes the melting temperature and increases the mechanical properties, and by forming oxides, it increases the corrosion resistance and the bond with ceramics.

Nickel is an essential element for the human body, containing about 10 mg of Ni. The daily intake is recommended to be 100 µg per day, mainly through food. Nickel compounds are generally very water-soluble, and therefore, in the case of corrosion, they are quickly entrained by saliva in the intestinal tract. For this reason, the contact time with the Langerhans cells present in the oral mucosa and acting as receptors is very short. Due to its nature and chemical structure, the oral mucosa allows for faster diffusion of Ni ions than the skin, and the risk of sensitization in the oral cavity is extremely low. There is currently no description of Ni accumulations in the body. Despite the relatively frequent allergies to skin contact with Ni, it has been clinically observed that the use of Ni-Cr alloys in the oral cavity does not systematically cause allergic reactions [26–28].

If we were to consider only the initial corrosion in the oral environment of the stable Ni-Cr alloy (e.g., Wiron88/Bego), in order to reach the recommended daily level of Ni absorption of 100 µg, it would result in 25 cm² of this alloy. It should also be taken into account that the initial corrosion phenomenon, namely the release of ions, decreases rapidly in the first hours and days, and after a few days, much fewer ions are released. We can conclude that a possible sensitization occurs only in very sensitive people. Given the small amounts released and the short biological half-life of Ni, a systemic toxic attack must be excluded. However, we cannot exclude a local toxic action, which can also occur for other metals. Such a phenomenon can occur in the case of incorrect finishing by the technician of the prosthetic piece.

The use of metallic biomaterials in the human body is dependent on certain specific characteristics of the material, as well as on the specific function it has to perform.

Subsequently, through improvements to the materials and design, the success rate increased. The concurrent development of asepsis and antisepsis protocols and anesthetic techniques also contribute greatly to this good outcome. After 1980, implantology aroused more and more interest in doctors from many corners of the world, and various congresses have been organized on this topic (important to mention the one in Toronto in 1982 where

Brånemark published the results of his research for more than 15 years in the field of osseointegration). From this moment, implantology begins to make unexpected progress. The number of dental implants applied worldwide is still increasing year by year [29,30].

We carried out a preliminary study in order to follow the opportunity of introducing a new type of dental implant. The new alloy was designed so that, by eliminating the harmful effects present in the dental alloys frequently used today in oral implantology, we could control the intrinsic biocompatibility of the material: a character with a defining influence on the osseointegration process of the implant by adding silicon. We choose the solution of alloying with an element such as silicon to improve the mechanical properties [31].

The aim of this work was to change the percentage of the metallic silicon of the VeraSoft-type dental alloy from the percentage of 1.60% to 4.32% in order to study and obtain mechanical properties suitable for further uses. For comparison, three commercial alloys, VeraBond, Kera N, and VeraSoft, were used, with the properties taken from the specialized literature. They have been studied structurally and mechanically.

2. Materials and Methods

2.1. Materials Preparation

In this article, four alloys were used for testing and comparison. They were bought and are classic alloys that are currently used, while one alloy was modified to improve the properties: one Verabond alloy, one Kera N alloy, two VeraSoft alloys, and a VeraSoft alloy to which metallic silicon was added to.

The metal charge for making the alloy must be of high quality and purity, degreased, and properly prepared. A commercially purchased dental alloy of the VeraSoft type and high-purity metallic silicon, 99.6%, provided by Alfa Aesar from Thermo Fisher Scientific, were used as raw materials. In order to obtain the new VeraSoft alloy with a modified percentage, the use of an indirect heating furnace was chosen.

Two semi-finished products from the new alloy were obtained: a sufficient quantity for taking the samples needed for the laboratory tests that had in mind the proposed characterization. Figure 1 highlights the technological flow of developing the new VeraSoft alloy. The developed alloy was analyzed by structural and mechanical characterization methods.

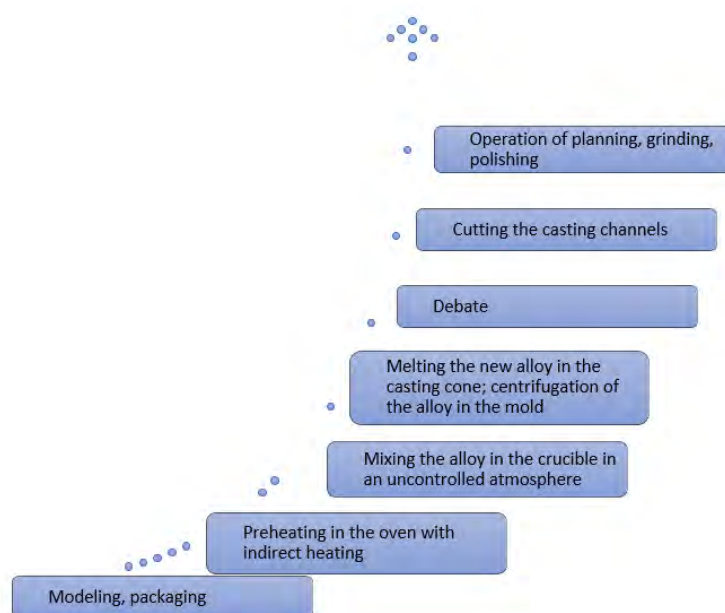


Figure 1. The technological flow of developing the new VeraSoft alloy.

In order to prepare the metallographic samples, a sequence of stages was completed as follows:

- The sanding process was performed with sanding papers. This was achieved by successive sanding operations on large-grained papers to small-grained papers.
- The polishing process with the help of felt. This was performed using aluminum oxide abrasive suspension of different grain sizes with the final goal of obtaining a mirror-gloss surface.
- The metallographic attack aimed to highlight the structural constituents. According to the ASM Handbook: 2 mL FeCl₃, 48 mL H₂O, and 50 mL HCL for 15 s at room temperature should be used.

VeraBond alloy (Figure 2a) is formulated for “Ceramico II” and other types of ceramics: Excelco, Spectrum, Noritake, Synspar, Shofu-Crystar, as well as with other medium-grained porcelains. The analyzed alloy has applications as a support for porcelain, and it is applied from a single element to full bridges, Maryland bridge, support for acrylic and composites from single elements to full bridge, all-metal crowns, and superstructures for implants.

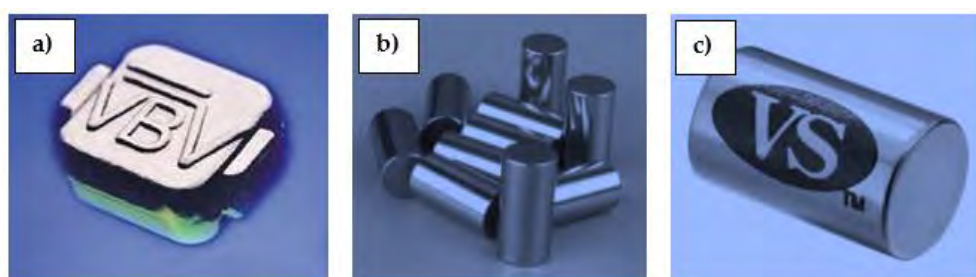


Figure 2. The commercial aspect of the analyzed samples: (a) VeraBond, (b) Kera N, (c) VeraSoft.

The KeraN alloy (Figure 2b) is an alloy of non-precious metals Nickel–Chromium, without Beryllium for ceramic work at high temperatures. It is suitable for open-fire processing and for dissociated working methods. An oxidizer is not required.

The VeraSoft (Figure 2c) alloy is a Ni–Cr casting alloy for metal crowns and bridges, pivots, restorations, and substructures for metal-acrylic crowns and bridges.

It is very important to recognize that synthetic materials have general and specific surface characteristics that depend on their properties. These characteristics must be known before any medical application, but they must also be known in relation to the changes that may occur over time in the body. In other words, any change in properties over time must be anticipated from the start and motivated by the choice of biomaterials and/or the device design.

The use of materials for tissue reconstruction in the human body dates back several thousand years, but clinically important advances have been achieved in the last century. The first interventions to replace some affected tissues date back more than 2000 years and are related to the Aztec, Chinese, and Roman civilizations [32,33].

2.2. Microstructural Characterization Methods

In order to obtain the most accurate determination, ten EDX determinations were performed in different areas of the semi-finished product to verify the concentrations obtained. To determine the chemical composition of the newly obtained alloy, the Vega Tescan LMH II equipment was used, using the Bruker EDAX detector attached to the SEM equipment.

The metallographic analysis provides information on the micrographic structure of the alloy, its nature, shape, dimensions, and distribution mode. A microscope Zeiss Axio Imager A1, was used for the optical analysis of high-precision optical images.

X-Ray diffractions (XRD, Panalytical, Almelo, The Netherlands) were conducted utilizing an Xpert PRO MPD 3060 facility from Panalytical (Almelo, The Netherlands) equipped with a Cu X-ray tube ($K\alpha = 1.54051$), 2θ : $10\text{--}70^\circ$, step size: 0.13° , time/step: 51 s, and a scan speed of $0.065651^\circ/\text{s}$ in the reflection mode. Highscore Plus 3.0 software was used to analyze the data in order to determine the phase components and their parameters.

2.3. Mechanical Properties

The determination of the hardness of the commercial Ni-Cr alloys analyzed was carried out on a PMT3 model durometer by the Vickers method, using a pressing weight of 100 gf and a pyramidal diamond indenter.

Indentation is a test method based on the principles used to determine the modulus of elasticity, stiffness, etc. The indentation tests were performed using a device for tribological and mechanical determinations Universal Micro-Tribometer CETR UMT-2. For a more precise determination, three determinations were made for each individual alloy. After completing the working stages and recording them through the software of the UMT 2 device, the imprint curves (depth vs. force) of the new alloy obtained by the VIEWER program were plotted.

3. Results

3.1. Microstructural Analysis

Figure 3 shows the Spectrum EDX obtained and the new composition obtained after elaboration.

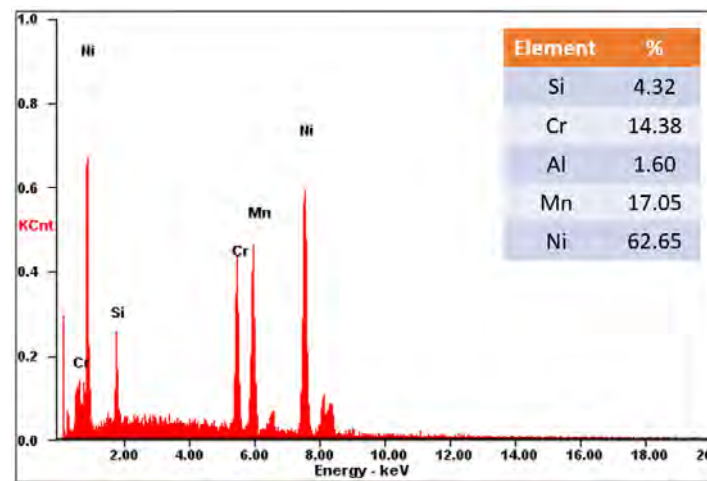


Figure 3. EDX spectrum for the newly obtained alloy with chemical composition obtained.

The chemical composition of the alloys is presented in Table 1 with average values for the three tests (\pm standard deviation) that were obtained regarding the chemical composition measurements results.

Table 1. The chemical composition of the alloys studied.

	Ni [%]	Cr [%]	Mo [%]	Al [%]	Be [%]	Co [%]	Ti [%]	Si [%]	Mn [%]
VeraBond	76.75 \pm 0.20	12.60 \pm 0.10	5.00 \pm 0.10	2.90 \pm 0.10	1.95 \pm 0.10	0.45 \pm 0.10	0.35 \pm 0.10	-	-
Kera N	61.60 \pm 0.30	25.50 \pm 0.10	11.00 \pm 0.10	0.40 \pm 0.10	-	-	-	1.50 \pm 0.10	-
VeraSoft	62.80 \pm 0.10	14.50 \pm 0.10	-	1.60 \pm 0.10	-	-	-	1.60 \pm 0.10	19.50 \pm 0.10
VeraSoft modified	62.65 \pm 0.20	14.38 \pm 0.10	-	1.60 \pm 0.10	-	-	-	4.32 \pm 0.10	17.05 \pm 0.10

The microstructure depends to a large extent on the alloying components but also on the processing conditions (melting, casting, and heat treatment).

Figure 4 presents the optical microstructure of the VeraBond, Kera N, VeraSoft, and the modified VeraSoft. Micrographs of the dental alloys are highlighted homogeneous dendritic structures.

VeraSoft and the modified VeraSoft have a dendritic structure, typical of cast alloys, which are solidified after medium to high-speed cooling. For the modified VeraSoft (Figure 4d,h), the influence of the addition of the silicon element is very well observed; in this, it has refined the structure and contains, along with the dendritic phase, eutectic separations that are observable in the interdendritic space.

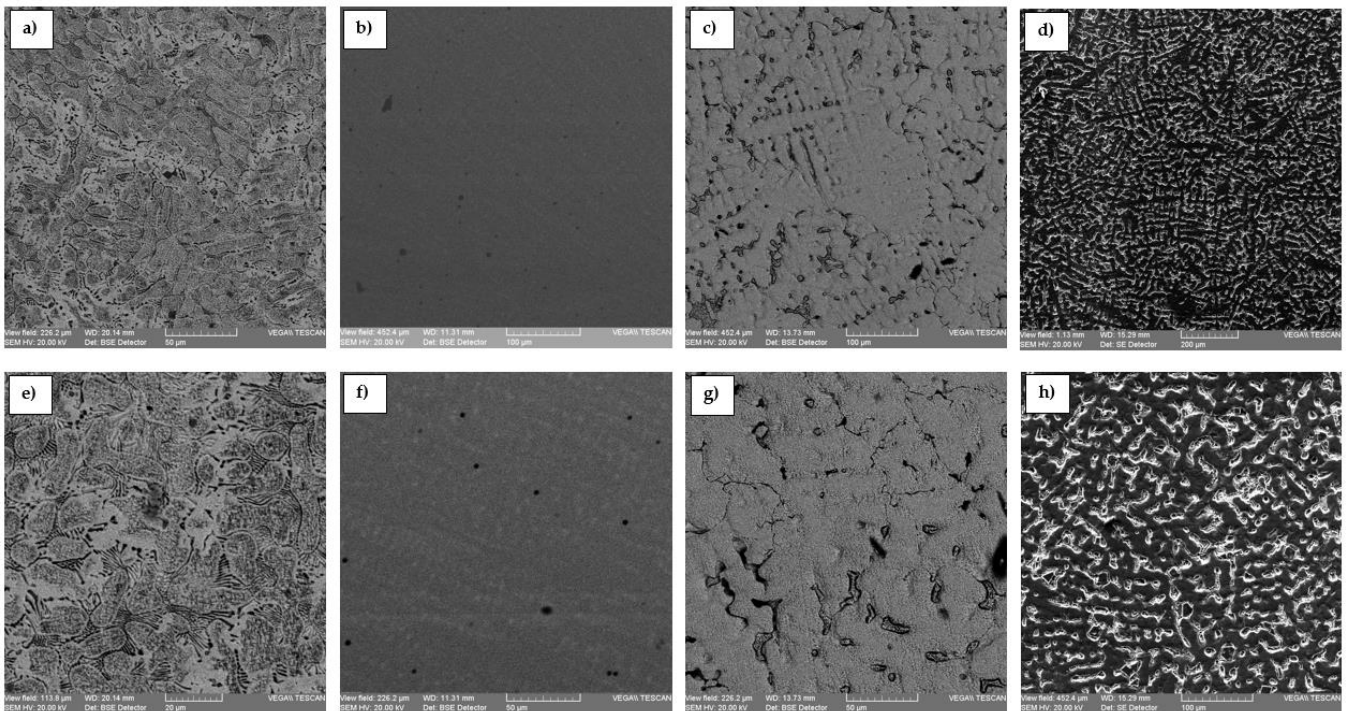


Figure 4. Microstructure analysis of experimental alloys: (a) VeraBond (200×), (b) Keran N (200×), (c) VeraSoft (200×), (d) VeraSoft modified (200×) (e) VeraBond (500×), (f) Kera N (500×), (g) VeraSoft (500×), (h) VeraSoft modified (500×).

The microstructure of dental alloys shows a homogeneous cellular structure with cellular boundaries. Similar findings were also reported by some previous reports [5,6]. This was due to the rapid solidification and strong temperature gradients of the melt during the melting process.

Usually, Ni-Cr alloys also contain, in smaller concentrations, Al, Co (hardening elements) and B, Si (deoxidizing elements). These alloys constitute a support for fused porcelain.

The alloys crystallize in the face-centered cube system, and the cast alloy has a dendritic structure with large grains.

The hardening of the alloy involves the precipitation of the subsequent phase or phases, particularly called the γ phase, consisting of $(\text{NiCo})_3(\text{AlTi})$. Carbs can form interdendritically. The values of the modulus of elasticity and hardness are somewhat lower than those presented by Co-Cr.

Solidification shrinkage is 1.5%, and the alloys are normally melted in induction furnaces and cast into phosphate forms. Due to the low-temperature range, Ni-Cr alloys offer a much more precise casting, which allows dental bridges and crowns to have minimal deviations [34,35].

3.2. Structural Analysis

XRD is a useful technique to study phases in dental alloys and their transformations as a function of temperature. Figure 5 presents the diffractograms of experimental alloys.

The phases revealed by XRD at the different analysis temperatures were in good agreement with those found in previous optical microstructures of transformations in these alloys. For the modified VeraSoft, new XRD peaks appear to result from the low-temperature transformation in martensite, which the optical microstructure has shown.

XRD diffractograms highlight that alloys exhibit three compounds: 2100373, Reference code: 96-210-0374, Chemical formula: $\text{Cr}_{156.00}\text{Al}_{596.00}$; 9013031, Reference code: 96-901-3032, Chemical formula: $\text{Ni}_{4.00}$; 1100049, Reference code: 96-110-0050, Chemical formula: $\text{Cr}_{30.00}\text{Al}_{48.00}$ [36].

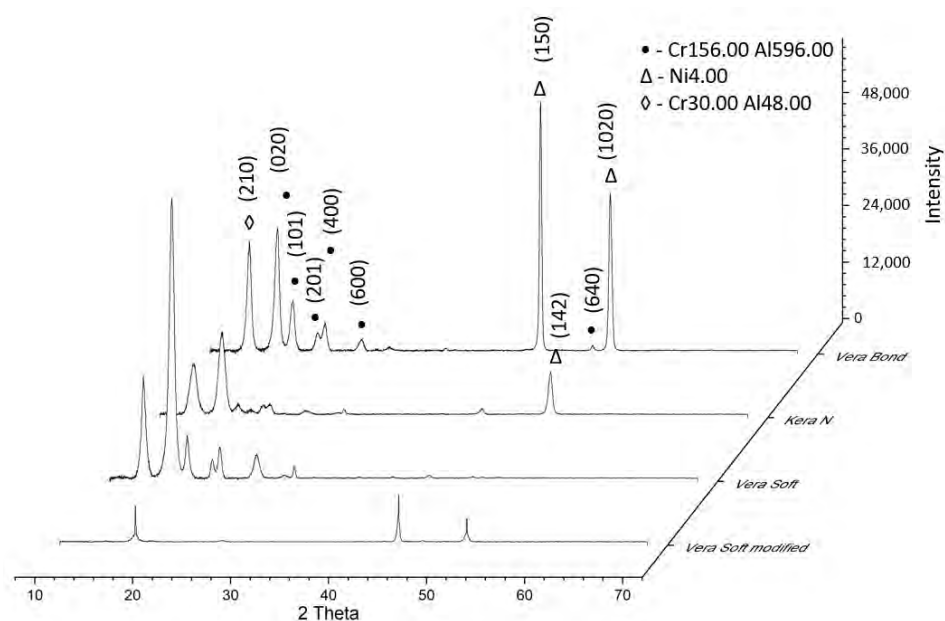


Figure 5. Diffractograms of experimental alloys.

These compounds that were formed in alloys were identified by XRD analysis. The main characteristics for Cr156.00 Al596.00 are as follows: crystal system: hexagonal, a (Å): 32.3000, b (Å): 32.3000, c (Å): 12.4000, α (°): 90.00, β (°): 90.00, γ (°): 90.00, calculated density (g/cm^3): 3.59, and volume of the cell (10^6 pm^3): 11203.59. The main characteristics for Ni4.00 are as follows: crystal system: cubic, a (Å): 3.5870, b (Å): 3.5870, c (Å): 3.5870, α (°): 90.00, β (°): 90.00, γ (°): 90.00, calculated density (g/cm^3): 8.45, and volume of the cell (10^6 pm^3): 46.15. The main characteristics for Cr30.00Al48.00 are as follows: hexagonal, a (Å): 12.7184, b (Å): 12.7184, c (Å): 7.9367, α (°): 90.0000, β (°): 90.0000, γ (°): 120.0000, calculated density (g/cm^3): 4.26, and volume of the cell (10^6 pm^3): 1111.8.

3.3. Hardness Results

For the dental alloys used in this study, Vickers hardness was determined by indentation tests. The samples were polished with 1 μm of alumina paste. After imprinting, the surface of the samples was processed, and the results were obtained tangentially to the surface with a Vickers indenter applied every 0.5 mm along the diameter of the sample. A load of 50 (Kg/mm^2) and contact times of 15 s were used. On this basis, the average hardness, expressed in degrees Vickers (HV), was determined for each sample studied.

The Vickers hardness test involves a pyramid-shaped diamond indenter with a square base and a penetration angle of 136° ; the load, in this case, is applied to the tested material constantly. The length of the penetrator's diagonals is used to determine the size of the indentation that it leaves in the material. The significant advantage of this test is that very small samples can be tested due to their small penetrator. Additionally, the ability of the test to work with varied tasks leads to another advantage; namely, hardness determinations can be made on both soft and hard materials. Vickers testing gives very good results in the case of brittle materials, but also, the situations in which ductile materials are encountered have been successfully solved.

Table 2 shows the average values for 10 tests (\pm Standard Deviation) obtained regarding the hardness measurement results of the dental alloys. The measurements showed values between 203 HV and 430 HV. As the percentage of silicon increases, the hardness decreases.

Modified VeraSoft has a lower hardness value compared to the classic VeraSoft alloy. The addition of silicon was beneficial and decreased the hardness. For dental applications, a very high hardness value is not necessary.

Table 2. The hardness values for alloys studied.

Alloys	VeraBond	Kera N	VeraSoft	VeraSoft Modified
HV	429.5 ± 4.60	388.8 ± 5.10	251.5 ± 3.40	203.4 ± 5.70

3.4. Indentation Results

Metals and their alloys were the first materials used in human prosthetics, which, together with other inorganic and organic materials, are still widely used today. The use of metallic materials in one or another field of technology depends on the relationship between their structure and properties.

Micro indentation is a hardness testing technique for measuring the physical properties of samples, such as film layers that are often too small for conventional physical testing techniques.

The samples to be tested by micro indentation must be securely mounted and also have a relatively flat test surface. Samples are often prepared using the same techniques as the samples prepared for electron microscopy, requiring mounting in a hard matrix such as epoxy and then planar polishing of the test surface.

Figure 6 shows the response of the alloys during the indentation tests in the form of force-depth dependencies, and Table 3 presents the results of the indentation test with the average values for the three tests (± standard deviation) performed.

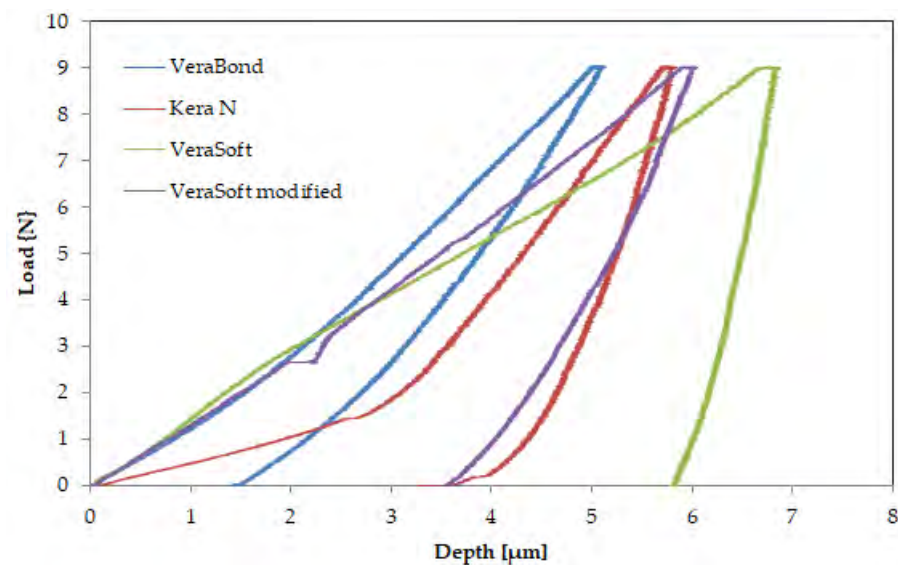


Figure 6. Indentation curves of the studied alloys: (a) VeraBond, (b) Kera N, (c) VeraSoft, (d) VeraSoft modified.

Table 3. Indentation results.

Sample	Loading Deformation [N]	Release Deformation [μm]	Young Modulus [GPa]	Stiffness [N/μm]	Specimen Poisson Ratio
VeraBond	9.01 ± 0.20	5.12 ± 0.10	56.37 ± 0.50	3.314 ± 0.10	0.23
Kera N	9.01 ± 0.30	5.73 ± 0.20	152.95 ± 0.60	12.83 ± 0.30	0.23
VeraSoft	9.01 ± 0.10	6.84 ± 0.10	139.78 ± 0.90	13.05 ± 0.40	0.23
VeraSoft modified	9.02 ± 0.10	5.62 ± 0.30	46.79 ± 0.80	4.589 ± 0.10	0.23

The mean value ± standard deviation values of at least three independent specimens were used to obtain all the results. The authors [37] stated that Young's modulus could be predicted using Equations (1) and for the Poisson ratio Equation (2).

$$E = \frac{(1 - \nu^2)}{2ak\left(\frac{a}{h}, \nu\right)} \cdot \frac{P}{w} \quad (1)$$

$$\frac{P_1 w_2 a_2}{P_2 w_1 a_1} = \frac{k\left(\frac{a_1}{h}, \nu\right)}{k\left(\frac{a_2}{h}, \nu\right)} \quad (2)$$

Mechanical properties that characterize the behavior of metals and alloys under the action of external forces are the basis of their most important applications.

Because the mechanical properties of metals and alloys are structure dependent, they are very sensitive to the effects of manufacturing processes, and the same material can produce different properties.

The modulus of elasticity obtained by the indentation method for the dental alloys is in the range of 46–153 GPa. The lowest value is presented by the new-modified VeraSoft (46.79 GPa). The addition of silicon had a beneficial effect on the mechanical properties, reducing the modulus of elasticity

The biomaterials used in oral implantology must ensure the transmission of occlusal forces to the supporting tissues. For this reason, they must present sufficient mechanical resistance but also an elasticity adapted to the bone. The functional biocompatibility of the implant material mainly concerns the modulus of elasticity and mechanical strength. The elasticity mode is the characteristic with significant influence on the bone remodeling process, causing the destruction of the tissue-implant assembly in the conditions of a major difference between the components of the implant-bone assembly [38–40].

A difference between the elastic modulus causes a mechanical stress on the tissue that is different from the physiologically normal one. The finite element analysis of the behavior of the bone-implant assembly under mechanical stress indicated that a material with a small modulus of elasticity could determine a distribution much closer to that of the mechanical stresses in the surrounding bone tissue.

The newly developed alloy aims to be used in medical applications, with the role of fulfilling the functional requirements and removing some disadvantages in the classic alloys used as biomaterials in human tissue.

The superior valorization of metallic biomaterials requires knowledge of the chemical, physical, mechanical, thermal, electrical, magnetic, optical, as well as technological properties by means of the specific methods of these categories of materials.

4. Conclusions

The performance of the field and the condition of success in oral implantology require today the review and reevaluation of the means that contribute essentially to ensure the stability and durability of the implant, starting from the nature of the biomaterial and continuing with the characteristics of the optimally designed biosurface.

Dental metal alloys have advantages such as a pleasant appearance, low price (the non-precious ones), and good physical and mechanical properties (such as high modulus of elasticity), which allow the use of smaller sections of the alloy, and therefore, less destruction to the teeth during crown preparation, They also provide an adequate coefficient of thermal expansion comparable to that of porcelain commonly used for veneering, which maintains the metal and crown ceramics which are intimately bonded during casting and prevents the cracking of the coating.

Precious and semi-precious dental alloys are generally recognized as inert and perfectly biocompatible. Some metals are already considered prohibited for organisms, such as beryllium, nickel, and mercury.

All components of the prosthetic field undergo changes over time, and the reactions of the oral mucosa are the result of mechanical irritation, plaque accumulation, as well as the toxic and/or allergic action of the materials from which the implants are made. For this reason, we must carefully choose the best materials so that once introduced into the human body they do not affect its health.

The aim of this paper consists of a comparative analysis of three commercial alloys, VeraBond, Kera N, and VeraSoft, compared to a modified dental alloy, with the aim of improving some mechanical properties.

Regarding the microstructural analyses, alloys show that the alloys crystallize in the face-centered cube system, and the cast alloy has a dendritic structure with large grains. XRD diffractograms highlight that alloys exhibit three compounds Cr156.00 Al596.00: 9013031, Ni4.00, and Cr30.00Al48.00.

For the mechanical properties, hardness measurements show values between 203 HV and 430 HV. As the percentage of silicon increases, the hardness decreases. The results of the indentation test for the dental alloys were in the range of 46–153 GPa. The results show that the hardness and elastic modulus of the new alloy was significantly minimized compared to the classical alloys used.

The percentage of silicon increased the hardness value and decreased the modulus of elasticity in the case of the new alloy obtained. The newly obtained alloy lends itself to uses in the medical field; the examinations performed to reveal a suitable behavior for prosthetic constructions.

Author Contributions: D.C.A.: conceptualization, management; M.S.B.: writing—original draft preparation, investigation; P.V.: methodology, financing, data curation; A.V.S.: investigation, writing—review and editing; M.B.: validation, investigation; B.I.: investigation, data curation. All authors have read and agreed to the published version of the manuscript.

Funding: This paper was financially supported by the Project “Network of excellence in applied research and innovation for doctoral and postdoctoral programs/InoHubDoc”, project co-funded by the European Social Fund financing agreement no. POCU/993/6/13/153437. This paper was also supported by “Gheorghe Asachi” Technical University from Iași (TUIASI), through the Project “Performance and excellence in postdoctoral research 2022”.

Institutional Review Board Statement: Not applicable.

Informed Consent Statement: Not applicable.

Data Availability Statement: All data provided in the present manuscript are available to whom it may concern.

Conflicts of Interest: The authors declare no conflict of interest.

References

1. Chen, Q.; Thouas, G.A. Metallic implant biomaterials. *Mater. Sci. Eng. R Rep.* **2015**, *87*, 1–57. [[CrossRef](#)]
2. González, J.E.G.; Mirza-Rosca, J.C. Study of the corrosion behavior of titanium and some of its alloys for biomedical and dental implant applications. *J. Electroanal. Chem.* **1999**, *471*, 109–115. [[CrossRef](#)]
3. Baltatu, M.S.; Vizureanu, P.; Balan, T.; Lohan, N.M.; Tugui, C.A. Preliminary Tests for Ti-Mo-Zr-Ta Alloys as Potential Biomaterials. *IOP Conf. Ser. Mater. Sci. Eng.* **2018**, *374*, 012023. [[CrossRef](#)]
4. Baltatu, M.S.; Vizureanu, P.; Sandu, A.V.; Munteanu, C.; Istrate, B. Microstructural analysis and tribological behavior of Ti-based alloys with a ceramic layer using the thermal spray method. *Coatings* **2020**, *10*, 1216. [[CrossRef](#)]
5. Focsaneanu, S.C.; Vizureanu, P.; Sandu, A.V.; Ciobanu, G.; Baltatu, S.M.; Vlad, D. Experimental study on the influence of zirconia surface preparation on deposition of hydroxyapatite. *Rev. Chim.* **2019**, *70*, 2273–2275. [[CrossRef](#)]
6. Baltatu, M.S.; Chiriac-Moruzzi, C.; Vizureanu, P.; Tóth, L.; Novák, J. Effect of Heat Treatment on Some Titanium Alloys Used as Biomaterials. *Appl. Sci.* **2022**, *12*, 11241. [[CrossRef](#)]
7. Celesti, C.; Gervasi, T.; Cicero, N.; Giofrè, S.V.; Espro, C.; Piperopoulos, E.; Gabriele, B.; Mancuso, R.; Lo Vecchio, G.; Iannazzo, D. Titanium Surface Modification for Implantable Medical Devices with Anti-Bacterial Adhesion Properties. *Materials* **2022**, *15*, 3283. [[CrossRef](#)]
8. Zhang, S.; Yu, Y.; Wang, H.; Ren, L.; Yang, K. Study on mechanical behavior of Cu-bearing antibacterial titanium alloy implant. *J. Mech. Behav. Biomed. Mater.* **2022**, *125*, 104926. [[CrossRef](#)]
9. Yuan, X.; Luo, R.; Ren, J.; Zhang, L.; Jiang, Y.; He, Z. Design of a new Ti-Mo-Cu alloy with excellent mechanical and antibacterial properties as implant materials. *Mater. Lett.* **2022**, *306*, 130875. [[CrossRef](#)]
10. Spataru, M.C.; Cojocaru, F.D.; Sandu, A.V.; Solcan, C.; Duceac, I.A.; Baltatu, M.S.; Voiculescu, I.; Geanta, V.; Vizureanu, P. Assessment of the effects of Si addition to a new TiMoZrTa system. *Materials* **2021**, *14*, 7610. [[CrossRef](#)]
11. Baltatu, M.S.; Vizureanu, P.; Sandu, A.V.; Florido-Suarez, N.; Saceleanu, M.V.; Mirza-Rosca, J.C. New titanium alloys, promising materials for medical devices. *Materials* **2021**, *14*, 5934. [[CrossRef](#)] [[PubMed](#)]

12. Savin, A.; Vizureanu, P.; Prevorovsky, Z.; Chlada, M.; Krofta, J.; Baltatu, M.S.; Istrate, B.; Steigmann, R. Noninvasive Evaluation of Special Alloys for Prostheses Using Complementary Methods. *IOP Conf. Ser.-Mater. Sci. Eng.* **2018**, *374*, 012030. [[CrossRef](#)]
13. Kaczmarek, K.; Konieczny, B.; Siarkiewicz, P.; Leniart, A.; Lukomska-Szymanska, M.; Skrzypek, S.; Lapinska, B. Surface Characterization of Current Dental Ceramics Using Scanning Electron Microscopic and Atomic Force Microscopic Techniques. *Coatings* **2022**, *12*, 1122. [[CrossRef](#)]
14. Li, R.W.K.; Chow, T.W.; Matinlinna, J.P. Ceramic dental biomaterials and CAD/CAM technology: State of the art. *J. Prosthodont. Res.* **2014**, *58*, 208–216. [[CrossRef](#)] [[PubMed](#)]
15. Fu, L.; Engqvist, H.; Xia, W. Glass-ceramics in dentistry: A review. *Materials* **2020**, *13*, 1049. [[CrossRef](#)] [[PubMed](#)]
16. Weng, W.; Biesiekierski, A.; Li, Y.; Wen, C. Effects of selected metallic and interstitial elements on the microstructure and mechanical properties of beta titanium alloys for orthopedic applications. *Materialia* **2019**, *6*, 100323. [[CrossRef](#)]
17. Denry, I.; Holloway, J. Ceramics for dental applications: A review. *Materials* **2010**, *3*, 351–368. [[CrossRef](#)]
18. Zarone, F.; Ruggiero, G.; Leone, R.; Breschi, L.; Leuci, S.; Sorrentino, R. Zirconia-reinforced lithium silicate (ZLS) mechanical and biological properties: A literature review. *J. Dent.* **2021**, *109*, 103661. [[CrossRef](#)]
19. Zhang, L.C.; Chen, L.Y. A review on biomedical titanium alloys: Recent progress and prospect. *Adv. Eng. Mater.* **2019**, *21*, 1801215. [[CrossRef](#)]
20. Vaicelyte, A.; Janssen, C.; Le Borgne, M.; Grosogeat, B. Cobalt–Chromium Dental Alloys: Metal Exposures, Toxicological Risks, CMR Classification, and EU Regulatory Framework. *Crystals* **2020**, *10*, 1151. [[CrossRef](#)]
21. Czepułkowska-Pawlak, W.; Wołowiec-Korecka, E.; Klimek, L. The Surface Condition of Ni-Cr after SiC Abrasive Blasting for Applications in Ceramic Restorations. *Materials* **2020**, *13*, 5824. [[CrossRef](#)] [[PubMed](#)]
22. Banaszek, K.; Maślanka, M.; Semenov, M.; Klimek, L. Corrosive Studies of a Prosthetic Ni-Cr Alloy Coated with Ti(C,N) Type Layers. *Materials* **2022**, *15*, 2471. [[CrossRef](#)] [[PubMed](#)]
23. Zheng, C.; Liu, Z.; Chen, S.; Liu, C. Corrosion Behavior of a Ni–Cr–Mo Alloy Coating Fabricated by Laser Cladding in a Simulated Sulfuric Acid Dew Point Corrosion Environment. *Coatings* **2020**, *10*, 849. [[CrossRef](#)]
24. Wołowiec-Korecka, E.; Czepułkowska-Pawlak, W.; Kula, Z.; Klimek, L. Effect of SiC Abrasive Blasting Parameters on the Quality of the Ceramic and Ni-Cr Dental Alloy Joint. *Materials* **2022**, *15*, 964. [[CrossRef](#)] [[PubMed](#)]
25. Pătrașcu, I. *Materiale Dentare*; Horanda Press: București, Romania, 2002.
26. Vaillant-Corroy, A.S.; Corne, P.; De March, P.; Fleutot, S.; Cleymand, F. Influence of recasting on the quality of dental alloys: A systematic review. *J. Prosthet. Dent.* **2015**, *114*, 205–211. [[CrossRef](#)]
27. Sartori, I.A.M.; Ramos, C.M.; Faot, F.; Silva, L.M.; Valgas, L.; Borges, A.F.S. Mechanical behavior of NiCr and NiCrTi alloys for implant prosthetic components. *Braz. Dent. Sci.* **2013**, *16*, 37–43. [[CrossRef](#)]
28. Lee, J.H.; Choi, S.K.; Hong, M.H. The metallurgical characteristics of non-precious alloys using Nd:YAG laser welding. *Biomater. Res.* **2015**, *19*, 25. [[CrossRef](#)]
29. Chen, C.F.; Hu, J.C.; Bresciani, E.; Peters, M.C.; Estrella, M.R. Treatment considerations for patient with Amelogenesis Imperfecta: A review. *Braz. Dent. Sci.* **2013**, *16*, 7–18. [[CrossRef](#)] [[PubMed](#)]
30. Yoo, J.H.; Lee, M.G.; Kim, Y.L. The Bond Strength of Ni-Cr Free Alloys of Recasting for Porcelain Fused to Metal. *Int. J. Clin. Prev. Dent.* **2012**, *8*, 1–16.
31. López Ríos, M.; Socorro Perdomo, P.P.; Voiculescu, I.; Geanta, V.; Craciun, V.; Boerasu, I.; Mirza-Rosca, J.C. Effects of nickel content on the microstructure, microhardness and corrosion behavior of high-entropy AlCoCrFeNi alloys. *Sci. Rep.* **2020**, *10*, 21119. [[CrossRef](#)]
32. Gil, F.J.; Manzanares, N.; Badet Gil, F.; Aparicio, C.; Ginebra, M.P. Biomimetic treatment on dental implants for short-term bone regeneration. *Clin. Oral Invest.* **2014**, *18*, 59–66. [[CrossRef](#)]
33. Madani, A.S.; Rokni, S.R.; Mohammadi, A.; Bahrami, M. The Effect of Recasting on Bond Strength between Porcelain and Base-Metal Alloys. *J. Prosthodont.-Implant. Esthet. Reconstr. Dent.* **2011**, *20*, 190–194. [[CrossRef](#)]
34. Bauer, J.; Costa, J.F.; Carvalho, C.N.; Souza, D.N.; Loguercio, A.D.; Grande, R.H. Influence of alloy microstructure on the microshear bond strength of basic alloys to a resin luting cement. *Braz. Dent. J.* **2012**, *23*, 490–495. [[CrossRef](#)] [[PubMed](#)]
35. Quinn, J.; McFadden, R.; Chan, C.W.; Carson, L. Titanium for orthopedic applications: An overview of surface modification to improve biocompatibility and prevent bacterial biofilm formation. *iScience* **2020**, *23*, 101745. [[CrossRef](#)] [[PubMed](#)]
36. Jiang, Z.; Dai, X.; Middleton, H. Effect of silicon on corrosion resistance of Ti–Si alloys. *Mater. Sci. Eng. B* **2011**, *176*, 79–86. [[CrossRef](#)]
37. Choi, A.P.; Zheng, Y.P. Estimation of Young’s modulus and Poisson’s ratio of soft tissue from indentation using two different-sized indentors: Finite element analysis of the finite deformation effect. *Med. Biol. Eng. Comput.* **2005**, *43*, 258–264. [[CrossRef](#)]
38. Brizuela, A.; Herrero-Climent, M.; Rios-Carrasco, E.; Rios-Santos, J.V.; Pérez, R.A.; Manero, J.M.; Gil Mur, J. Influence of the Elastic Modulus on the Osseointegration of Dental Implants. *Materials* **2019**, *12*, 980. [[CrossRef](#)]
39. Grosogeat, B.; Vaicelyte, A.; Gauthier, R.; Janssen, C.; Le Borgne, M. Toxicological Risks of the Cobalt–Chromium Alloys in Dentistry: A Systematic Review. *Materials* **2022**, *15*, 5801. [[CrossRef](#)]
40. Dumitru, C.; Milici, L.D.; Pentiu, R.D.; Atănăsoae, P.; Ungureanu, C.; Hopulele, E. Experimental Analysis on the Impact of Current on the Strength and Lifespan of a Ni-Ti Element. *Appl. Sci.* **2022**, *12*, 3185. [[CrossRef](#)]

Article

Effects of Acidic Challenge on Demineralized Root Surface Treated with Silver Diamine Fluoride and Potassium Iodide

Alexandru Iovan ^{1,†}, Marcelin Benchea ^{2,*} , Simona Stoleriu ^{1,*}, Ionuț Tărăboanță ^{1,†} , Nicanor Cimpoșu ^{3,†}, Irina Nica ^{1,†} and Sorin Andrian ¹

¹ Faculty of Dental Medicine, “Grigore T. Popa” University of Medicine and Pharmacy, 16 Universitatii Str., 700115 Iași, Romania

² Faculty of Mechanical Engineering, “Gh. Asachi” Technical University, 67 Dimitrie Mangeron Str., 700050 Iași, Romania

³ Faculty of Materials Science and Engineering, “Gh. Asachi” Technical University, 67 Dimitrie Mangeron Str., 700050 Iași, Romania

* Correspondence: marcelin.benchea@tuiasi.ro (M.B.); simona.stoleriu@umfiasi.ro (S.S.)

† These authors contributed equally to this work.

Abstract: Background: The aim of the study was to assess the protective effect of applying potassium iodide (KI) over silver diamine fluoride (SDF) on demineralized root dentin in the case of a sustained acidogenic attack. Methods: Forty caries-free third molars were used in the study. A diamond disc was used to separate the roots and the tooth crowns from the roots. Each root fragment was randomly distributed in one of the four study groups: C—samples were not demineralized; DD—demineralized samples; RS1—demineralized samples covered with SDF+KI (RS-Riva Star product, SDI limited, Bayswater, Australia); RS2—demineralized samples covered with SDF+KI and submersed to another acidic challenge for 3 days. SEM and EDX were used for the morphological and elemental analysis. Vickers hardness assessment was performed using a tribometer CETR UMT-2 (Bruker Corporation, Berlin, Germany). One-way ANOVA and post hoc Bonferroni tests were used for the statistical analysis with a significance level of $p < 0.05$. Results: Morphological and elemental changes were observed on the surface of the study samples. Significant differences were observed between the recorded hardness values of groups C and DD ($p = 0.005$), C and RS2 ($p = 0.002$), DD and RS1 ($p = 0.011$); RS1 and RS2 ($p = 0.004$). Conclusions: The application of SDF and KI (Riva Star product) on root dentin caries resulted in the formation of a heterogeneous outer layer that sealed the dentin and increased the microhardness of the treated surface. In the conditions of the present study, this layer did not provide enough protection for root dentin exposed to continuous attacks.

Keywords: silver diamine fluoride SDF; hardness; root caries; remineralization; SEM; EDX



Citation: Iovan, A.; Benchea, M.; Stoleriu, S.; Tărăboanță, I.; Cimpoșu, N.; Nica, I.; Andrian, S. Effects of Acidic Challenge on Demineralized Root Surface Treated with Silver Diamine Fluoride and Potassium Iodide. *Diagnostics* **2023**, *13*, 530. <https://doi.org/10.3390/diagnostics13030530>

Academic Editor: Daniel Fried

Received: 17 December 2022

Revised: 26 January 2023

Accepted: 29 January 2023

Published: 1 February 2023



Copyright: © 2023 by the authors. Licensee MDPI, Basel, Switzerland. This article is an open access article distributed under the terms and conditions of the Creative Commons Attribution (CC BY) license (<https://creativecommons.org/licenses/by/4.0/>).

1. Introduction

Root caries is a pathology inevitably associated with periodontal disease [1]. With the increase in life expectancy and the advances in dentistry, the number of teeth with periodontal recessions and susceptibility to root caries has significantly increased [2,3]. The treatment of carious root surfaces can be more difficult compared to coronal surfaces due to the complexity of the local context (cementum/root dentin/marginal periodontium), as well as the debilitating pathology associated with patients' age.

For this reason, the therapeutic management of root caries is oriented towards minimally invasive strategies and the promotion of arresting root lesions by controlling etiological factors [4]. Non-restorative caries control is a recently proposed treatment alternative for root caries [5]. This strategy aims at exposing the lesion to cleaning and self-cleaning agents and applying varnishes that reduce carious activity and promote remineralization [6]. The efficiency of the method in controlling the dental caries of primary teeth has been evaluated by several studies [7,8], but the scientific evidence for the root caries treatment is relatively

scarce. Treatment recommendations in active root lesions suggest the application of highly concentrated fluoride varnishes (>20,000 ppm) and silver diamino fluoride (SDF > 30%), although these recommendations are based on inconclusive evidence [4].

The presence of active root caries is associated with the existence of a highly cariogenic oral environment. Elderly patients and those with debilitating systemic diseases, who represent the main risk group, show a reduced capacity for radical changes in dietary and oral hygiene habits [9]. The success of non-restorative therapy involves changing the oral environment conditions in favor of remineralization phenomena. In the absence of this change, it seems unlikely that non-operative treatment will be sufficient to stop the lesions. The application of SDF is one of the proposed alternatives for preventing and arresting root caries [9,10]. Combining SDF with potassium iodide (KI) was proposed to prevent SDF-induced post-therapeutic staining [11,12], but the long-term effectiveness of this combination has not been validated by sufficient clinical and laboratory studies. This study aimed to analyze whether such a material protects the demineralized root dentin in the case of a sustained acidogenic attack, characterized by prolonged periods in which the pH drops below the critical value.

Therefore, the effects of treatment with SDF and KI root dentin hardness, chemical composition, and morphology of the demineralized root surface were evaluated immediately after the application of the material and after exposure to a prolonged cariogenic attack. The null hypothesis was that SDF+KI application and the subsequent exposure to cariogenic attack do not influence the physical and chemical properties of root dentin.

2. Materials and Methods

2.1. Sample Preparation

G*Power software (version 3.1.9.7., Heinrich Heine-Universität Düsseldorf, Düsseldorf, Germany) was used for the sample size calculation. An effect size of 0.25 was used, which is a medium effect according to Cohen's classification. The alpha value was 0.05 with a power of 95%. The results estimated a total number of 79 required samples.

For the present study, forty caries-free third molars were used, extracted in accordance with a protocol (no. 89/07 June 2021) approved by the Research Ethics Committee of "Gr. T. Popa", University of Medicine and Pharmacy of Iasi, Romania. Collected teeth were cleaned by manual scaling and brushing with polishing paste Universal Polishing Paste (Ivoclar Vivadent, Schaan, Lichtenstein) and then stored in a 0.5% chloramine T solution at 4 °C until testing. A diamond disc (DFS-DIAMON GmbH, Riedenburg, Germany) activated at 5000 rpm under running water was used to separate the roots and the tooth crowns from the roots (Figure 1B). Each root fragment was distributed to one of the 4 study groups described in Table 1.

Table 1. Distribution of the samples in groups.

Study Group	Study Protocol
C (<i>n</i> = 20)	Control group: Samples were submersed in distilled water
DD (<i>n</i> = 20)	Samples were submersed in demineralizing solution for 3 days
RS 1 (<i>n</i> = 20)	Samples were submersed in demineralizing solution for 3 days Riva Star product (RS) (SDI limited, Bayswater, Australia) was then applied on the exposed dentin surface
RS 2 (<i>n</i> = 20)	Samples were submersed in demineralizing solution for 3 days Riva Star product (RS) (SDI limited, Bayswater, Australia) was then applied on the exposed dentin surface Samples were stored in distilled water for 24 h Samples were submersed in demineralizing solution for 3 days

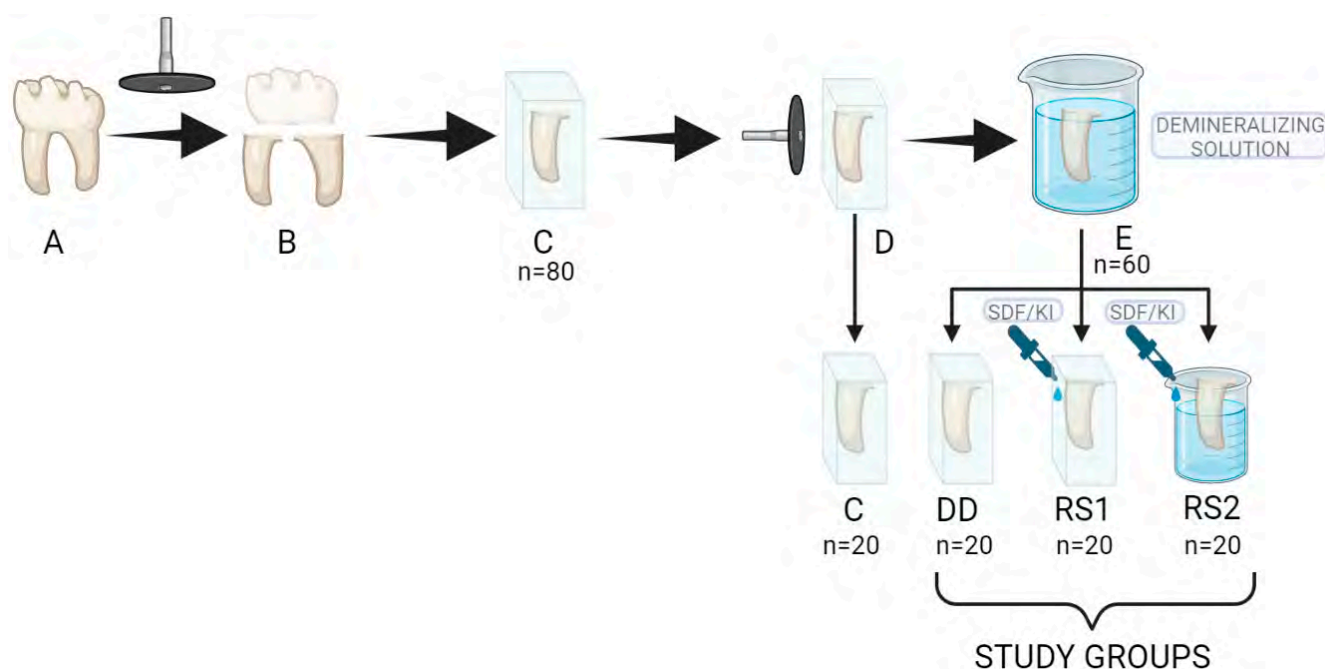


Figure 1. Sample preparation steps. (A) caries-free third molar; (B) separation of crown and roots with a diamond disc; (C) root fragments embedded in blocks of self-curing acrylic resin; (D) root surfaces planed and polished with extra-thin abrasive discs; (E) samples in groups (DD,RS1,RS2) stored in a 10 mL demineralizing solution.

The root fragments were then embedded in blocks of self-curing acrylic resin (Duracryl Plus, Spofa Dental, Jičín, Czech Republic) so that only one root surface was exposed (Figure 1C). The surfaces were then planed and polished with Sof-Lex™ Extra-thin abrasive discs (3M ESPE Dental Products, St. Paul, MN, USA) with decreasing grit (Figure 1D). The samples were cleaned of detritus in an ultrasonic bath for 5 min. A layer of acid-resistant nail varnish was applied to the prepared surfaces in order to obtain a 4 mm × 3 mm area of exposed root dentin.

Samples in groups DD, RS1, and RS2 were stored in a 10 mL demineralizing solution (Figure 1E) containing 0.2 M lactic acid, 3.0 mM CaCl₂, and 1.8 mM KH₂PO₄ with a pH of 4.5 for 3 days at 37 °C to simulate artificial root caries lesions [13,14]. The solution was changed each 24 h in order to keep a constant pH. The pH was verified every 12 h with a pH meter (Thermo Scientific Eutech pH 5+, Vernon Hills, IL, USA).

After the demineralization process, the samples were rinsed thoroughly with distilled water and gently air-dried without desiccating the dentin. Then, each sample in groups DD, RS1, and RS2 was subjected to one of the 3 experimental protocols on the exposed root surface (Table 1), after which they were stored for 24 h in distilled water until evaluation by scanning electron microscopy (SEM) and spectroscopy (EDX) or hardness evaluation.

The composition and the application protocol of the Riva Star product are presented in Tables 2 and 3.

Table 2. Composition of the Riva Star product.

Product	Composition	Batch No.
Riva Star Capsule Kit (SDI Limited Australia)	Riva Star Step 1: 38% silver diaminofluoride (SDF) Riva Star Step 2: potassium iodide (KI)	1164696

Table 3. Application protocol of Riva Star product.

Protocol
Riva Star Solution Step 1 was applied on the exposed dentin surface Riva Star Solution Step 2 was immediately applied to the treated surface until the creamy-white precipitate became clear.

2.2. SEM Evaluation

Three samples in each group were morphologically evaluated under a Scanning Electron Microscope (Vega Tescan LMH II, Tescan, Brno, Czech Republic) with operating conditions of 10–30 kV, 15.5 WD. Secondary electrons (SE) detector was used to obtain the images. There were no phase differences in the material, and the variation in the cathode power permitted the correct biological material evaluation.

2.3. EDX Evaluation

Elemental analysis was realized on three samples in each study group by X-ray dispersive spectroscopy using an EDX X Flash 6L10 detector, Esprit 2.2 (Esprit, Bruker Corporation, Berlin, Germany) soft wave in automatic mode/list of elements, and Line, Point and Mapping sought to detect the presence and distribution of calcium, phosphorus, silver, potassium, iodine, and fluorine. Energy-dispersive spectroscopy experiments (Automatic-Precise mode, PB-ZAF detection type with 0.01% detection limit) were realized with repetition on different areas in order to obtain average values (five times). Esprit 2.2 software was used to evaluate the energies registered. Standard deviation of the elements' percentages was established (from five determinations of chemical composition percentages on the same area 0.25 mm²) for each chemical element. Absolute and relative errors of the detector were presented in order to compare the results.

2.4. Microhardness Test

The surface microhardness of 10 samples in each group was assessed using a tribometer CETR UMT-2 (Bruker Corporation, Berlin, Germany). A Vickers-type indenter was used for the microindentation test (diamond cone with an angle of 120° and a tip with a radius of 200 µm). The samples were fixed on the flat plate of the tribometer, and the indentations were made by pressing the indenter with a vertical force of 5 N with an indentation speed of 0.005 mm/s, a preload time of 15 s, a charging time of 30 s, a holding time of 15 s, and a download time of 30 s. The software (Tribometer CETR UMT-2, Version 1.01 software, Bruker Corporation, Berlin, Germany) performed the automatic test and recorded the vertical load F_z , the time, and the vertical displacement distance C of the indenter (depth of penetration). Hardness was automatically calculated from the discharge slope curve and expressed in GPa.

2.5. Statistical Analysis

IBM SPSS 26.0.0. software (SPSS Inc., Chicago, IL, USA) was used for statistical analysis. Levene's test was used to assess the homogeneity of variances, and then statistical analysis was performed using one-way analysis of variance (ANOVA) and post hoc Bonferroni tests with a significance level of $p < 0.05$.

3. Results

3.1. SEM Evaluation Results

The morphological analysis of dentin subjected to demineralization (group DD) showed the dentin surface with opened tubules and the absence of a smear layer (Figure 2c,d).

The morphological analysis of the samples in group RS1, consisting of demineralized dentin samples treated with RS, revealed deposits with a heterogeneous appearance on the dentin surface. Most images show areas of dentin completely covered with uniform deposits with a granular appearance (Figure 2e,f). On all samples, including areas where

inconsistent deposits were observed, the dentinal tubules appeared completely occluded with a precipitate or crystalline-looking particles.

For the samples in group RS2, the images showed less consistent material deposition. The deposits on the surface were uneven. The particles had variable sizes and were more dispersed compared to the images of the samples treated with RS immediately after application (Figure 2g,h).

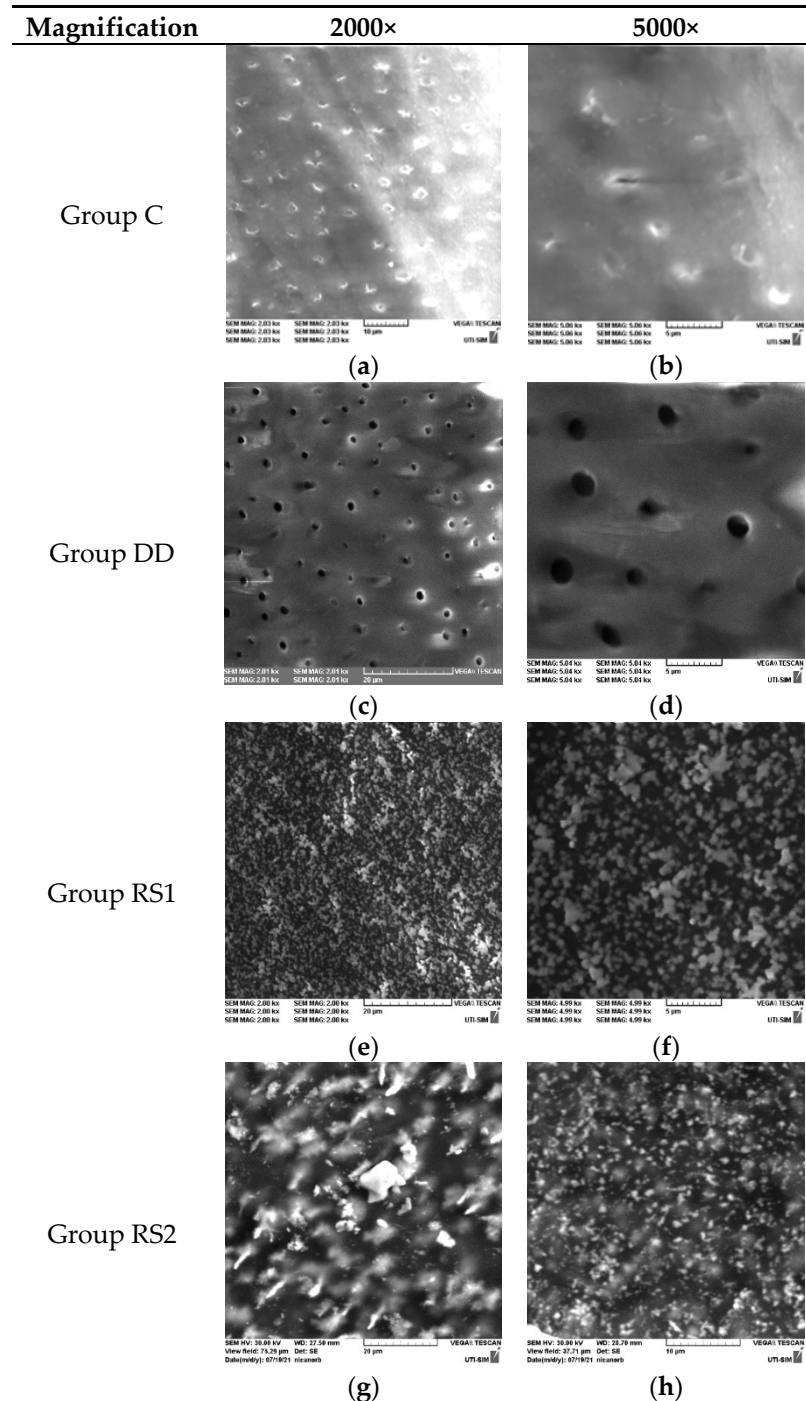


Figure 2. SEM images of a sample in each group (C, DD, RS1, RS2) at 2000× and 5000× magnifications.

3.2. EDX Evaluation Results

For the samples in group C, EDX analysis showed the presence of calcium and phosphorus on the samples' surface. The analysis confirmed high mass concentration and normalized weight percent of oxygen, followed by carbon and calcium, and lower concentrations of phosphorous. An example of EDX elemental analysis on the surface of one sample in group C is presented in Table 4.

Table 4. EDX elemental analysis on the surface of a study sample in group C.

Element	Mass Norm. (%)	Atom (%)	abs. Error (%) (1 Sigma)
Oxygen	46.12745	53.05732	7.906657
Calcium	24.93783	11.45097	0.931029
Carbon	19.5091	29.89149	4.159093
Phosphorus	9.425618	5.600225	0.495739
Sum	100	100	

EDX analysis of the samples in group DD also showed high mass concentration and normalized weight percentage of carbon and oxygen, followed by nitrogen. Calcium and phosphorus were detected in lower concentrations than in group C. An example of EDX elemental analysis on the surface of one sample in group DD is presented in Table 5.

Table 5. EDX elemental analysis on the surface of a study sample in group DD.

Element	Mass Norm. (%)	Atom (%)	abs. Error (%) (1 Sigma)
Carbon	46.2307	54.4655	6.85517
Oxygen	34.19054	30.23935	5.822515
Nitrogen	12.40779	12.53513	3.712765
Calcium	4.972625	1.755698	0.185945
Phosphorus	2.198341	1.004318	0.123339
Sum	100	100	

For the samples in group RS 1, EDX analysis showed the presence of high concentrations of iodine, followed by silver, and lower concentrations of potassium on the samples' surfaces. In contrast, fluorine was almost undetectable (mass concentration and normalized weight percent were lower than the values of absolute and relative errors of detection), and calcium and phosphorus were undetectable. An example of EDX elemental analysis on the surface of one sample in group RS1 is presented in Table 6.

Table 6. EDX elemental analysis on the surface of a study sample in group RS1.

Element	Mass Norm. (%)	Atom (%)	abs. Error (%) (1 Sigma)
Iodine	46.34	20.72	3.90
Silver	35.93	18.90	2.30
Oxygen	16.38	58.10	3.70
Potassium	1.13	1.64	0.57
Fluorine	0.22	0.64	0.73
Sum	100	100	

For the samples in group RS2, EDX analysis confirmed the presence of iodine and silver on the surfaces of samples with higher concentrations of iodine, followed by silver, while potassium and fluorine were undetectable. Calcium and phosphorus were observed in amounts close to the detection limit. An example of EDX elemental analysis on the surface of one sample in group RS2 is presented in Table 7.

Table 7. EDX elemental analysis on the surface of a study sample in group RS2.

Element	Mass Norm. (%)	Atom (%)	abs. Error (%) (1 Sigma)
Oxygen	59.03	90.55	3.012
Iodine	23.05	4.46	0.31
Silver	15.67	3.56	0.23
Calcium	1.96	1.20	0.10
Phosphorus	0.29	0.23	0.08
Sum	100	100	

3.3. Microhardness Test Results

Hardness mean values and standard deviations for all the groups are presented in Figure 3. It can be observed that control group C reached the peak with a value of 0.50 GPa, followed by groups RS1 with 0.48 GPa, DD with 0.28 GPa, and RS2 with 0.25 GPa. Statistically significant differences were recorded between groups C and DD ($p = 0.005$); C and RS2 ($p = 0.002$); DD and RS1 ($p = 0.011$); RS1 and RS2 ($p = 0.004$).

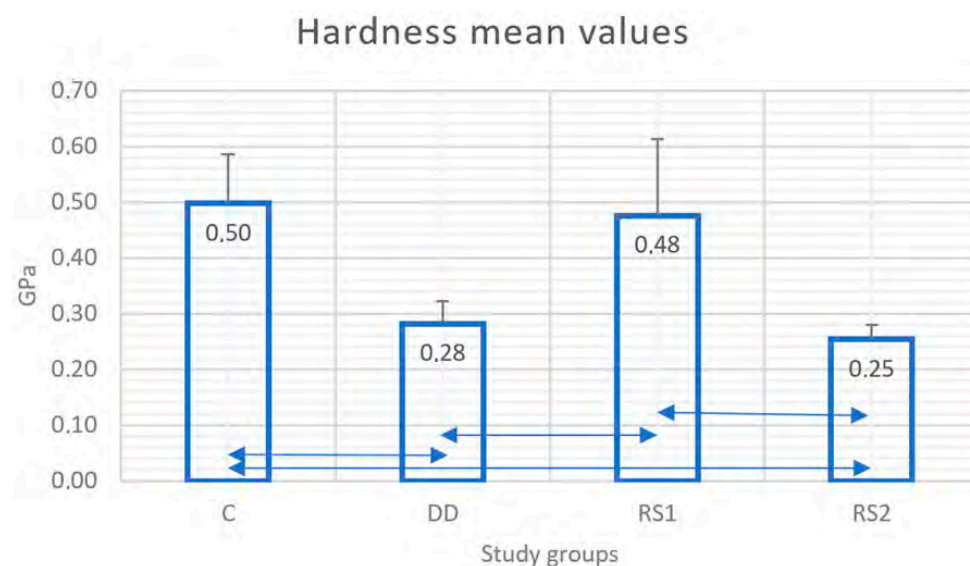


Figure 3. Mean values (Gpa) and standard deviations (SD) of hardness in each study group. Double arrow lines (\longleftrightarrow) show statistical differences between groups.

4. Discussion

Ample evidence supports the efficacy of high-concentration fluoride in the management of root caries [15]. In the presence of an organic dental matrix, the mechanism of remineralization is based on the absorption of remineralizing ions into the underlying demineralized tissue rather than precipitation on the surface [16]. When subjected to immediate acid or mechanical attack, these materials can significantly diminish their effectiveness. Therefore, this study aims to evaluate tooth behavior in a demineralizing environment that simulates an intense and prolonged cariogenic attack immediately after the application of the remineralizing material. To simulate artificial root caries lesion and acidic attack after remineralization, we used a demineralization solution that had been also applied in other previous studies [12,17].

SDF promotes remineralization and increases the resistance of dental tissues to acid attack by forming calcium fluoride and hydroxyapatite deposits [18], inhibits microbial activity mainly due to silver ions [19], and prevents the degradation of dentinal collagen by inhibiting the activity of collagenases and cysteine-cathepsins [20]. The material tested in this study uses a combination of SDF with KI. Potassium iodide was introduced more

recently to prevent the staining of dentin caused by unreacted silver ions after exposure to light.

In our study, SEM images and EDX analyses revealed the presence of a heterogeneous layer with high concentrations of silver and iodine that covered demineralized dentin treated with RS immediately after application. The dentinal tubules were consistently occluded by granular deposits, regardless of the area examined. This aspect is consistent with the results of a previous study that showed the formation of dense, granular, clustered structures after SDF treatment [21]. The EDX analysis did not provide sufficient data to determine the chemical composition of the layer, but it showed the presence of iodine, silver and potassium on the surface in proportions that varied depending on the morphology of the examined areas.

The surface morphology was modified after acid attack, with increased dispersion of the deposits on the dentin surface. Elemental EDX analysis confirmed the decrease in silver and iodine concentrations on the surface of RS-treated samples after the acid attack. Previous EDX studies suggest that the metal crystals precipitated on the surface of the specimen may be AgCl salts [15] with irregular shapes [22], but in our study, the areas with granular agglomerations showed high concentrations of silver and iodine while chlorine proportions were below the detection limit. The explanation is probably related to the storage medium that had been used. In our study, EDX analysis revealed only high concentrations of silver and iodine in the crystalline particles, probably as a result of the RS mechanism combining SDF and KI during application, leading to AgI formation and reducing the silver ions available for reaction with dentin [23,24]. The low phosphorus concentrations found in this study suggest that if silver phosphate was formed during the reaction with hydroxyapatite, it was probably present in deeper subsurface areas. Another explanation could be related to the sensitivity of the detection method and especially to the time required for the silver phosphate crystals to become mature [25].

An unexpected result was the low amount of fluoride detected after RS application. Traces of fluoride were almost undetectable in the outer layers of both experimental groups. Normally, a 38% SDF solution contains 44,800 ppm of fluoride [26]; therefore, calcium fluoride-like compounds are expected to be formed after application [27]. However, a previous *in vitro* study also found that silver and fluoride were inconspicuous in active carious lesions treated with SDF [28], and other laboratory studies showed decreased fluoride content after water washing [29] or could not find calcium fluoride on demineralized dentin treated with SDF after pH-cycling [22,30].

The lack of fluorine detection can be explained by a rapid washing effect caused by the high fluidity of SDF solutions [29,31] or by the high detection limit of EDX [32]. Moreover, the caries model with a continuous acid challenge without de-/remineralization cycles and the short storage period could contribute to the accelerated dissolution of calcium fluoride without the formation of fluorapatite crystals.

To validate the SEM and EDX analysis results, mechanical tests were performed. Rehabilitation of mechanical properties is considered a good indicator of functional remineralization of damaged dentin [33–35].

In our study, the application of RS produced a significant increase in the hardness values of demineralized dentin immediately after application. However, the treatment was not able to increase the microhardness to values similar to those of sound dentin, a conclusion that has been confirmed by a previous study performed on demineralized bovine dentin [36]. Other previous studies confirmed the improvement in the mechanical properties of the demineralized dentin after SDF+KI treatment [15,37]. Knoop hardness, modulus of elasticity, and creep behavior improved after the application of SDF+KI on the dentin demineralized by storage for five days in a similar solution [15]. Other studies also concluded that SDF improved the properties of artificial demineralized dentin even when compared to other fluoride varnishes [37,38].

In the present study, the remineralization effect was not fully maintained after subjecting the samples to a demineralization challenge. The surface microhardness significantly

decreased after the storage of the samples treated with RS in acid. In other in vitro studies performed on dentin affected by caries, SDF treatment caused a significant increase in the immediate dentin hardness, which the authors correlated with an increased surface mineralization [21,39,40]. Contrary to our results, this effect persisted after repeated acid attacks simulated by pH cycling for 8 days in de- and re-mineralization solutions [21,41]. These conflicting results can be explained by the pH cycling model allowing some remineralization to occur. In contrast, the continuous and sustained demineralizing attack simulated in our study did not allow these reactions to take place, with the protecting layer being corroded continuously by the acidic solution.

The results of the mechanical tests confirmed the images observed in the scanning electron microscope and EDX analysis, which showed a deterioration of material deposited on the demineralized dentin surface after storage in the demineralizing solution. However, the microhardness values did not significantly decrease below the initial values of demineralized dentin (before the treatment with RS), supporting the hypothesis that RS had a moderate protective effect on root dentin by slowing down its deterioration when acidic challenge persists.

The limitations of our study are primarily related to the chemical model used for caries simulation and the detection limits of SEM and EDX analysis. Within these limits, our results support the effectiveness of SDF+KI in protecting demineralized root dentin against cariogenic attack immediately after application and the drastic reduction in this effect if pH conditions are maintained below the critical level after application of the material. Further studies are needed to evaluate the effectiveness of SDF+KI application on root dentin remineralization in caries models using pH cycling and longer observation periods.

Even with the limitations of the chemical caries model that we used, the results support the hypothesis that this protection is limited under continuous cariogenic or erosive environmental conditions. It seems likely that in the absence of oral allostasis, when the control of risk factors is inefficient, only the application of such materials to root carious surfaces would not stop the progression of root carious lesions. Further studies are needed to evaluate the effect of repeated application of these materials on carious root dentin under simulated conditions of a strongly cariogenic or erosive environment.

5. Conclusions

The application of silver diamine fluoride and potassium iodide on root dentin caries resulted in the formation of a heterogeneous outer layer that sealed the dentin and increased the microhardness of the treated surface.

In the conditions of the present study, this protective layer did not provide enough protection for root dentin exposed to continuous attacks.

Author Contributions: Conceptualization, A.I., M.B., S.S. and S.A.; methodology, I.T., N.C. and I.N.; validation, A.I., S.S., M.B. and S.A.; formal analysis, A.I., M.B., S.S. and N.C.; investigation, A.I., I.T. and I.N.; resources, A.I.; writing—original draft preparation, A.I., S.S., I.T. and I.N.; writing—review and editing, M.B., N.C. and S.A.; visualization, M.B. and S.S.; supervision, N.C. and S.A.; project administration, A.I.; funding acquisition, A.I. All authors have read and agreed to the published version of the manuscript.

Funding: This research received no external funding.

Institutional Review Board Statement: The study was conducted in accordance with the Declaration of Helsinki, and approved by the Ethics Committee of “Grigore T. Popa” University of Medicine and Pharmacy of Iași, Romania (no. 89/07 June 2021).

Informed Consent Statement: Not applicable.

Data Availability Statement: Not applicable.

Conflicts of Interest: The authors declare no conflict of interest.

References

1. Potârniche, O.; Solomon, S.; Păsărin, L.; Mârțu, A.; Nițescu, D.C.; Mârțu, S. Statistical study on the prevalence of gingival recession in young adults. *Int. J. Med. Dent.* **2013**, *3*, 219–224.
2. Sufaru, I.G.; Martu, M.A.; Solomon, S.M. Advances in Periodontal Pathogens. *Microorganisms* **2022**, *10*, 1439. [[CrossRef](#)] [[PubMed](#)]
3. Al Qranei, M.S.; Balhaddad, A.A.; Melo, M.A.S. The burden of root caries: Updated perspectives and advances on management strategies. *Gerodontology* **2021**, *38*, 136–153. [[CrossRef](#)] [[PubMed](#)]
4. Paris, S.; Banerjee, A.; Bottenberg, P.; Breschi, L.; Campus, G.; Doméjean, S.; Ekstrand, K.; Giacaman, R.A.; Haak, R.; Hannig, M.; et al. How to intervene in the caries process in older adults: A joint ORCA and EFCD expert Delphi consensus statement. *Caries Res.* **2020**, *54*, 459–465. [[CrossRef](#)]
5. Eden, E.; Frencken, J.; Gao, S.; Horst, J.A.; Innes, N. Managing dental caries against the backdrop of COVID-19: Approaches to reduce aerosol generation. *Br. Dent. J.* **2020**, *229*, 411–416. [[CrossRef](#)] [[PubMed](#)]
6. van Strijp, G.; van Loveren, C. No Removal and Inactivation of Carious Tissue: Non-Restorative Cavity Control. In *Caries Excavation: Evolution of Treating Cavitated Carious Lesions*; Karger Publishers: Basel, Switzerland, 2018; Volume 27, pp. 124–136.
7. Santamaria, R.M.; Innes, N.P.; Machiulskiene, V.; Schmoekel, J.; Alkilzy, M.; Splieth, C.H. Alternative caries management options for primary molars: 2.5-year outcomes of a randomised clinical trial. *Caries Res.* **2017**, *51*, 605–614. [[CrossRef](#)] [[PubMed](#)]
8. Mijan, M.; de Amorim, R.G.; Leal, S.C.; Mulder, J.; Oliveira, L.; Creugers, N.H.; Frencken, J.E. The 3.5-year survival rates of primary molars treated according to three treatment protocols: A controlled clinical trial. *Clin. Oral Investig.* **2014**, *18*, 1061–1069.
9. Grandjean, M.L.; Maccarone-Ruetsche, N.; McKenna, G.; Muller, F.; Srinivasan, M. Silver Diamine Fluoride (SDF) in the management of root caries in elders: A systematic review and meta-analysis. *Swiss Dent. J.* **2021**, *131*, 417–424.
10. Castelo, R.; Attik, N.; Catirse, A.B.; Pradelle-Plasse, N.; Tirapelli, C.; Grosogoeat, B. Is there a preferable management for root caries in middle-aged and older adults? A systematic review. *Br. Dent. J.* **2021**, *27*, 1–7. [[CrossRef](#)]
11. Knight, G.M.; McIntyre, J.M.; Craig, G.G.; Mulyani Zilm, P.S.; Gully, N.J. Inability to form a biofilm of *Streptococcus mutans* on silver fluoride- and potassium iodide-treated demineralized dentin. *Quintessence Int.* **2009**, *40*, 155–161.
12. Srisomboon, S.; Kettratad, M.; Stray, A.; Pakawanit, P.; Rojviriyaya, C.; Patntirapong, S.; Panpisut, P. Effects of silver diamine nitrate and silver diamine fluoride on dentin remineralization and cytotoxicity to dental pulp cells: An in vitro study. *J. Funct. Biomater.* **2022**, *13*, 16. [[CrossRef](#)]
13. Yagi, K.; Yamamoto, H.; Uemura, R.; Matsuda, Y.; Okuyama, K.; Ishimoto, T.; Nakano, T.; Hayashi, M. Use of PIXE/PIGE for sequential Ca and F measurements in root carious model. *Sci. Rep.* **2017**, *7*, 13450. [[CrossRef](#)] [[PubMed](#)]
14. Matsuda, Y.; Komatsu, H.; Murata, Y.; Tanaka, T.; Sano, H. A newly designed automatic pH-cycling system to stimulate daily pH fluctuation. *Dent. Mater. J.* **2006**, *25*, 280–285. [[CrossRef](#)] [[PubMed](#)]
15. Peterson, I.M.; Pajares, A.; Lawn, B.R.; Thompson, V.P.; Rekow, E.D. Mechanical characterization of dental ceramics by Hertzian contacts. *J. Dent. Res.* **1998**, *77*, 589–602. [[CrossRef](#)] [[PubMed](#)]
16. Cai, J.; Burrow, M.F.; Manton, D.J.; Tsuda, Y.; Sobh, E.G.; Palamara, J.E.A. Effects of silver diamine fluoride/potassium iodide on artificial root caries lesions with adjunctive application of proanthocyanidin. *Acta Biomater.* **2019**, *88*, 491–502. [[CrossRef](#)]
17. Ganss, C.; Hardt, M.; Lussi, A.; Cocks, A.K.; Klimek, J.; Schlueter, N. Mechanism of action of tin-containing fluoride solutions as anti-erosive agents in dentine—An in vitro tin-uptake, tissue loss, and scanning electron microscopy study. *Eur. J. Oral Sci.* **2010**, *118*, 376–384. [[CrossRef](#)]
18. Iovan, A.; Stoleriu, S.; Ghiorghe, C.A.; Pancu, G.; Topoliceanu, C.; Moldovanu, A.; Iovan, G.; Andrian, S. Effect of silver diamine fluoride and potassium iodide on artificial root caries subjected to demineralization. *Rom. J. Oral Rehabil.* **2021**, *13*, 82–91.
19. Seifo, N.; Robertson, M.; Maclean, J.; Blain, K.; Grosse, S.; Milne, R.; Seeballuck, C.; Innes, N. The use of silver diamine fluoride (SDF) in dental practice. *Br. Dent. J.* **2020**, *228*, 75–81. [[CrossRef](#)]
20. Mei, M.L.; Nudelman, F.; Marzec, B.; Walker, J.M.; Lo, E.C.M.; Walls, A.W.; Chu, C.H. Formation of fluorohydroxyapatite with silver diamine fluoride. *J. Dent. Res.* **2017**, *96*, 1122–1128. [[CrossRef](#)]
21. Zhao, I.S.; Gao, S.S.; Hiraishi, N.; Burrow, M.F.; Duangthip, D.; Mei, M.L.; Lo, E.C.; Chu, C.H. Mechanisms of silver diamine fluoride on arresting caries: A literature review. *Int. Dent. J.* **2018**, *68*, 67–76. [[CrossRef](#)]
22. Firouzmandi, M.; Vasei, F.; Giti, R.; Sadeghi, H. Effect of silver diamine fluorid and proanthocyanidin on resistance of carious dentin to acid challenge. *PLoS ONE* **2020**, *15*, e0238590. [[CrossRef](#)]
23. Srisomboon, S.; Kettratad, M.; Pakawanit, P.; Rojviriyaya, C.; Phantumvanit, P.; Panpisut, P. Effects of Different Application Times of Silver Diamine Fluoride on Mineral Precipitation in Demineralized Dentin. *Dent. J.* **2021**, *9*, 70. [[CrossRef](#)] [[PubMed](#)]
24. Barrera Ortega, C.C.; Araiza Tellez, M.A.; Garcia Perez, A.L. Assessment of Enamel Surface Microhardness with Different Fluorinated Compounds under pH Cycling Conditions: An in Vitro Study. *J. Clin. Diagn. Res.* **2019**, *13*, ZC05–ZC10.
25. Mohanty, S.; Satyarup, D.; Nagarajappa, R.; Mahapatra, I.; Dalai, R.P.; Sahu, S. Silver Diamine Fluoride: Game Changer in Dental Public Health: A Review. *Indian J. Forensic Med. Toxicol.* **2020**, *14*, 8655–8659.
26. Sayed, M.; Matsui, N.; Hiraishi, N.; Inoue, G.; Nikaido, T.; Burrow, M.F. Evaluation of discoloration of sound/demineralized root dentin with silver diamine fluoride: In-vitro study. *Dent. Mater. J.* **2019**, *38*, 143–149. [[CrossRef](#)] [[PubMed](#)]
27. Mei, M.L.; Chu, C.H.; Lo, E.C.; Samaranayake, L.P. Fluoride and silver concentrations of silver diammine fluoride solutions for dental use. *Int. J. Paediatr. Dent.* **2013**, *23*, 279–285. [[CrossRef](#)]
28. ten Cate, J.M.; Damen, J.J.M.; Buijs, M.J. Inhibition of dentin demineralization by fluoride in vitro. *Caries Res.* **1998**, *32*, 141–147. [[CrossRef](#)]

29. Mei, M.L.; Ito, L.; Cao, Y.; Li, Q.; Chu, C.H.; Lo, E.C. The inhibitory effects of silver diamine fluoride on cysteine cathepsins. *J. Dent.* **2014**, *42*, 329–335. [[CrossRef](#)]
30. Yu, O.Y.; Mei, M.L.; Zhao, I.S.; Li, Q.L.; Lo, E.C.M.; Chu, C.H. Remineralisation of enamel with silver diamine fluoride and sodium fluoride. *Dent. Mater.* **2018**, *34*, 344–352. [[CrossRef](#)]
31. Mei, M.L.; Ito, L.; Cao, Y.; Li, Q.; Lo, E.C.; Chu, C.H. Inhibitory effect of silver diamine fluoride on dentine demineralisation and collagen degradation. *J. Dent.* **2013**, *41*, 809–817. [[CrossRef](#)]
32. Zhao, I.S.; Mei, M.L.; Burrow, M.F.; Lo, E.C.; Chu, C.H. Prevention of secondary caries using silver diamine fluoride treatment and casein phosphopeptide-amorphous calcium phosphate modified glass-ionomer cement. *J. Dent.* **2017**, *57*, 38–44. [[CrossRef](#)]
33. Sayed, M.; Matsui, N.; Nikaido, T.; Oikawa, M.; Burrow, M.F.; Tagami, J. Morphological and elemental analysis of silver penetration into sound/demineralized dentin after SDF application. *Dent. Mater.* **2019**, *35*, 1718–1727. [[CrossRef](#)] [[PubMed](#)]
34. Bertassoni, L.E.; Habelitz, S.; Kinney, J.H.; Marshall, S.J.; Marshall, G.W., Jr. Biomechanical perspective on the remineralization of dentin. *Caries Res.* **2009**, *43*, 70–77. [[CrossRef](#)]
35. Kinney, J.H.; Marshall, S.J.; Marshall, G.W. The mechanical properties of human dentin: A critical review and re-evaluation of the dental literature. *Crit. Rev. Oral Biol. Med.* **2003**, *14*, 13–29. [[CrossRef](#)] [[PubMed](#)]
36. Kanarakis, I.; Sandu, D.; Solomon, S.M.; Pasarin, L.; Sufaru, I.G.; Martu, M.A.; Sioustis, I.A.; Kappenberg-Nitescu, D.C.; Luchian, I. Contemporary aspects regarding the etiology of gingival recessions. A review. *Rom. J. Oral Rehabil.* **2021**, *13*, 78–86.
37. Ferreira, A.C.; de Lima Oliveira, R.F.; Amorim, A.A.; Geng-Vivanco, R.; de Carvalho Panzeri Pires-de-Souza, F. Remineralization of caries-affected dentin and color stability of teeth restored after treatment with silver diamine fluoride and bioactive glass–ceramic. *Clin. Oral Investig.* **2022**, *26*, 4805–4816. [[CrossRef](#)] [[PubMed](#)]
38. Tiba, A.A.; Tiba, A.; Horvath, F.; Huh, E.Y.; Ford, A.A.; Arens, D.K.; Sarwar, T.; Hwang, Y. Effects of a Two-Step Silver Diamine Fluoride Varnish on Shear Bond Strength of Restorations, Dentin and Enamel Hardness, and Biofilm Formation. *Mil. Med.* **2022**, 1–11. [[CrossRef](#)]
39. Wierichs, R.J.; Stausberg, S.; Lausch, J.; Meyer-Lueckel, H.; Esteves-Oliveira, M. Caries-Preventive Effect of NaF, NaF plus TCP, NaFplus CPP-ACP, and SDF Varnishes on Sound Dentin and Artificial Dentin Caries in vitro. *Caries Res.* **2018**, *52*, 199–211. [[CrossRef](#)]
40. Firouzmandi, M.; Shafiei, F.; Jowkar, Z.; Nazemi, F. Effect of Silver Diamine Fluoride and Proanthocyanidin on Mechanical Properties of Caries-Affected Dentin. *Eur. J. Dent.* **2019**, *13*, 255–260. [[CrossRef](#)]
41. Vieira, A.; Ruben, J.L.; Huysmans, M.C. Effect of titanium tetrafluoride, amine fluoride and fluoride varnish on enamel erosion in vitro. *Caries Res.* **2005**, *39*, 371–379. [[CrossRef](#)]

Disclaimer/Publisher’s Note: The statements, opinions and data contained in all publications are solely those of the individual author(s) and contributor(s) and not of MDPI and/or the editor(s). MDPI and/or the editor(s) disclaim responsibility for any injury to people or property resulting from any ideas, methods, instructions or products referred to in the content.